Computational Modeling of Elastic and Transformation Incompatibility at Grain Boundaries in Shape Memory Materials

by
Zhiyi Wang
B.S.E., Shanghai Jiaotong University (2015)
S.M., Massachusetts Institute of Technology (2018)
Submitted to the Department of Aeronautics and Astronautics
in partial fulfillment of the requirements for the degree of
Doctor of Philosophy
at the
MASSACHUSETTS INSTITUTE OF TECHNOLOGY
September 2022

Author .....
Department of Aeronautics and Astronautics
June 2, 2022

Certified by .....
Raúl Radovitzky
Professor of Aeronautics and Astronautics
Thesis Supervisor

Committee Member .....
Rohan Abeyaratne
Professor of Mechanical Engineering

Committee Member .....
Christopher Schuh
Professor of Materials Science and Engineering

Committee Member .....
Xuanhe Zhao
Professor of Mechanical Engineering

Accepted by .....
Jonathan P. How
R. C. Maclaurin Professor of Aeronautics and Astronautics
Chair, Graduate Program Committee

Computational Modeling of Elastic and Transformation Incompatibility at Grain Boundaries in Shape Memory Materials

by

Zhiyi Wang

Submitted to the Department of Aeronautics and Astronautics
on June 2, 2022, in partial fulfillment of the
requirements for the degree of
Doctor of Philosophy

Abstract

Shape memory alloys (SMAs) and zirconia-based ceramics (SMCs) find a wide range of applications in various fields due to their unique properties such as superelasticity and shape memory effect. Desirable superelastic properties of shape memory materials are realized to their maximum extent in single crystalline structures due to the absence of internal constraints. By contrast, in polycrystalline forms, superelasticity is significantly compromised by severe premature intergranular fracture originated at grain boundaries. This limitation has generated significant research interest focused on developing microstructures that can preserve the properties of single crystals while avoiding the production cost and manufacturing limitations of single-crystal processing.

The overarching goal of the thesis is to improve our understanding of the competition between martensitic transformation, grain boundary constraints, and intergranular fracture in shape memory materials through comprehensive computational modeling. To this end, we developed a finite-element based framework for modeling martensitic transformation at the continuum level incorporating details of the micromechanical information. A single-crystal model is implemented to provide a full mechanistic three-dimensional description of both the anisotropic elastic and martensitic transformation stress-strain response, including the non-Schmid behavior observed in some types of SMCs. We used the geometrically nonlinear theory of martensite to identify all possible transformation systems in SMAs and SMCs, based on the knowledge of lattice parameters of the single crystal. In the case of SMCs, the model was calibrated against data obtained from compression tests of zirconia micropillars in previously published literature. We conducted finite element simulations to obtain detailed information on the nucleation and evolution of martensite variants and stress distribution at grain boundaries in both SMAs and SMCs. The simulation results also provide insights on the competing mechanisms of elastic and transformation incompatibility leading to severe stress concentration at grain bound-

aries. We identified grain boundary configurations which result in very large stress concentrations at very low deformations due to elastic incompatibility, as well as others where the elastic incompatibility is relatively low and stress concentrations only occur at large transformation strains. We also showed how this approach can be used to explore the misorientation space for quantifying the level of elastic and transformation incompatibility at grain boundaries in both SMAs and SMCs. In addition we investigated the correlation between different types of incompatibilities and grain boundary characteristics. In the particular case of SMAs, we explored the role that a coincident site lattice (CSL) may have in affecting grain boundary incompatibilities. We demonstrated that grain boundaries with low CSL order exhibit low elastic incompatibilities in Cu-based SMAs, as previously suggested from experimental observations. However, high CSL order grain boundaries result in incompatibilities that are commensurate with those exhibited by random grain boundary configurations. This approach could be used to identify misorientations that reduce or minimize grain boundary incompatibilities, thus extend the superelastic range of the material.

Thesis Supervisor: Raúl Radovitzky
Title: Professor of Aeronautics and Astronautics

Committee Member: Rohan Abeyaratne
Title: Professor of Mechanical Engineering

Committee Member: Christopher Schuh
Title: Professor of Materials Science and Engineering

Committee Member: Xuanhe Zhao
Title: Professor of Mechanical Engineering

Acknowledgments

First off I would like to express my deepest gratitude to my advisor Raúl Radovitzky. Raúl, I cannot emphasis enough how much your support and guidance mean to me. I could not ask for a better advisor and I owe so much of my professional development to you. Thank you for setting a high standard and for always pushing me to do better and be a more rigorous researcher. I am grateful for all the opportunities you've given me, and for your guidance and advise not only in research but in life. Thank you for always believing in me and never giving up on me. There are ups and downs along the journey, and you have always been so patient with me and gone out of your way to show me that you always have my back. For that, I'll forever be grateful.

I would also like to thank my thesis committee members, Prof. Chris Schuh, Prof. Rohan Abeyaratne, and Prof. Xuanhe Zhao for their valuable advice over the years and for the time you've invested in me. I also want to thank Prof. Tal Cohen and Prof. Zachary Cordero for taking the time to be my thesis readers. Prof. Schuh, I am beyond grateful for your guidance on this project, and for the kindness and support you've showed me throughout the years. Thank you for always taking an interest in my professional development. You've been such an role model to me, and I've learned so much about how to be a good researcher and writer from you. Prof. Abeyaratne, thank you for being on my committee, and for being the most amazing lecturer ever. Your class will always be one of my favorite memories at MIT.

I would like to express my gratitude to Dr. Alan Lai, Dr. Isabelle Crystal and Victor Champagne, and everyone else who has been working on this project for their invaluable work on this project. It has been such a pleasure working with all of you. Alan, you showed me how to be a great researcher and I truly appreciate your support and guidance in this endeavor.

My thanks also go to Beth Marois, Beata Shuster, Lindsay Petrarca from the AeroAstro Department, Marlisha McDaniels from ISN, Alexis Boyer from CAPD, and Janka Moss from ISO. I am extremely grateful for your help and support throughout my time at MIT.

This work would not be possible without all the previous and current members of the Radovitzky group and their continuous and valuable contributions to **ΣMIT**. First I want to extend my gratitude to the postdocs and staff members of the group. Dr. Aurélie Jean, Dr. Martin Hautefille, Dr. Adrian Roselen, Dr. Ryadh Haferssas, Dr. Khai Pham, Dr. Yang Liu, Dr. Bianca Giovanardi and Anwar Koshakji. I learned so much from each of you. Bianca and Anwar, I've learned so much from the both of you, and I am beyond grateful for the kindness and support you both have extended me. Yang, thank you for always looking out for me even beyond MIT and for caring about my career development. To the current and past group members, Alex Mijailovic, Gregoire Chomette, Michelle Xu, Daniel Pickard, Giulia Pozzi, and Chris Quinn, thank you for your friendship. Daniel, I will miss all the discussions we've had throughout the years. I wish you all the best in your PhD study and I am certain that you are growing into an amazing researcher and I cannot wait to see what you achieve next! Greg and Michelle, thank you for being such amazing friends. You have made the last few years of my PhD so enjoyable and I hope we stay in touch! Alex, thank you for always checking in on me and being there for me consistently. The last two years would not have been possible without you. You are an amazing researcher and your dedication to teaching is such an inspiration to me; I know that you will make a great professor one day!

To my group of friends who have been by my side from the very beginning of the journey, Sandro Salgueiro, Mohammad Islam, and Shun Zhang, you have been my support system and I would not able to make it through without you. Sandro and Mohammad, you've been there for me through thick and thin, and I hope our friendship will continue beyond MIT. Shun, thank you for always looking out for me even when you are thousands of miles away. I don't know what I would do without your friendship and support. To my dear friends Chockalingam Senthilnathan, Shashank Agarwal, Ben Zhang, and Ximo Gallud, thank you for your companionship. I will forever remember the good times and the memories we've shared. You've made the grad school experience much more enjoyable. Chocka and Ximo, thank you for your friendship, and I will miss our time together immensely. Shashank, thank you

for always looking out for me. You are such an amazing friend and I've learned so much from you. I cannot wait for us to get together again. Ben, you are an awesome researcher and will make an amazing professor some day. I am so excited to see what the future holds for you! Finally, thank you D, I could not have done it without you.

Lastly, I would like to thank my parents and extended family back home for their unconditional love and support throughout the years. Mom and Dad, I love you and could not have done this without you!

Contents

List of Figures

List of Tables

Chapter 1

Introduction

1.1 Shape Memory Materials and Their Properties

Shape memory materials are a class of materials that can undergo reversible diffusionless transformation from one solid phase to another. These phase transitions only involve a sudden change in lattice structures and crystal symmetries, while atoms in a lattice do not change their relative positions with respect to one another and only alter their distances. This process is known as martensitic transformation, and has been observed in various metallic materials, ceramics and polymers [18, 19, 20, 21, 22]. By virtue of the reversible martensitic transformation, shape memory materials are able to recover their original shape upon heating. This is known as the shape memory effect (SME). They can also exhibit large reversible strains accommodated by the transformation upon cyclic mechanical loading, which is known as superelasticity or pseudoelasticity.

The solid-to-solid first-order phase transformation in a shape memory material is between *austenite* (a high temperature phase) and *martensite* (a low temperature phase), and can be induced by a change of temperature and/or stress. Martensitic transformations in shape memory materials are characterized by four important temperatures: martensite start temperature (θ_{ms}), martensite finish temperature (θ_{mf}), austenite start temperature (θ_{as}), and austenite finish temperature (θ_{af}). These temperatures define the state of the material and whether phase transformation is possi-

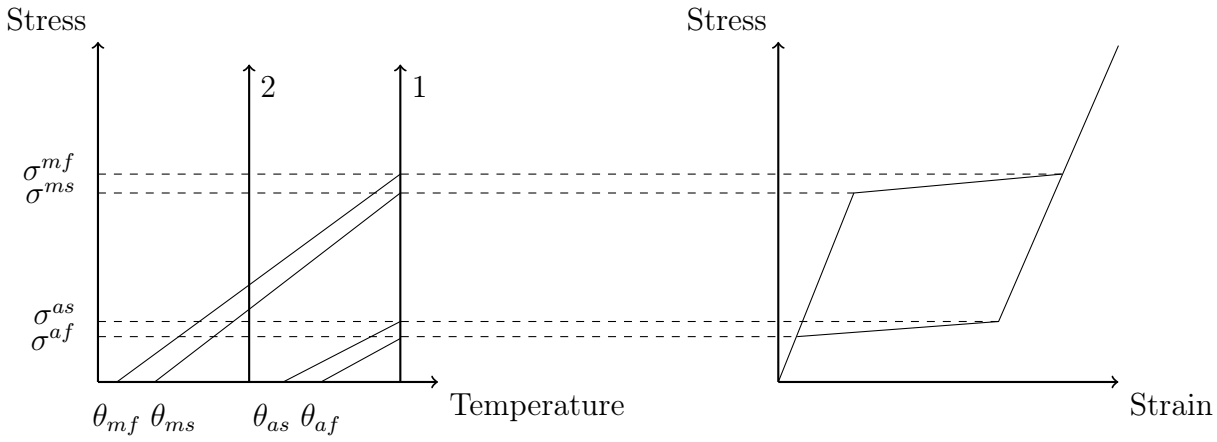

Figure 1-1: Stress-temperature phase diagram and cyclic loading stress-strain response of SMAs.

ble. When the temperature is above θ_{af}, the austenite phase is stable and the material is in the purely austenitic phase as martensite is metastable at higher temperatures. Figure 1-1 shows a typical thermomechanical response of a shape memory material. The vertical line 1 is an example of an isothermal process. At a given temperature $\theta > \theta_{af}$, a shape memory material at the stress-free state will first deform elastically upon loading until the stress reaches a critical value σ^{ms}, at which point the transformation from austenite to martensite (forward transformation) initiates. It is worth noting that the material will undergo plastic deformation or fracture if the stress reaches the critical stress for slip or fracture before transformation. Upon further loading, the material will continue to deform with a very small variation in stress if the transformation is unimpeded until the material is completely in the martensite phase, from where the material will again deform elastically upon further loading. If the loading is removed, the material will first unload elastically from the martensite phase, until the stress reaches a critical value σ^{as} at which point the reverse transformation is activated. Once the reverse transformation is complete and the loading is removed, the material will unload elastically in the austenite phase to the zero-stress state with no residual strain and a full recovery in its original shape. This behavior is known as superelasticity.

The vertical line 2 in Figure 1-1 demonstrates the isothermal cyclic loading process

at a lower temperature $\theta_{ms} < \theta < \theta_{af}$. Upon loading, the aforementioned forward transformation can still happen once the stress reaches the critical value σ^{ms}. It is worth noting that these critical stresses are temperature-dependent as indicated in Figure 1-1. Once the material is completely in the martensite phase, it will deform elastically upon further unloading. However, reverse transformation cannot be initiated upon subsequent unloading to the stress-free state, which will produce a residual strain. This is due to the austenite phase being unstable at lower temperatures, and the material can only recover its original shape when heated above the temperature where austenite is stable, i.e. $\theta > \theta_{af}$. This phenomenon is known as shape memory effect, as the material is able to "remember" its original shape, and the seemingly permanent deformation could only be recovered upon heat treatment.

It is worth pointing out that stress-induced martensitic transformations are not limited to cases where external stresses are applied. Internal stresses can also trigger the martensitic transformation. For example, local internal stresses induced by the initial transformation may subsequently affect the transformation in their neighboring regions.

When a material is undergoing the martensitic transformation, the change of total Gibbs free energy ΔG during transformation can be expressed as follows [23],

$$\Delta G = \Delta G_{\text{chem}} + \Delta G_{\text{el}} + W_{\text{fr}} \tag{1.1}$$

where ΔG_{chem} is the difference in the chemical free energy between the two phases. ΔG_{chem} is negative at temperatures below θ_{ms}. ΔG_{el} is the stored elastic energy associated with the transformation. W_{fr} is the energy dissipated during the transformation due to the internal work to overcome frictional barriers. This irreversible loss in energy accounts for the hysteresis loop observed during transformation, see Figure 1-1. The material stays in the austenite phase if the total change of free energy $\Delta G > 0$, i.e. $|\Delta G_{\text{chem}}| < \Delta G_{\text{el}} + W_{\text{fr}}$. When ΔG is negative, i.e. $|\Delta G_{\text{chem}}| > \Delta G_{\text{el}} + W_{\text{fr}}$, the austenite phase becomes unstable or metastable and the martensitic transformation may happen.

Important properties like superelasticity and shape memory effect observed in shape memory materials have made them promising candidates for a wide range of applications in various industries. The application of shape memory alloys in the biomedical industry can be traced back to the 1970s [24]. SMAs are proven suitable materials for eyeglasses, dental wires, and antennae due to their ability to attain large recoverable strains [25, 26, 27, 28]. NiTi SMAs are especially widely used in the orthodontic field as palatal arches, orthodontic wires/distracters, and endodontic files [29, 30]. Due to their good corrosion resistance and biocompatibility, NiTi SMAs are commonly used in intraspinal implants, venous filters, and neurosurgical stent devices for arteries and veins [29, 30, 31]. Possessing a unique combination of characteristic properties like superelasticity and SME with excellent corrosion resistance, good wear resistance, and low coefficient of friction, shape memory ceramics (SMCs) have attracted a considerable amount of interest in clinical and biomedical applications. Zirconia is especially a material of keen interest in dental restorations as endosseous implants, implant abutments, and ceramic crowns [32, 33, 34]. Zirconia has also been increasingly used as hemoral head components in hip arthroplasty [34].

Shape memory materials are also considered excellent active materials due to their ability to convert a non-mechanical input to a mechanical output, and have found themselves desirable in actuation and sensing applications [35, 36, 37, 38, 39, 40]. SMAs have been widely used as actuators or artificial muscles in various robotic applications since the early 2000s [41, 42, 43, 36]. In the case of ceramic shape memory materials, zirconia-based SMCs particularly have very large transformation stresses on the order of GPa, which are expected to translate into large output stresses when used for actuator applications [44]. Due to the high melting and transformation temperature (can be as high as 1100°C), zirconia-based SMCs are attractive candidates for high-temperature devices in oxidative environment [45, 46]. Transformation temperatures in zirconia-based SMCs can also be controlled when doped with different metal oxides. Doped zirconia is also widely used as oxygen sensors in a variety of applications such as combustion control systems and oxygen generation systems [47]. In addition, shape memory materials are also suitable for force protection and shielding

purposes due to their excellent damping properties [48, 49, 50].

1.2 Oligocrystalline Cu-based SMAs

Cu-based SMAs have attracted much research interest in recent years due to their promisingly low material and processing cost compared to NiTi SMAs. Desirable superelastic properties including large recoverable transformation strains and low transformation stresses are realized to their maximum extent in single crystalline structures. For example, single crystal Cu-based SMAs have exhibited strains as large as 10% prior to fracture. This is attributed to the absence of internal constraints in the form of grain boundaries that limit the extent of the martensitic transformation [2]. San Juan and Schuh [51] quantitatively studied the superelastic cycling responses of micropillars of CuAlNi SMAs. They observed a completely recoverable superelastic behavior in these micropillars with transformation strains above 5%, and that some pillars underwent as high as hundreds of superelastic cycles. By contrast, in polycrystalline forms, superelastic properties are significantly compromised by severe premature intergranular fracture originated at grain boundaries and triple junctions [2, 52]. The deficiency in ductility and severe embrittlement problem observed in polycrystalline Cu-based SMAs have significantly limited their commercial applications.

Recent work has been conducted on the thermomechanical and superelastic responses of Cu-based SMAs with an emphasis on the influence of grain microstructure and grain boundary characteristics on the martensitic transformation [1, 53, 2, 54, 52, 55]. Chen et al. [1] applied a liquid-phase wire forming process and microstructure control technique that significantly improved the ductility limits and prevented premature intergranular fracture in polycrystalline CuAlNi SMAs through the reduction of the grain boundary area and the removal of triple junctions. Specifically, they fabricated Cu-based SMAs in bamboo-shaped thin wire forms, namely oligocrystalline structures. Figure 1-2 illustrates the scanning electron micrographs of two typical CuAlNi oSMA wires produced by Chen et al [1]. The diameters of the bamboo-

shaped oligocrystalline SMAs (oSMAs) wires range from 10 to 150 μm. The wires also have significantly larger grains spanning along the longitudinal axis and less grain constraints in the forms of grain boundaries or triple junctions compared to their polycrystalline counterparts. In a broad sense, oligocrystalline materials refer to those with fewer and coarser grains [56, 57] and larger free surface area relative to the grain boundary area [2]. The absence of grain constraints facilitates an unimpeded phase transformation only seen in single crystals and permits larger recoverable superelastic and shape memory strains, which notably has not yet been observed in bulk polycrystalline CuAlNi SMAs [1]. The grain microstructure of a typical oSMA wire and its mechanical response can be found in Figure 1-3, which is reproduced from the work of Ueland et al [2]. As a comparison, Figures 1-3 (a) and (d) respectively show the stress-strain responses of polycrystalline CuAlNi SMAs [58] and single crystal ones [59] obtained in previous studies. As can be clearly seen, while a single-crystal CuAlNi SMA underwent unimpeded martensitic transformation with a 10% transformation strain, a polycrystal SMA suffered from fracture at a very small strain level before the martensitic transformation was complete. Overall, CuAlNi SMAs of oligocrystalline (Figure 1-3 (c)) and near-oligocrystalline (Figure 1-3 (b)) structures achieved much higher strains and exhibited a clear enhancement in their ductility limits compared to polycrystalline SMAs. In particular, the bamboo-shaped oligocrystal wires with no triple junction can reach rather large strains (as high as 7%), approaching those of a single crystal. Ueland and Schuh [54] conducted experimental study on the transformation behavior and superelastic characteristics of CuZnAl microwires and observed large recoverable strains up to 7.5% in these oSMA wires. They also showed that the fatigue life of CuZnAl can be significantly improved in oligocrystal forms, and that oSMAs may exhibit fatigue lifetimes two orders of magnitude higher than bulk polycrystalline ones. These findings have inspired an important microstructure engineering approach to solve the embrittlement problem of polycrystalline SMAs and achieve desirable single crystal-like mechanical properties while avoiding the high processing cost associated with single crystal production, which will significantly expand the use of Cu-based SMAs to more practical engineer-

ing applications.

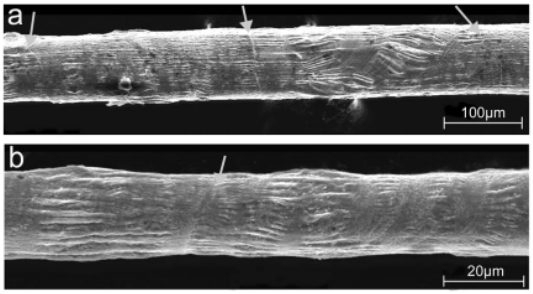

Figure 1-2: Scanning electron micrographs of two CuAlNi microwires showing bamboo grain structure, where grain boundaries are marked by arrows [1].

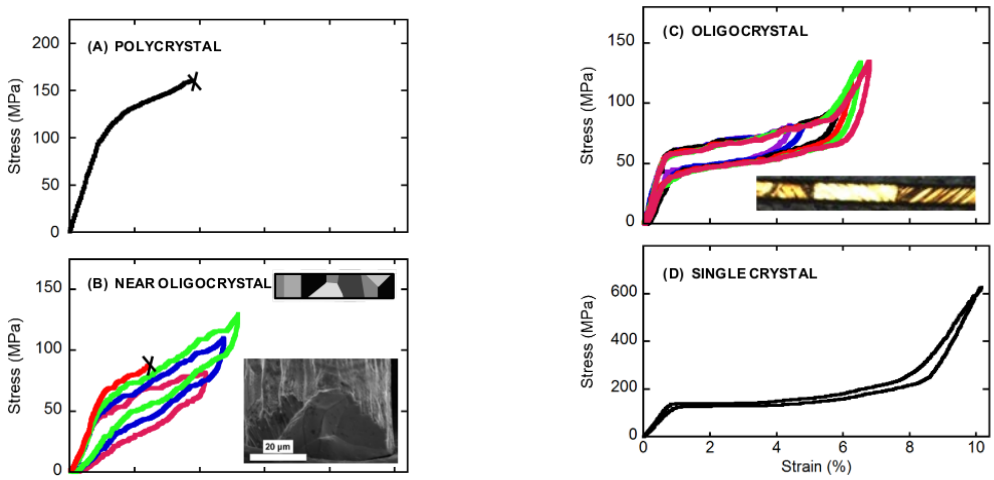

Figure 1-3: Stress-strain curves of Cu-based SMAs in single-crystal, polycrystal, near-oligocrystal and oligocrystal forms. The schematics on the top right corner show the grain structure of the oligocrystal and near-oligocrystal specimens [2]

More recently, the same authors [52] investigated the effect of grain constraints on the martensitic transformation of as-cast oligocrystalline CuZnAl wires. They conducted *in situ* tensile tests on wires with different degrees of microstructural complexity inside a scanning electron microscope, and examined the formation and evolution of martensite variants in different regions of the wires. They observed that the complexity of martensite morphology during transformation increases with increasing grain constraint, in that the martensitic transformation is largely single-variant and complete in the unconstrained monocrystalline region, and multi-variant and partial near grain boundaries. This was attributed to the stress concentrations near

grain boundaries due to incompatibility of transformation strains that emerge at considerably-high levels of strain ($\sim 4\%$). The stress concentrations have the effect of inducing transformation in secondary variants, impeding full transformation and possibly leading to premature fracture near grain boundaries. They also performed finite element simulations using an anisotropic linear elastic constitutive model of CuZnAl wires, which showed the role that incompatibility of elastic deformations due to grain misorientation has in producing large stress concentrations at the grain boundary. This experimental and modeling study suggested that both the elastic and transformation strain incompatibility can be attributed to stress concentration at grain boundaries. An important limitation of the model is the absence of a mechanistic description of the martensitic transformation, and therefore it was unable to ascertain whether the stress concentration is due to elastic or transformation strain incompatibility. Ueland and Schuh [55] also systematically studied the martensitic transformation morphology in CuZnAl microwires in the size range of 21 to 136 μm. They observed a transition from a multi-domain to a single domain martensitic morphology with decreasing diameters of CuZnAl wires. Specifically, in coarser wires, many martensite plates started to nucleate and grow and eventually coalesce with their neighbors as the martensitic transformation progressed. In finer wires, however, only one single martensite plate was formed at the beginning of the transformation and proceeded to grow and propagate in a monolithic manner.

Additional important previous work has also provided potential explanations of the tendency of Cu-based SMAs to fracture along grain boundaries [58, 60, 61, 62, 63, 64]. Miyazaki et al. [60, 61] tested two kinds of bi-crystals groups with both symmetric and random grain boundaries. The symmetric cases showed uninterrupted phase transformation like their single crystal counterparts. In cases of randomly oriented bi-crystals, three samples with incompatible elastic strains fractured along the grain boundary before transformation, whereas one sample with incompatible transformation strains fractured during transformation. From these observations, they concluded that intergranular fracture in Cu-based β phase SMAs is induced by stress concentration at grain boundaries due to either the large elastic anisotropy or to

the difference in transformation strain at grain boundaries, instead of the brittleness of grain boundaries. Sakamoto et al. [58] examined the fracture and fatigue characteristics of polycrystalline CuAlNi SMAs under three different deformation modes; elastic deformation in the austenite state, pseudoelastic/inelastic deformation due to a stress-induced martensitic transformation, and deformation in the martensitic state. They concluded from the experimental results that intergranular fracture in polycrystalline CuAlNi SMAs originated from the formation of stress-induced martensitic transformation. Husain et al. [62] investigated the role of impurities on the segregation of metalloids and consequently intergranular embrittlement in CuAlNi alloys. The experimental results indicated that neither the presence of oxygen due to heat treatment nor grain boundary precipitation of brittle intermetallic compounds like carbides constitutes a significant source of embrittlement. Creuziger et al. [63] investigated the role of grain boundary characteristics on the fracture response with the goal of providing a more comprehensive explanation for grain boundary fracture in polycrystalline CuAlNi. They conducted mode I loading tests to samples with different grain misorientations, and applied the coincident site lattice (CSL) theory to categorize the experimental results. They observed that intergranular fracture did not occur on samples with low angle grain boundaries. It was found that all samples with non-CSL grain boundaries fractured with the exception of one sample that likely had a triple junction near the notch instead of a typical grain boundary. They therefore concluded that grain boundaries with coincident site lattices are capable of accommodating the deformation and prevent premature fracture in CuAlNi. However their CSL analysis is not exhaustive as it did not include samples where grain boundary failure was observed with no visible martensitic transformation on either side of the grain boundary. This suggests that they overlooked the case of elastic incompatibility. In a more recent paper, Dar et al. [64] noticed that intergranular fracture oftentimes occurs before the completion of martensitic transformation in most brittle single-phase polycrystalline samples. They used a grain boundary engineering (GBE) approach to improve the transformation ductility of polycrystalline SMAs. They stimulated the precipitation of a ductile second phase along grain boundaries

to accommodate transformation strain and relieve constraints in adjacent austenite grains by extensive plastic deformation. Their results showed that by relaxing strain mismatch during transformation, one could relieve local stress concentration and reduce the probability of crack nucleation at grain boundaries, and therefore avoid or delay intergranular fracture in polycrystalline SMAs.

1.3 Grain Size Effects in SMAs

Grain size effects were first discovered in Cu-based SMAs in the 1970s [65], and previous work on size effects in SMAs were largely focused on cases where the grain size is considerably smaller than the sample size [66, 67, 68, 69]. Previous studies demonstrated a decrease in the martensite start temperature (θ_{ms}) and an increase in the transformation stress in polycrystalline SMAs with smaller grain sizes [66, 67, 70, 71]. These observations suggested that increasing grain constraints limited the nucleation and formation of martensite plates, and as a result the martensitic transformation was suppressed in samples with smaller grain sizes. In recent years, a number of studies have been carried out to study the grain size effects upon the martensitic transformation and thermomechanical behaviors of SMAs in at micro- and nanoscales and with unique oligocrystal structures.

San Juan et al. [72, 73] investigated the superelastic and shape memory properties in micro- and nano-scale CuAlNi pillars. They showed that both stress- and thermal-induced phase transformation can take place in these finer-scaled pillars in a reversible way. This completely recoverable superelasticity achieved at very fine scales suggested the possibility of designing the next-generation smart micro- and nano-electromechanical systems (MEMS) devices using CuAlNi systems. They also showed that the martensitic transformation and the mechanical damping capacity had strong dependencies on the sample size [73]. Specifically, they observed that both the martensite and austenite phases were more stable in the nanopillars than in their bulk counterparts, and both the hysteresis loop in the stress-strain curve and the superelastic cycling ability in a nanopillar were significantly larger than in a

bulk CuAlNi SMA. Chen and Schuh [53] showed that in oligocrystalline CuAlNi wires with a bamboo grain structure, both the stress hysteresis upon mechanical loading and the temperature hysteresis upon thermal loading increased as the wire diameter decreased from $100\mu m$ to $20\mu m$. They proposed several possible origins of the observed size effects including surface energy, stored elastic energy, interfacial energy, acoustic emission, heat transfer, and internal friction. After evaluating each factor, they concluded that the size effect observed in larger SMA samples can be attributed to the sluggish heat transfer in larger specimens, while the size effect observed in CuAlNi SMA microwires was due to the enhanced dissipation of frictional energy in the free surfaces of smaller wires.

More recently, Ueland and Schuh [55] related the size effect on transformation hysteresis observed in CuZnAl microwires to the morphological evolution of martensite. The experimental results suggested that the sampling of defects and obstacles met by the transformation front as it propagated along the wire changed with sample size. Specifically, the transformation front encountered more obstacles on a per volume basis in finer wires, which lead to a larger amount of frictional energy dissipated and larger hysteresis size. In [74], the authors explored the effects of sample size of CuAlMnNi wires on the thermal-induced phase transformation, and in particular on the martensitic transformation ranges and the stored elastic energy. They observed that smaller wires responded faster to temperature change and the stored elastic strain energy during martensitic transformation was proportional to the wire diameter. More importantly, they showed that the macroscopic strain during the thermal-induced martensitic transformation was independent of wire diameter in the absence of external stress, while the strain increased with decreasing wire diameter in the presence of external stress. These results suggested that thermal-induced martensitic transformations and superelastic properties in SMAs were enhanced in finer wires.

1.4 Zirconia-based Shape Memory Ceramics

Historically, the work on shape memory materials has been mostly focused on metallic materials like Cu-based and NiTi SMAs. Recent work [11, 75, 6, 76, 77, 78] has notably expanded the study from metals and alloys to martensitic ceramics, with significant research interest on the shape memory effect and superelasticity in small volume shape memory materials such as micropillars of zirconia-based SMC [11, 75, 6, 76, 77, 78] and microparticles [79, 80].

Similarly to their metallic counterparts, SMCs can also undergo a reversible diffusionless solid-to-solid phase transformations from austenite to martensite at the crystal level. Among various shape memory ceramic materials, zirconia-based ones have attracted much research interest in recent years for a number of reasons. First of all, zirconia has a very well-studied and well-characterized martensitic transformation between a tetragonal austenitic phase and a monoclinic martensitic phase [81, 15, 82, 83, 19, 5, 7, 84, 85, 86]. They can also be fabricated by conventional ceramic processing techniques [87]. By doping with different oxides, zirconia-based SMCs are able to achieve a wide range of transformation temperatures, which makes them attractive candidates for a variety of applications especially in high-temperature environments [6]. Shape memory behaviors were first demonstrated in polycrystalline zirconia-based ceramics in the 1980s [19, 3, 88], and early research interest was largely focused on the transformation toughening in zirconia-based ceramics [4, 89, 90, 91, 92]. Polycrystalline zirconia is known to suffer from premature fracture at very small strain levels, which results in very limited superelastic effect. Figure 1-4 is adapted from the work in [3]. As can be seen, while good superelastic properties can be observed in the first few loading cycles, further loading induces a degradation of superelastic properties and eventual failure. In polycrystalline zicornia-based SMCs, the degradation of shape memory and superelastic properties is due to shape distortions in adjacent crystal grains being incompatible with one another, inducing large mismatch stresses and triggering fracture along grain boundaries. This embrittlement problem has severely limited the application of these materials in engineering practice.

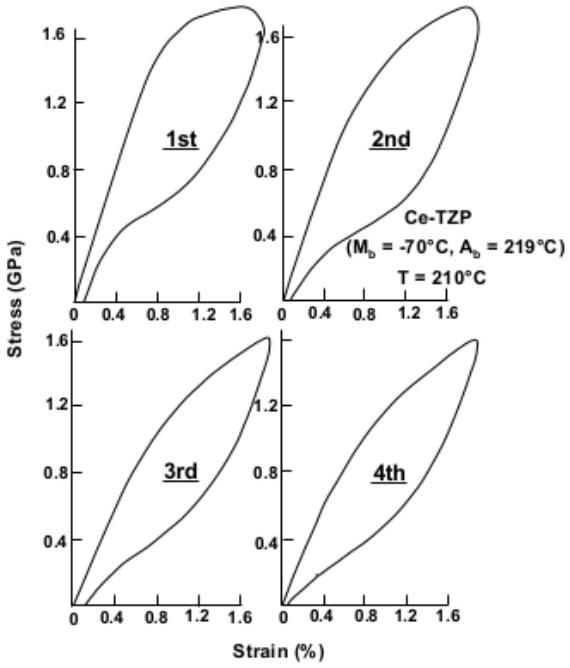

Figure 1-4: Axial superelastic stress-strain curves for CeO_2-ZrO_2 showing diminishing hysteresis with each cycle, the 5th cycle resulted in failure [3]

As discussed in the previous section, the issue of stress concentration and potential intergranular fracture due to grain boundary constraints is well studied in metallic shape memory materials. In SMCs, strain incompatibilities at grain boundaries is far less studied, although recent work has provided significant insights on this issue [93, 94, 95, 96]. Pang et al. [93] investigated the two-dimensional compatibility of the martensite-austenite interface via the application of the cofactor conditions as a possible factor controlling the cracking of bulk polycrystalline zirconia-based SMCs. The results suggested that samples with excellent interface compatibility may avoid cracking during thermal cycles and that bulk compatibility was not necessarily the dominant cause of transformation-induced fracture. Pang et al. [94] later studied the role of grain constraints on the martensitic transformation in ceria-doped zirconia (ZrO_2-CeO_2). They characterized and analyzed the thermally-induced transformation in ZrO_2-CeO_2 oligocrystalline powders and sintered pellets. They observed large compressive strains in ZrO_2-CeO_2 pellets due to the pressure build-up at grain constraints and that transformation temperatures were depressed in ZrO_2-CeO_2 pellets but not in powders. In [95], Crystal et al. studied the role of grain boundaries in

the damage evolution of yttria-doped zirconia (Y_2O_3-ZrO_2) SMCs subject to cyclic thermal loading. The authors demonstrated that one can suppress cracking and avoid intergranular fracture in single crystal Y_2O_3-ZrO_2 in the micro- to the millimeter scale by removing grain boundary constraints through careful microstructural control. The same authors later investigated the grain size effect on intergranular cracking in 1.5 mol% Y_2O_3-ZrO_2 in pellet forms [96]. The experimental results showed that smaller grained samples required more thermal cycles to achieve full disaggregation, and the total heat release associated with cracking increased with increasing grain boundary area and decreasing grain size. These important previous work shed light on the martensite-austenite interface compatibility and thermally-induced transformation in zirconia-based SMCs. However, comprehensive study on the mechanism of stress-induced transformation and bulk compatibility in zirconia-based SMCs is still lacking.

In this work, we concentrate on the stress-induced transformation as it is relevant to superelasticity and shape memory materials' mechanical damping properties. The main goal of this work is to improve our understanding of the sources of grain boundary incompatibility in zirconia-based SMCs. This can help identify grain boundary configurations that increase the superelastic range of SMCs in oligocrystalline or polycrystalline forms.

1.4.1 Martensitic Transformation in Zirconia-based SMCs

To better understand strain incompatibilities at grain boundaries in SMCs and in support of interpreting previous experimental studies, in this work we take on the task of characterizing the martensitic transformation in zirconia-based SMCs through the development of crystal-level models. This requires the fundamental description of the martensitic transformation that is specific for zirconia-based SMCs at the single-crystal level. In this section, we review the basics of the martensitic transformation in zirconia-based SMCs and the variant selection process, and examine the resulting austenite/twinned-martensite interface (habit plane) microstructure.

Zirconia can exist in three phases: the monoclinic phase is stable at temperature

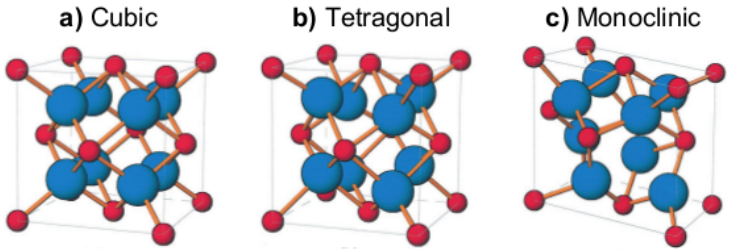

Figure 1-5: The three polymorphs of ZrO_2 and the corresponding space groups: (a) cubic, (b) tetragonal, and (c) monoclinic. Adapted from [4]

Temperature ($°C$)	Phase	Lattice Parameters
30	Monoclinic	a= 5.1415, c= 5.2056, c= 5.3128, $\beta = 99°18'$
1393	Tetragonal	a= 3.6526, c= 5.2928
2400	Cubic	a= 5.272

Table 1.1: Lattice parameters of pure zirconia at room temperature and at elevated temperatures [14, 15]

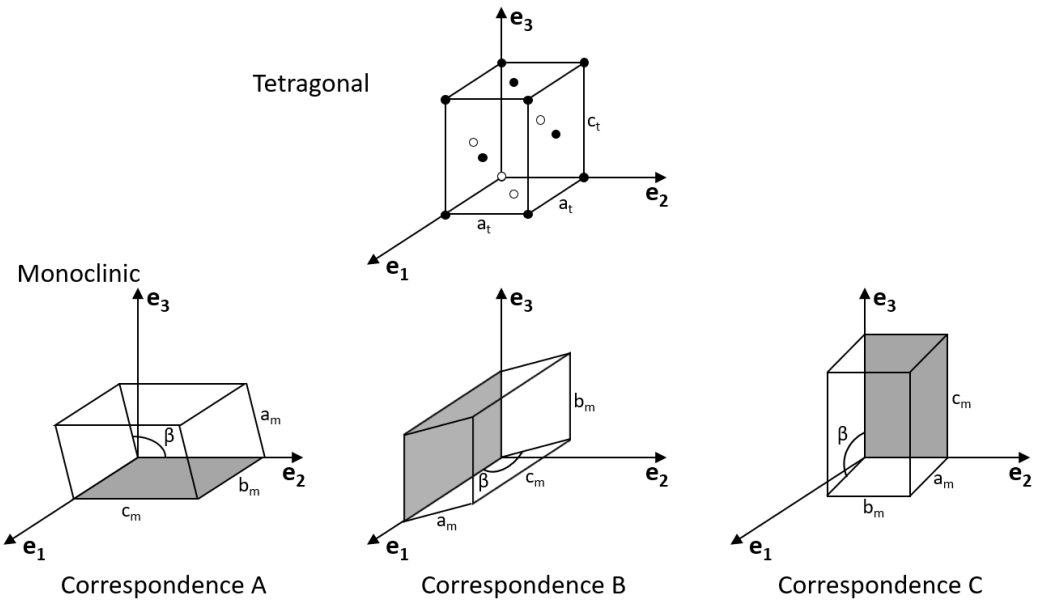

Figure 1-6: The tetragonal unit cell and three different monoclinic correspondences. Adapted from [5, 6]

T<1170 °C, the tetragonal phase is stable at 1170 °C<T< 2360 °C, and the cubic phase is stable at T> 2360 °C [86]. The schematic illustration of crystal structure and lattice parameters of each phase in a pure zirconia can be found in Figure 1-5 and Table 1.1 [14, 15], respectively. Though the cubic-to-tetragonal transformation was

observed in zirconia systems [97], the martensitic transformation in zirconia normally refers to the transition from the tetragonal to monoclinic phase. This transformation is accompanied by a significant shear strain about 8% as well as a volume change about 4%. The transformation is usually described by the lattice correspondence between the tetragonal unit cell and the resulting monoclinic unit cell. There are three possible paths through which the tetragonal cell can become the monoclinic cell, see Figure 1-6. While each path produces an identical final monoclinic cell, the paths differ on whether the tetragonal long axis c_t becomes the monoclinic axis a_m, b_m, or c_m. These different paths are referred to as correspondences A, B and C, respectively. This notation system where correspondences are named based on which monoclinic axis is derived from the unique tetragonal axis (c_t) was proposed in [98], and it is worth noting that this system lacks the ability to distinguish different variants of a particular correspondence. The notation of correspondences is not unique.

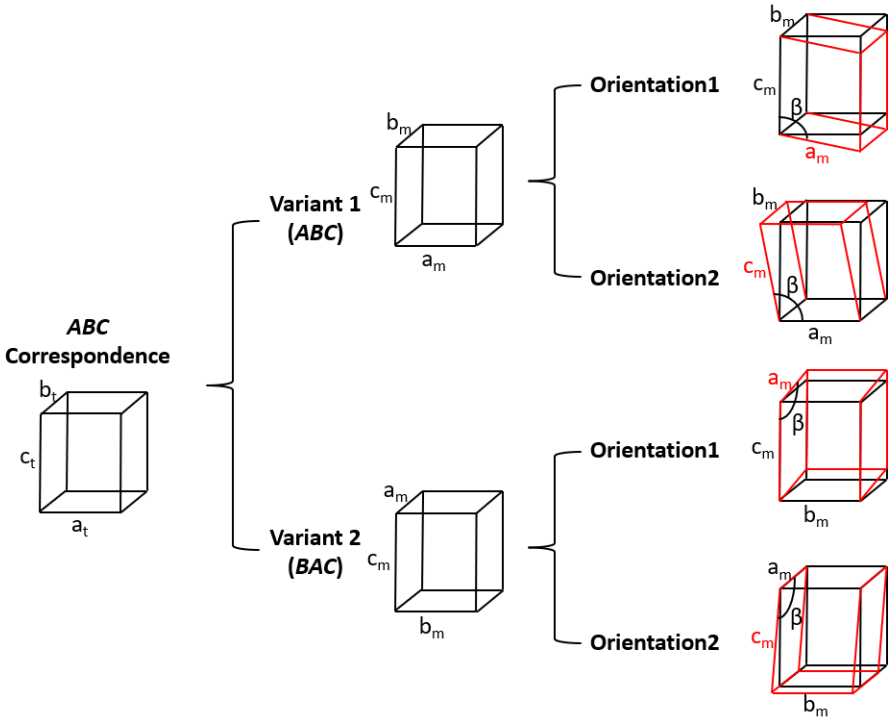

Figure 1-7: Different variants and orientations of correspondence ABC. Adapted from [7, 8, 9, 10]

In [8, 9, 10], the authors introduced a new notation system that allowed all the different variants of a correspondence to be identified and labeled. The correspon-

dences are described based on which atom of the parent phase becomes which atom of the product phase, an example can be seen in Figure 1-7. As can be clearly observed, there are two crystallographically equivalent variants related by a rotation for each correspondence. For example, if the transformation happens through the correspondence where axis c_t becomes b_m, there are two possibilities for axes a_t and b_t: (1) a_t to a_m and b_t to c_m; or (2) b_t to a_m and a_t to c_m (using a right-handed set of axes), which can be represented by ACB and CAB to distinguish variants in transformation. For each variant, there are two options for the axes c_m and a_m to align with the parent phase: (1) a_m becomes parallel to its counterpart parent axis and c_m become inclined; or (2) c_m becomes parallel to its counterpart parent axis and a_m become inclined, see Figure 1-7. In summary, during the transformation from the tetragonal to monoclinic phase, each of the three correspondences has two variants, and each variant has two orientations, which results in 12 possible lattices in the monoclinic phase for each tetragonal lattice. This information is crucial for the development of micromechanics models of phase transformation, as the model needs to capture all possible variants in order to correctly characterize the martensitic transformation in zirconia. From an energy minimization perspective, correspondences B and C are more favored during the variant selection process because they have the smallest Bain (transformation) strain and lattice invariant strain, respectively [5]. Meanwhile correspondence A has the largest Bain strain therefore is considered the least favorable for transformation and rarely seen in experiments [86]. The preference among correspondence B and C will be discussed in greater detail in the following section. This discussion on variant selection is of great importance, as identifying the transformation strain tensor that converts a tetragonal unit cell to a monoclinic unit cell is the starting point for calculating theoretical transformation strains and austenite/martensite interface (habit plane) orientations. Provided with this information, we later undertake the task of calculating the transformation systems in zirconia using the geometrically nonlinear theory of transformation which will be described in Chapter 2 with the knowledge of the lattice parameters provided by our collaborators [6]. The results are interesting and worth further discussion as the theory furnishes 24 habit planes (as shown in

Table 2.2) in case of correspondence B, while no habit plane can be obtained via correspondence A and C. This itself calls for further investigation as it indicates a stark contrast between the martensitic transformation along different paths when one searches for possible habit planes and will be discussed carefully later.

1.4.2 Orientation Effects and Non-Schmid Behavior in Single-crystal Zirconia

The mechanical response of zirconia-based SMCs and its dependency on different grain properties have been thoroughly studied in recent work [11, 75, 6, 76, 77, 78]. In [76, 6], the authors extensively studied the orientation dependence of zirconia micro-pillars. They conducted micro-compression tests of 43 micro-pillars whose grain orientations were identified using EBSD. All the pillars were based on the same phase composition with diameters close to 1.2 μm to avoid size effects, and only differed in crystallographic orientations. The results of micro-compression tests exhibited a wide variety of mechanical responses among these pillars. They showed that not all of the pillars underwent martensitic transformation under compression; some pillars fractured while others showed signs of plastic slip. The critical transformation stress, transformation strain, and loading elastic modulus were measured for each pillar. Among the 31 pillars that underwent martensitic transformation, a wide range of critical transformation stresses from 0.58 to 8.7 GPa were observed, which indicates that the critical stress depends strongly on the crystallographic orientation. This phenomenon is well studied in shape memory alloys like NiTi and CuAlZn where phase transformation is shear-dominated and Schmid's law can be applied to predict the orientation-dependence of transformation stress. In [6], extensive efforts went into understanding the orientation-dependence of transformation stress in zirconia-based SMCs. They first assumed that phase transformation in zirconia is shear-dominated as is the case for most shape memory alloys, therefore the shear stress required to activate transformation σ_{shear} can be related to the Schmid Factor (SF). They also investigated the relationship between the experimentally measured transformation

stress and theoretical SF for different crystallographic orientations. It is worth mentioning that correspondence A was neglected in the discussion as it is not favored thermodynamically for transformation as discussed in the previous section, and only correspondences B and C and their combination were examined in [6]. Their results showed a lack of good alignments of SF and transformation stress when considering martensite variants derived from correspondence B or a combination of correspondences B and C. Interestingly, results obtained from considering correspondence C alone revealed a better fit, which as mentioned in the previous section, contradicts the nonlinear theory of martensitic transformation. Still, the results obtained from only correspondence C were not very satisfying, which strongly indicated that the maximum resolved stress criterion was not sufficient to explain the orientation-dependence of transformation stress in zirconia. With the resolved stress criterion being insufficient, they postulated that the non-Schmid effect might be related to the experimental observations that the martensitic transformation in zirconia was accompanied by a rather large volume change [6]. To this end, they proposed to incorporate a normal effect in the transformation criterion by adding a normal component to adjust the calculation of SF. However, this was also proven insufficient as the results showed that for only some orientations would the addition of the normal factor have a significantly positive affect, and in particular it affected orientations with low Schmid factors, among which many were fractured and slipped. In fact, the effect of the additional normal factor on transformed pillars was shown to be marginal, as the fitting result were almost identical to that using the resolved stress criterion. One possible explanation is that the same weight was assigned to the normal and shear component while evaluating SF in the transformation criterion while the relation is likely to be much more involved. These discrepancies between the nonlinear theory and experimental results call for a more detailed study on the non-Schmid effect in the transformation response of zirconia-based SMCs, which we will later take on.

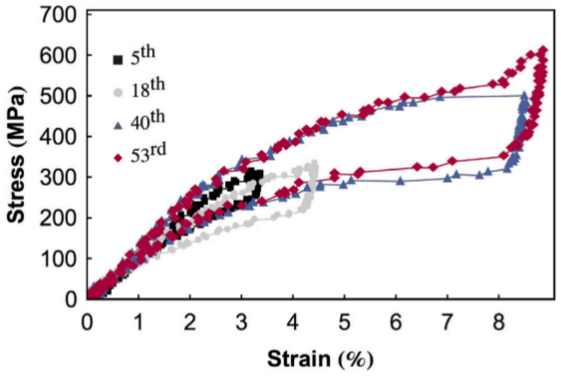

Figure 1-8: Superelastic stress-strain curves for a pillar cycled 53 times with d_{eff} = 1.1 μm, produced in [6]

1.4.3 Shape Memory Ceramics in Small Volumes

Towards the goal of manufacturing high-strength robust ceramics through microstructural design to fully realize their superelastic properties and avoid intergranular fracture, recent development in zirconia-based SMCs [11, 75, 6, 76, 77] has demonstrated that that shape memory properties can be preserved in polycrystalline structures by applying microstructure control techniques to reduce grain boundary constraints and consequently reduce stress concentrations at grain boundaries. The authors showed that catastrophic cracking and failure in SMCs can be suppressed when made into small volumes (on the order of a few cubic microns) with few crystal grains and less grain boundaries constraint. The concept behind the design is that oligocrystalline and near-oligocrystalline structures will effectively relieve the stress concentration generated by martensitic transformation and mismatch between neighboring grains, therefore permitting cyclic transformation without cracking.

Lai et al. [11] manufactured zirconia micro-pillars that are able to withstand dozens of transformation cycles at significant strain levels of several percent (one pillar withstood 53 superelastic cycles and more than 7% strain), as shown in Figure 1-8. This indicates a great improvement over polycrystalline superelastic zirconia that can only endure several cycles before catastrophic failure. Notably, zirconia-based SMCs also demonstrate great energy absorption properties, with the energy dissipation upon cyclic loading significantly larger than that in conventional metallic

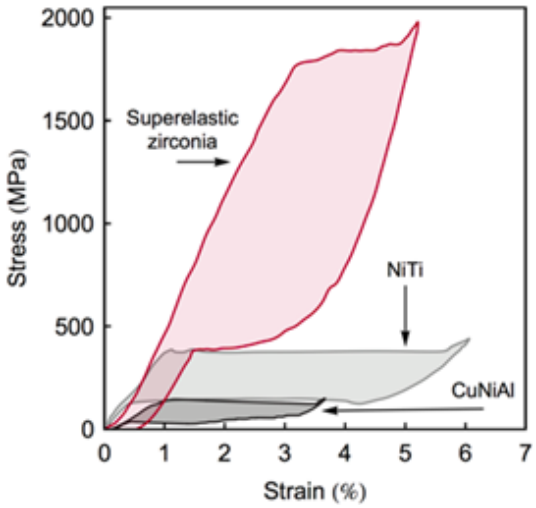

Figure 1-9: Superelastic zirconia micro-pillars dissipates more energy than shape memory alloys like NiTi and CuNiAl due to its higher transformation stress [11]

shape memory materials [11]. Figure 1-9 is reproduced from [11], and shows stress-strain curves of superelastic zirconia along with SMAs like NiTi and CuNiAl. The area within the stress-strain curve indicates the characteristic energy dissipation hysteresis of each material. It can be observed that zirconia has much higher strength which leads to a particularly large total energy dissipated in a superelastic cycle. In [95], the authors showed that polycrystal SMCs at the millimeter size scale exhibit highly reversible transformation behavior over as many as 35 cycles, and their energy dissipation ability also converges with that of the single-crystal structure.

1.5 Previous Work on Numerical Modeling of Shape Memory Materials

There has been significant research interest in developing suitable constitutive models for shape memory materials in the past few decades, as thoroughly reviewed in [99, 100, 101, 102]. Early efforts were largely directed towards one-dimensional models that can adequately capture the characteristics of martensitic transformation in shape memory materials [103, 104, 105]. The last few decades have also seen intense efforts in the development of continuum models of martensitic transformation

to describe the complex thermomechanical behavior of various shape memory alloys at single crystal levels [106, 107, 108, 109, 110, 111, 100, 101, 102, 112, 113, 114, 115]. Among them, micromechanics-based models [107, 109, 110, 111, 115, 116] incorporate details of the crystallographic microstructure of martensite into the continuum mechanics framework, and therefore are particularly suitable for modeling material response under multi-axial stress states and material behavior such as the nucleation and localization of martensite variants, austenite/martensite interface motion, and growth of martensite plates. Micromechanics-based information like the orientation of a habit plane and transformation strain can be identified by the crystallographic theory of the martensitic transformation [117, 118, 119] or the geometrically nonlinear theory of martensite [120, 5, 121, 7, 122]. To allow for finite deformations in the initially crystallographic-textured NiTi SMAs, Anand and several different coauthors developed a rigorous continuum mechanics framework for micromechanics-based anisotropic constitutive models [111, 109, 110]. Guided by the similarity between phase transformation and crystallographic slip in the crystal plasticity framework, they developed a set of flow rules and transformation conditions based on modifications of the crystal plasticity theory [123], and transformation systems are calculated based on the geometrically nonlinear theory of martensite. Thamburaja and coauthors later extended the finite deformation model to account for martensitic reorientation and detwinning [124, 125]. Micromechanical models have also proven instrumental for modeling the material response under multi-axial stress states. Several authors obtained accurate predictions of macroscopic mechanical behavior of SMAs [126, 127, 128, 129, 107, 130, 131, 132]. Several other authors have also incorporated features including self-accommodation, variants interactions, reorientation and detwinning, and transformation-induced plasticity in the micromechanics models [133, 134, 135, 16, 136].

Another important part of the numerical works on SMAs has focused on the macroscopic and phenomenological modeling of phase transformation in SMAs [137, 108, 138, 106, 113, 112, 114, 139]. Though these models were successful in predicting the macroscopic stress-strain response of various SMA systems, they are not

able to provide detailed information on the phase transformation, or to assess the effects of initial textures, grain orientations and grain boundaries (GBs). In the past few decades, there has also been a surge of research interest in developing microscopic modeling approaches such as atomistic modeling and molecular dynamics (MD) [140, 141, 142, 143, 144, 145, 146]. MD simulations are proven useful for addressing the shortcomings of continuum mechanics-based models, in that they are able to capture atomic-level information of the deformation twinning and phase transformation. However, the utility of MD simulations is limited by two major challenges: MD requires small time steps and simulation timescales for numerical stability, and the accuracy of MD simulations depends highly on the choice of the interatomic potentials. In recent years, phase field modeling (PFM) [147, 148, 149, 150, 151] has also emerged as a powerful tool for simulating the morphological evolution of martensite microstructures in SMAs at the mesoscopic scale. Phase field models assume a set of field variables that are continuous across the interfacial regions to describe a multidomian microstructure. Instead of explicitly describing the motion of individual atoms, evolution equations of these field variables are obtained based on general thermodynamics and kinetics principles. As a result, phase field models require the knowledge of material specific properties based on experimental and theoretical studies. A review on phase field modeling of the martensitic phase transformation can be found in [148].

Compared to SMAs, there have been far fewer continuum models for SMCs and efforts have largely gone into the development of atomistic or phase field models. A comprehensive review of computational models for SMCs can be found in [152]. Zhang and Zaeem [153, 154, 155, 156, 157] conducted extensive studies of various aspects of inelastic deformation of single crystalline yttria-stabilized tetragonal zirconia (YSTZ) nanopillars by means of MD simulations including different deformation mechanisms, orientation-dependency, grain size-dependency, and the influence of pre-existing defects. In [154], Zhang and Zaeem conducted MD simulations to investigate the effects of grain boundaries on phase transformation, dislocation emission and the mechanical properties of yttria-stabilized tetragonal zirconia (YSTZ) bicrystalline nanopillars.

They showed that grain orientations as well as grain boundary orientations with respect to the loading direction resulted in different deformation mechanisms such as amorphous phase formation, dislocation emission and martensitic phase transformation in YSTZ.

Phase field models have also been proven successful in modeling martensitic transformation in zirconia-based SMCs [158, 159, 160, 161]. Various types of phase field models have been developed for tetragonal to monoclinic transformation in zirconia where different thermodynamic potentials and order parameters are used. In particular, in [160] a three-dimensional phase field model for tetragonal-to-monoclinic transformation in zirconia was proposed. The model took into account all possible martensite variants from different correspondences and was used to study the formation of a monoclinic embryo in a tetragonal single crystal. Their model is shown to successfully capture the variant selection process based on the minimum formation energy and the effect of variant strain accommodation during the tetragonal-to-monoclinic transformation. They also reproduced the microstructural patterns and the morphological evolution of martensite observed in experiments. In [161], the authors combined a variational formulation of crack propagation with a two-dimensional phase field model of tetragonal-to-monoclinic transformation. The model was employed to study crack growth in a single crystal tetragonal zirconia.

1.6 Thesis Objectives and Approach

The background material and discussion presented so far in Chapter 1 suggest that shape memory and superelastic properties in shape memory materials can be significantly improved when the microstructure is properly controlled. This speaks of the great potential to improve the performance of brittle shape memory materials and achieve the attractive properties of single crystals such as high strength and refractory properties through integrated computational materials engineering (ICME) [162]. It is also clear that there is a significant knowledge gap in the microstructure engineering and in characterizing the micromechanical responses of oligocrystalline and single

crystalline SMAs and SMCs, and a number of outstanding research opportunities exist for advancing our understanding of this field. To better utilize microstructure engineering techniques to eliminate the brittle intergranular fracture commonly seen in shape memory materials, it is imperative to improve our understanding on the role of grain boundary as sources of deformation incompatibilities in shape memory materials in polycrystalline forms.

The overarching goal of this thesis is to comprehensively study the competition between phase transformation, grain boundary constraints, and their potential effect on intergranular fracture in shape memory materials through comprehensive computational modeling. To this end, we first established a numerical framework for modeling the martensitic transformation at the continuum level incorporating micromechanical information. We implemented an anisotropic rate-dependent constitutive model of phase transformation based on the three-dimensional constitutive framework for single-crystal SMAs developed by Anand and Gurtin [111] and Thamburaja and Anand [109]. Notably, we adapted the model to take into account the non-Schmid effect observed in zirconia-based shape memory ceramics [6], which to our knowledge has not been done in previous finite element-based models. The model adopts the geometrically nonlinear theory of transformation to account for transformation strains of different martensitic variants [120], and captures both the elastic and transformation anisotropy, and thus enables a full description of the effect of incompatibilities arising at grain boundaries on the mechanical response for arbitrary grain misorientations. We applied the theory to identify all admissible transformation systems in a single-crystal Cu-based SMA and zirconia-based SMC, based on the knowledge of lattice parameters. In the case of SMCs, the model was calibrated against micro-pillar compression tests presented in [76, 6], and subsequently used to verify the orientation-dependence of transformation stress and strain. We then conducted high-resolution three-dimensional finite element simulations to explore and understand strain incompatibilities at grain boundaries due to both elastic and transformation anisotropy in both materials with general misorientations. The simulation results provide important insights on the origins of incompatibilities at grain boundaries due to both

elastic and transformation anisotropy in samples with general misorientations. We also showed that this approach could be used to explore the misorientation space for quantifying the level of elastic and transformation incompatibility at any grain boundaries. We also demonstrated that there is a clear correlation between grain boundary characteristics such as disorientation angles and different types of incompatibilities. This can help with understanding the sources of incompatibility and brittleness in shape memory materials and provide an approach to material design based on ICME.

The organization of this thesis is as follows. In Chapter 2, the modeling framework in this thesis is described. We first provide a detailed derivation of the rate-independent anisotropic constitutive model for SMAs closely following the derivation in [111, 109, 124]. We proceeded with a rate-dependent constitutive model for the sake of efficiency and simplicity in terms of numerical implementation. We also provide algorithmic details of the robust explicit time integration scheme developed to update the constitutive law.

In Chapter 3, utilizing the micromechanical modeling framework, we conducted finite element simulations in support of interpreting the experimental results of Cu-based fine wires with bamboo-shaped oligocrystalline microstructure obtained in [2, 52]. We studied tensile response in bi-crystal oSMA wires of arbitrary grain misorientations. Among these simulations, we identified two distinct cases representative of two different configurations, one in which there is significant elastic incompatibility, and another one in which there is significant transformation incompatibility. The simulation results provide insights on the competing mechanisms of elastic and transformation incompatibility leading to intergranular fracture in the oligocrystalline structure. The simulation results allowed the identification of misorientations that reduce or minimize elastic and transformation incompatibility, as well as provided some explanations of the tendency of Cu-based SMAs to fracture along grain boundaries. We then investigated the correlation between different types of incompatibilities and grain boundary characteristics including the disorientation angle and coincidence site lattice (CSL).

In Chapter 4, we first calibrated the constitutive model against the micro-pillar

compression tests in [6, 76]. We then conducted a series of finite element simulations to investigate different types of strain incompatibilities arising at grain boundaries in zirconia using the calibrated model, followed by analysis and discussion of the results. The simulation results provide detailed information on the nucleation and evolution of martensite variants and stress distribution at grain boundaries. The results also shed light on on the competing mechanisms of elastic and transformation incompatibilities leading to severe stress concentration at the grain boundaries. We then explored the misorientation space for quantifying the level of elastic and transformation incompatibilities at SMC grain boundaries, as well as the correlation between different types of incompatibilities and several grain boundary characteristics.

The thesis closes in Chapter 5 with conclusions and recommendations for future work.

Chapter 2

A Micromechanical-based Modeling Framework

In this chapter, anisotropic rate-dependent constitutive models for single-crystal SMAs and zirconia-based SMCs are proposed. The models are built upon the general continuum framework for describing martensitic transformations at the single-crystal level proposed by Anand et al [109, 110, 111, 125]. This framework requires the identification and geometric description of the transformation systems pertaining to the specific crystal structure of the material. The geometric characteristics of the transformation systems for martensitic transformations are defined by the normal to the austenite-martensite interface plane (habit plane), $\mathbf{m}_0^i$, and the transformation strain direction vector $\mathbf{b}_0^i$, where i is the index of the existing transformation systems. These quantities can be computed from the geometrically nonlinear theory of martensite [120, 5, 7, 122] based on the crystal structure of the austenite and martensite phases of the material and the lattice parameters in both phases.

It is worth mentioning that the martensitic transformation in zirconia not only involves lattice shear as in most SMAs, but it is also accompanied by a significant volume change ($\sim$4%) [88]. From a micromechanics perspective, transformation systems in zirconia are non-orthogonal and this results in a non-Schmid effect during the transformation. In order to take into account the normal deformation in each transformation system which is responsible for the volume change, we adapted the

formulation in [12] developed for crystalline silicon. A robust explicit algorithm is developed to update the constitutive law. The formulation of the constitutive model follows closely the presentation in [111]. The model was incorporated in our in-house computational framework **ΣMIT** developed by the research group of Raúl Radovitzky to perform large- scale and high-resolution finite element simulations [163, 164, 165]. In this chapter, we summarized the main steps in the constitutive formulation. We also provide algorithmic details of the robust explicit time integration scheme we implemented to update the constitutive law.

2.1 Anisotropic Rate-dependent Constitutive Model of Single-Crystal SMAs

A single-crystal micromechanics-based model is implemented to provide a full mechanistic three-dimensional description of the anisotropic elastic as well as martensitic transformation stress-strain response in shape memory materials. The model is based on the three-dimensional constitutive framework for single-crystal SMAs developed by Anand and several co-authors [111, 109, 110]. The authors developed the model by modifying the widely-used framework for crystal plasticity by crystallographic slip, and assuming the similarity in the inelastic deformation during the martensitic transformation and dislocation-based plastic deformation. The model takes into account the elastic anisotropy as well as the anisotropy from the transformation strains and therefore is able to capture different grain orientations and crystallographic textures. Though the model does not explicitly account for the atomic-level fine-scale microstructures of martensite, the model is able to track the evolution of volume fractions of different martensite variants via the geometrically nonlinear theory of martensite.

The anisotropic constitutive model is derived and summarized in the following sections, closely following the derivation in [111, 109, 124].

2.1.1 Kinematics

In this work we adopt the standard continuum mechanics notation, and an entire single crystal is chosen as a representative-volume element (RVE). Considering a material point $\mathbf{X}$ in the reference configuration in a homogeneous crystalline body B, a motion of B maps the material point $\mathbf{X}$ to $\mathbf{x} = \boldsymbol{\varphi}(\mathbf{X}, t)$ in the deformed configuration. The deformation gradient $\mathbf{F}$ is a tensor that maps segments $\mathbf{dX}$ in the reference configuration to segments $\mathbf{dx} = \mathbf{F}\mathbf{dX}$ in the deformed configuration. The deformation gradient $\mathbf{F}$, velocity $\mathbf{v}$ and velocity gradient $\mathbf{L}$ are defined as:

$$\mathbf{F} = \nabla\boldsymbol{\varphi} \qquad \mathbf{v} = \dot{\boldsymbol{\varphi}} \qquad \mathbf{L} = \mathrm{grad}\mathbf{v} = \dot{\mathbf{F}}\mathbf{F}^{-1} \tag{2.1}$$

where ∇ and grad are the gradient with respect to the material point in the reference configuration, and the gradient with respect to the material point in the deformed configuration, respectively.

We base the model of the martensitic transformation on a multiplicative decomposition of the deformation gradient,

$$\mathbf{F} = \mathbf{F}^e\mathbf{F}^p \tag{2.2}$$

where the elastic deformation gradient $\mathbf{F}^e$ represents the mapping of segments $\mathbf{dl}$ in the relaxed lattice configuration due to the stretching and rotation of the lattice, and $\mathbf{F}^p$ represents the mapping of segments $\mathbf{dX}$ to segments $\mathbf{dl} = \mathbf{F}^p(\mathbf{X})\mathbf{dX}$ in the relaxed lattice configuration due to the nucleation and growth of the austenite/fine-twinned martensite structure.

The elastic and phase transformation velocity gradient can be obtained by taking the time derivative in Eq. 2.2,

$$\dot{\mathbf{F}} = \dot{\mathbf{F}}^e\mathbf{F}^p + \mathbf{F}^e\dot{\mathbf{F}}^p \tag{2.3}$$

[0] $\mathbf{F}^p$ is not the plastic part of the deformation gradient as is normally used in the plasticity theory and the subscript p is for phase transformation.

where the elastic and phase transformation velocity gradient are defined as follows,

$$\mathbf{L}^e = \dot{\mathbf{F}}^e \mathbf{F}^{e-1} \tag{2.4}$$

$$\mathbf{L}^p = \dot{\mathbf{F}}^p \mathbf{F}^{p-1} \tag{2.5}$$

Substituting Eq. 2.3, Eq. 2.4, and Eq. 2.5 in Eq. 2.2, the velocity gradient can be expressed as:

$$\mathbf{L} = \dot{\mathbf{F}}\mathbf{F}^{-1} = (\dot{\mathbf{F}}^e \mathbf{F}^p + \mathbf{F}^e \dot{\mathbf{F}}^p)(\mathbf{F}^{p-1}\mathbf{F}^{e-1}) = \mathbf{L}^e + \mathbf{F}^e \mathbf{L}^p \mathbf{L}^{e-1} \tag{2.6}$$

2.1.2 Field Equations

Balance of Linear Momentum Denote $\boldsymbol{\sigma}$ as the Cauchy stress in the deformed body, and $J = \det(\mathbf{F})$ as the Jacobian of the deformation gradient tensor. The first Piola-Kirchoff stress $\mathbf{S}$ can be related to the Cauchy stress $\boldsymbol{\sigma}$ through the relation:

$$\mathbf{S} = (\det \mathbf{F})\boldsymbol{\sigma}\mathbf{F}^{-\mathrm{T}} = J\boldsymbol{\sigma}\mathbf{F}^{-\mathrm{T}} \tag{2.7}$$

The balance of linear momentum in the reference configuration is guaranteed by,

$$\mathrm{Div}\ \mathbf{S} + \mathbf{b} = \rho_0 \ddot{\boldsymbol{\varphi}} \tag{2.8}$$

where Div is the divergence with respect to the material point in the reference configuration.

by neglecting dynamic effects and body forces, the equilibrium equation reduces to the following form,

$$\mathrm{Div}\ \mathbf{S} = \mathbf{0} \tag{2.9}$$

Balance of Angular Momentum The balance of angular momentum guaranteed by,

$$\mathbf{S}\mathbf{F}^{\mathrm{T}} = \mathbf{F}\mathbf{S}^{\mathrm{T}} \tag{2.10}$$

This indicates that the Cauchy stress tensor $\boldsymbol{\sigma}$ is symmetric.

Balance of Energy In the reference configuration, denote P as a region in the reference body with the outward unit normal $\mathbf{n}_R$ on its boundary ∂R. Denote dV_R and dA_R as the volume and area integral. Furthermore, define ϵ as the internal energy per unit reference volume, $\mathbf{q}_R$ as the referential heat flux, and g as the heat generation rate per unit reference volume. The first law of thermodynamics in the reference configuration yields,

$$\int_{\partial R} \mathbf{S}\mathbf{n}_R \cdot \dot{\boldsymbol{\varphi}} dA_R - \int_{\partial R} \mathbf{q}_R \cdot \mathbf{n}_R dA_R + \int_R (\mathbf{b} \cdot \dot{\boldsymbol{\varphi}} + g) dV_R = \frac{d}{dt} \int_R (\epsilon + \frac{1}{2}\rho_0 \dot{\boldsymbol{\varphi}} \cdot \dot{\boldsymbol{\varphi}}) dV_R \quad (2.11)$$

By applying the divergence theorem to 2.11, we have,

$$\int_R (\mathrm{Div}\mathbf{S} \cdot \dot{\boldsymbol{\varphi}} + \mathbf{S} \cdot \nabla \dot{\boldsymbol{\varphi}}) dV_R - \int_R \mathrm{Div}\mathbf{q}_R dV_R + \int_R (\mathbf{b} \cdot \dot{\boldsymbol{\varphi}} + g) dV_R = \frac{d}{dt} \int_R (\epsilon + \frac{1}{2}\rho_0 \dot{\boldsymbol{\varphi}} \cdot \dot{\boldsymbol{\varphi}}) dV_R \quad (2.12)$$

Recall the linear momentum balance (Eq. 2.8) and multiply both sides by $\dot{\boldsymbol{\varphi}}$,

$$\mathrm{Div}\mathbf{S} \cdot \dot{\boldsymbol{\varphi}} + \mathbf{b} \cdot \dot{\boldsymbol{\varphi}} = \rho_0 \ddot{\boldsymbol{\varphi}} \cdot \dot{\boldsymbol{\varphi}} = \frac{d}{dt}(\frac{1}{2}\rho_0 \dot{\boldsymbol{\varphi}} \cdot \dot{\boldsymbol{\varphi}}) \quad (2.13)$$

Substituting Eq. 2.13 into Eq. 2.12 leads to,

$$\int_R (\mathbf{S} \cdot \nabla \dot{\boldsymbol{\varphi}} - \mathrm{Div}\mathbf{q}_R + g - \dot{\epsilon}) dV_R = 0 \quad (2.14)$$

Localizing the energy balance equation for every part in P yields,

$$\mathbf{S} \cdot \dot{\mathbf{F}} - \mathrm{Div}\mathbf{q}_R + g = \dot{\epsilon} \quad (2.15)$$

Entropy Imbalance In the reference configuration, define η as the entropy per unit reference volume. The entropy imbalance yields,

$$\frac{d}{dt} \int_R \eta dV_R \geqslant \int_{\partial R} -\frac{\mathbf{q}_R}{\theta} \cdot \mathbf{n}_0 dA_R + \int_R \frac{g}{\theta} dV_R \quad (2.16)$$

The Cauchy-Green elastic strain measure is defined as,

$$\mathbf{E}^e = \frac{1}{2}(\mathbf{F}^{e\mathrm{T}}\mathbf{F}^e - \mathbf{1}) \tag{2.17}$$

We then introduce a Helmholtz free energy as follows,

$$\psi = \hat{\psi}(\mathbf{E}^e, \theta, \xi) = \epsilon - \eta\theta \tag{2.18}$$

where θ is the absolute temperature and ξ is the volume fraction of martensite, a measure of the degree of phase transformation.

By applying the divergence theorem and combining Eq. 2.17,2.6, 2.12, 2.16, the entropy imbalance yields,

$$\{\mathbf{T}^e - \frac{\partial\psi}{\partial\mathbf{E}^e}\} \cdot \dot{\mathbf{E}}^e - \{\frac{\partial\psi}{\partial\theta} + \eta\}\dot{\theta} + (\mathbf{C}^e\mathbf{T}^e) \cdot \mathbf{L}^p - \frac{\partial\psi}{\partial\xi}\dot{\xi} - \frac{\mathbf{q}_0}{\theta} \cdot \nabla\theta \geqslant 0 \tag{2.19}$$

where a new stress measure, the elastic second Piola-Kirchoff stress is introduced: $\mathbf{T}^e = J\mathbf{F}^{e-1}\boldsymbol{\sigma}\mathbf{F}^{e-T}$.

Free Energy Following the work in [166, 124], the free energy per unit reference volume ψ is decomposed into three terms: the strain energy ψ^e, the energy of phase transformation ψ^p, and the thermal energy ψ^θ:

$$\psi(\mathbf{E}^e, \theta, \xi) = \psi^e(\mathbf{E}^e, \theta, \xi) + \psi^p(\xi, \theta) + \psi^\theta(\theta) \tag{2.20}$$

where ξ is the martensite volume fraction, and θ is the temperature.

The strain energy is given by:

$$\psi^e(\mathbf{E}^e, \theta, \xi) = \frac{1}{2}\mathbf{E}^e \cdot \mathcal{C}(\xi)\mathbf{E}^e \tag{2.21}$$

where $\mathcal{C}$ is the fourth-order elasticity tensor. Note that in this study we neglected the thermal expansion term.

The energy of phase transformation is given by,

$$\psi^p(\xi,\theta) = \frac{\lambda_T}{\theta_T}(\theta-\theta_T)\xi + \frac{1}{2}\sum_{i,j} g^{ij}\xi^i\xi^j \tag{2.22}$$

where $\theta_T \equiv \frac{1}{2}(\theta_{ms}+\theta_{as})$ is the phase equilibrium temperature, λ_T is the latent heat of phase transformation at θ_T, and g^{ij} is the interaction matrix that accounts for possible energetic interactions between transformation systems. Here we shall neglect the interactions between systems and consider $g^{ij}=0$ in our application of the theory to zirconia due to the lack of experimental data that would allows us to calibrate the interaction coefficients.

The thermal energy is given by,

$$\psi^\theta(\theta) = c(\theta-\theta_0) - c\theta\ln\frac{\theta}{\theta_0} \tag{2.23}$$

where c is the constant specific heat, and θ_0 is the reference temperature.

Combining the above equations, the entropy imbalance can be rewritten in the following form,

$$\big\{\mathbf{T}^e - \frac{\partial\psi^e}{\partial\mathbf{E}^e}\big\}\cdot\dot{\mathbf{E}}^e - (\frac{\partial\psi}{\partial\theta}+\eta)\dot{\theta} + (\mathbf{C}^e\mathbf{T}^e)\cdot\mathbf{L}^p - \frac{\mathbf{q}_0}{\theta}\cdot\nabla\theta \geqslant 0 \tag{2.24}$$

2.1.3 Constitutive Relations

Constitutive Equation for Elastic Stress The second Piola-Kirchhoff elastic stress tensor $\mathbf{T}^e$ can be expressed as,

$$\mathbf{T}^e = \frac{\partial\psi^e}{\partial\mathbf{E}^e} = \mathcal{C}\mathbf{E}^e \tag{2.25}$$

The elastic moduli $\mathcal{C}$ are obtained in terms of the respective values for the austenite and martensite phases $\mathcal{C}^a_{ijkl}$ and $\mathcal{C}^m_{ijkl}$, as a function of the martensite volume fraction ξ using the rule of mixtures,

$$\mathcal{C}_{ijkl} = \xi\mathcal{C}^m_{ijkl} + (1-\xi)\mathcal{C}^a_{ijkl} \tag{2.26}$$

As can be seen, $\mathbf{T}^e$ is work-conjugate to the elastic strain $\mathbf{E}^e$. $\mathbf{T}^e$ is related to the first Piola-Kirchhoff stress $\mathbf{S}$ and Cauchy stress $\boldsymbol{\sigma}$ through the following relations,

$$\mathbf{S} = \mathbf{F}^e \mathbf{T}^e \mathbf{F}^{p^{-\mathrm{T}}} \tag{2.27}$$

$$\boldsymbol{\sigma} = J^{-1} \mathbf{F}^e \mathbf{T}^e \mathbf{F}^{e^{\mathrm{T}}} \tag{2.28}$$

Phase Transformation Flow Rule As discussed in the previous section, the flow rule of phase transformation in SMAs is assumed to take a similar form to that in the crystal plasticity theory [1],

$$\begin{aligned} \dot{\mathbf{F}}^p &= \mathbf{L}^p \mathbf{F}^p, \\ \mathbf{L}^p &= \sum_{i=1}^{N} \dot{\xi}^i \mathbf{b}_0^i \otimes \mathbf{m}_0^i \end{aligned} \tag{2.29}$$

where N is the total number of transformation systems taken into consideration, ξ^i, $\dot{\xi}^i$ are the volume fraction of martensite and its rate of change in transformation system i, respectively. The volume fraction in each transformation system ξ^i and the total volume fraction $\sum_{i=i}^{N} \xi^i = \xi$ are constrained by:

$$0 \leqslant \xi^i \leqslant 1 \tag{2.30}$$

$$0 \leqslant \xi \leqslant 1 \tag{2.31}$$

A transformation system S_0 is defined by a set of $\{\mathbf{b}_0, \mathbf{m}_0\}$ which contains sufficient information on the orientation of a compatible austenite-martensite interface [120, 122].

$$\mathcal{S}_0^i = \mathbf{b}_0^i \otimes \mathbf{m}_0^i \tag{2.32}$$

As mentioned in Chapter 1, given the lattice parameters and symmetry of the austenite and martensite phases, one can apply the nonlinear theory of martensite

[1] Note that this is transformation flow rule proposed in [111] specifically for metallic shape memory materials. We will later extend the formulation to shape memory ceramics where non-Schmid effects have been observed during transformation

to obtain the transformation systems in the single crystals of interest. The calculation requires the knowledge of the mapping from the austenite configuration to the martensite one, which can be obtained by constructing the deformation gradient that takes a unit cell in the austenite phase to martensite. From there one then obtains the stretch tensor $\mathbf{U}_0$, as well as all possible variants of martensite by applying rotations to the $\mathbf{U}_0$. Then one can obtain the transformation systems by solving the twinning and habit plane equations, see Appendix B for a detailed description of the procedure. The algorithm is summarized as follows:

1. Construct Bain strains $\mathbf{U}_0$ (a mapping from the austenite point group $\mathcal{P}_a$ to the martensite point group $\mathcal{P}_m$) for the tetragonal to monoclinic transformation in zirconia;

2. Calculate all the possible variants of martensite $\mathbf{U}_i = \mathbf{Q}_i \mathbf{U}_0 \mathbf{Q}_i^T$, $\mathbf{Q}_i \in \mathcal{P}_a$;

3. Solve the twinning equation to obtain the twinning system for all possible combinations of i, j: $\mathbf{a}$ and $\hat{\mathbf{n}}$: $\mathbf{R}\mathbf{U}_j - \mathbf{U}_i = \mathbf{a} \otimes \hat{\mathbf{n}}$;

4. Solve the habit plane equation to obtain the transformation system $\mathbf{b}$ and $\hat{\mathbf{m}}$ for all possible combinations of i, j: $\mathbf{Q}(\mathbf{U}_i + (1-\mu)\mathbf{a} \otimes \hat{\mathbf{n}}) = \mathbf{I} + \mathbf{b} \otimes \hat{\mathbf{m}}$.

Previous work has been focused on identifying transformation systems in SMAs such as NiTi and Cu-based systems [167, 168, 128, 126, 17, 109]. The martensitic transformation in a NiTi single-crystal can appear in as many as 192 transformation systems, yet only a subset of 24 transformation systems are observed in experiments [128, 109]. In [111], the authors computed the components of theses 24 transformation systems with respect to an orthonormal basis associated with the cubic austenite lattice in a NiTi, and showed that the stress-strain response of a single-crystal NiTi predicted using 24 systems are qualitatively similar to that using the complete set of 192 systems [111]. Similar calculations were also later carried out for CuZnAl SMAs where the phase transformation is between the cubic austenite phase to a monoclinic martensite phase [16, 17], and 24 transformation system were identified for CuZnAl systems, as shown in Table 2.1. Simha [5] first used the nonlinear

i	$[\mathbf{m^i}]_1$	$[\mathbf{m^i}]_2$	$[\mathbf{m^i}]_3$	$[\mathbf{b}]_1$	$[\mathbf{b^i}]_2$	$[\mathbf{b^i}]_3$
1	0.1817	0.669	0.721	0.1634	-0.7435	0.6487
2	-0.1817	-0.721	-0.669	-0.1634	-0.6487	0.7435
3	0.1817	-0.669	-0.721	0.1634	0.7435	-0.6487
4	-0.1817	0.721	0.669	-0.1634	-0.6487	0.7435
5	-0.669	0.1817	0.721	0.7435	0.1634	0.6487
6	0.721	-0.1817	-0.669	0.6487	-0.1634	0.7435
7	0.669	0.1817	-0.721	-0.7435	0.1634	-0.6487
8	-0.721	-0.1817	0.669	-0.6487	-0.1634	0.7435
9	-0.1817	0.669	-0.721	-0.1634	-0.7435	-0.6487
10	0.1817	-0.721	0.669	0.1634	-0.6487	-0.7435
11	-0.1817	-0.669	0.721	-0.1634	0.7435	0.6487
12	0.1817	0.721	-0.669	0.1634	0.6487	0.7435
13	0.721	0.1817	0.669	0.6487	0.1634	-0.7435
14	-0.669	-0.1817	-0.721	0.7435	-0.1634	-0.6487
15	-0.721	0.1817	-0.669	-0.6487	0.1634	0.7435
16	0.669	-0.1817	0.721	-0.743	-0.1634	0.6487
17	0.669	-0.721	-0.1817	-0.743	-0.6487	-0.1634
18	-0.721	0.669	0.1817	-0.6487	-0.7435	0.1634
19	-0.669	0.721	-0.1817	0.7435	0.6487	-0.1634
20	-0.721	-0.669	0.1817	0.6487	0.7435	0.1634
21	-0.721	-0.669	-0.1817	-0.6487	0.7435	-0.1634
22	0.669	0.721	0.1817	-0.7435	0.6487	0.1634
23	0.721	0.669	-0.1817	0.6487	-0.7435	-0.1634
24	-0.669	-0.721	0.1817	0.7435	-0.6487	0.1634

Table 2.1: Variants of the transformation systems for CuZnAl [16, 17]

i	$[\mathbf{m^i}]_1$	$[\mathbf{m^i}]_2$	$[\mathbf{m^i}]_3$	$[\mathbf{b}]_1$	$[\mathbf{b^i}]_2$	$[\mathbf{b^i}]_3$
1	0.8230	-0.2522	-0.5090	0.0265	-0.0081	0.0169
2	-0.8230	0.2522	-0.5090	-0.0265	0.0081	0.0169
3	0.8230	0.2522	-0.5090	0.0265	0.0081	0.0169
4	-0.8230	-0.2522	-0.5090	-0.0265	-0.0081	0.0169
5	0.7856	-0.3519	-0.5090	0.0253	-0.0113	0.0169
6	-0.7856	0.3519	-0.5090	-0.0253	0.0113	0.0169
7	0.6987	0.5027	-0.5090	0.0225	0.0162	0.0169
8	-0.6987	-0.5027	-0.5090	-0.0225	-0.0162	0.0169
9	0.5027	-0.6987	-0.5090	0.0162	-0.0225	0.0169
10	-0.5027	0.6987	-0.5090	-0.0162	0.0225	0.0169
11	-0.3519	-0.7856	-0.5090	-0.0113	-0.0253	0.0169
12	0.3519	0.7856	-0.5090	0.0113	0.0253	0.0169
13	0.7856	0.3519	-0.5090	0.0253	0.0113	0.0169
14	-0.7856	-0.3519	-0.5090	-0.0253	-0.0113	0.0169
15	0.6987	-0.5027	-0.5090	0.0225	-0.0162	0.0169
16	-0.6987	0.5027	-0.5090	-0.0225	0.0162	0.0169
17	0.7856	0.3519	-0.5090	0.0162	0.0225	0.0169
18	-0.7856	-0.3519	-0.5090	-0.0162	-0.0225	0.0169
19	0.6987	-0.5027	-0.5090	-0.0113	0.0253	0.0169
20	-0.6987	0.5027	-0.5090	0.0113	-0.0253	0.0169
21	0.2522	0.8230	-0.5090	0.0081	0.0265	0.0169
22	-0.2522	-0.8230	-0.5090	-0.0081	-0.0265	0.0169
23	-0.2522	0.8230	-0.5090	-0.0081	0.0265	0.0169
24	0.2522	-0.8230	-0.5090	0.0081	-0.0265	0.0169

Table 2.2: Habit plane normal and transformation directions of the 24 transformation systems. The monoclinic and tetragonal lattice parameters are $a_m = 0.51597, b_m = 0.52222, c_m = 0.53227, \beta = 98.71,\ a_t = 0.5149; c_t = 0.5267$

theory of martensite to compute the transformation systems in zirconia-based SMCs where the phases are respectively tetragonal and monoclinic for a particular set of lattice parameters, see also [7] for a review of martensitic transformation systems in other ceramics. Here, we computed the transformation systems for the specific composition of CuZnAl and the ceria-doped zirconia used in the experiments from [6]. The results are shown in Table 2.2 and 2.1.

Transformation Conditions Similarly to the crystal plasticity theory [123], a resolved shear stress for phase transformation in each transformation system is defined

as follows,

$$\tau^i = \mathbf{b}_0^i \cdot (\mathbf{C}^e \mathbf{T}^e) \mathbf{m}_0^i \tag{2.33}$$

A thermodynamic force b (back stress) that is work-conjugate to the martensite volume fraction ξ is defined as,

$$b = \frac{\partial \psi^p}{\partial \xi} = \frac{\lambda_T}{\theta_T}(\theta - \theta_T) \tag{2.34}$$

For simplicity, we assume b remains the same for all transformation systems. Neglecting the interaction effects of different systems, the driving force f^i for phase transformation is defined as,

$$f^i = \tau^i - b \tag{2.35}$$

Forward and reverse transformation can only occur when the driving force f^i in the transformation system reaches a critical value Y^i. The transformation criteria are as follows [111],

$$f^i(\dot{\xi}) = \begin{cases} Y_+^i & \text{for} \quad \dot{\xi}^i > 0, \\ -Y_-^i & \text{for} \quad \dot{\xi}^i < 0. \end{cases} \tag{2.36}$$

where Y_+^i and Y_-^i are material parameters defined as the critical transformation resistance for forward and reverse transformation, respectively.

The consistency condition for phase transformation in each system can be obtained in a similar manner [109] to that in the plasticity theory [123],

$$\overline{(\tau^i - b - Y_+^i)}\dot{\xi}^i = 0 \quad \text{or} \quad \overline{(\tau^i - b + Y_-^i)}\dot{\xi}^i = 0 \tag{2.37}$$

Rate-dependent Theory The rate-independent formulation requires an implicit algorithm to determine the active transformation systems and associated martensite volume fractions. This is usually fraught with numerical difficulties which stem from the lack of convexity of the problem. A rate-dependent transformation condition [111], facilitates the use of an explicit algorithm, which enables robust calculations [169, 170]. Such a rate-dependent flow rule will reduce to the rate-independent

one (Eq. 2.37) in the limit where the rate-dependence exponent approaches zero. Closely following the derivation in [111], the main steps in the formulation are summarized below,

$$\tau^i - b = \begin{cases} +|\frac{\dot{\xi}^i}{\bar{\xi}^i}|^m Y^i_+ & \text{for} \quad \dot{\xi}^i \geqslant 0, \\ -|\frac{\dot{\xi}^i}{\bar{\xi}^i}|^m Y^i_- & \text{for} \quad \dot{\xi}^i \leqslant 0, \end{cases} \tag{2.38}$$

where the reference transformation rate $\bar{\xi}^i$, and the rate-dependence constant m, are additional material parameters for the rate-dependent model.

The transformation condition in the rate-dependent theory can be obtained by inverting Eq. 2.38,

$$\dot{\xi}^i = \begin{cases} +\bar{\xi}^i|\frac{\tau^i - b}{Y^i_+}|^{1/m} & \text{for} \quad \tau^i - b \geqslant 0, \\ -\bar{\xi}^i|\frac{\tau^i - b}{Y^i_-}|^{1/m} & \text{for} \quad \tau^i - b \leqslant 0, \end{cases} \tag{2.39}$$

Eq. 2.39 shows that the rate of change in martensite volume fraction in each transformation system $\dot{\xi}^i$ can be obtained in a straightforward manner in the rate-dependent theory. The volume fraction of martensite ξ^i is updated at each time step upon solving for $\dot{\xi}^i$. Closely following the framework in [111, 109], we assume the critical transformation stress remains the same for all transformation systems, $Y^i_+ = Y^i_- = Y$ for simplicity and lacking better experimental evidence.

2.1.4 Phase Transformation Flow Rule and Non-Schmid effect

The framework developed in the previous section is derived from the framework of crystal-plasticity where slip is approximated as homogeneous shear deformation of a lattice. However, unlike in metallic shape memory alloys where martensitic transformation is volume preserving, martensitic transformation in zirconia is accompanied by a significant volume change (about 4-5%) and the formation of martensite involves a normal deformation in addition to the pure shear component. Consequently, stresses normal to the habit plane also contribute to the driving force for martensitic

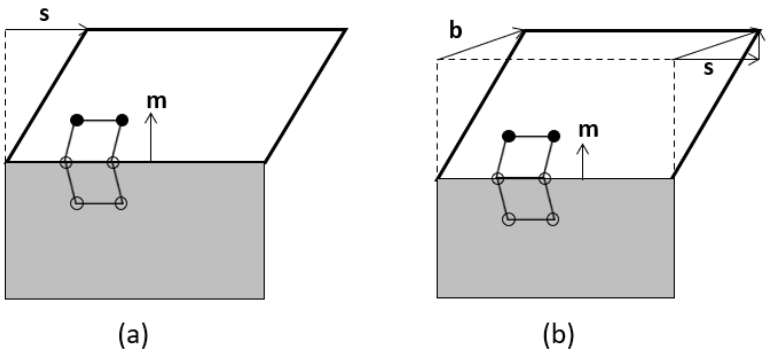

Figure 2-1: Approximation of slip, twinning (a), and martensitic phase transformations (b) as homogeneous deformations. Reproduced from [12]

transformation in addition to shear stresses. From a micromechanics perspective, this is explained by the fact that transformation systems in zirconia are non-orthogonal which introduces a non-Schmid effect in the transformation response. As a result, the formulation derived from crystal-plasticity that obeys the Schmid law is not sufficient anymore. To this end, we adapted the formulation in [12] to include the normal deformation in addition to the pure shear component during transformation,

As seen in Figure 2-1, the deformation associated with martensite transformation and the inelastic deformation gradient can be expressed as:

$$\mathbf{x} = \mathbf{X} + \xi(\mathbf{b}_0 \otimes \mathbf{m}_0)\mathbf{X} \tag{2.40}$$

$$\mathbf{F} = \nabla\mathbf{x} = \mathbf{I} + \xi(\mathbf{b}_0 \otimes \mathbf{m}_0) \tag{2.41}$$

The direction of phase transformation $\mathbf{b}_0$ is decomposed as,

$$\xi\mathbf{b}_0 = \xi_s\mathbf{s}_0 + \xi_n\mathbf{m}_0 \tag{2.42}$$

where $\mathbf{s}_0$ and $\mathbf{m}_0$ are the shear and normal directions, respectively, and $\xi_n = \xi\mathbf{b}_0 \cdot \mathbf{m}_0$.

Upon including the normal deformation across the habit plane, the transformation

velocity gradient in a single transformation system setting then yields,

$$\mathbf{L}^p = \dot{\mathbf{F}}\mathbf{F}^{-1} = \frac{\dot{\xi}}{1+\xi_n}\mathbf{b}_0 \otimes \mathbf{m}_0 \tag{2.43}$$

In a multi-system setting, the transformation velocity gradient becomes[2],

$$\mathbf{L}^p = \sum_{i=1}^{N} \frac{\dot{\xi}^i}{1+\xi_n^i}\mathbf{b}_0^i \otimes \mathbf{m}_0^i \tag{2.44}$$

Note that this is a general formulation for shape memory materials that takes into consideration possible volume change accompanied by martensitic transformation. Recall that in conventional crystal plasticity-like models with multiple transformation systems, the velocity gradient $\mathbf{L}^p$ is given by

$$\mathbf{L}^p = \sum_{i=1}^{N} \dot{\xi}^i \mathbf{b}^i \otimes \mathbf{m}^i \tag{2.45}$$

. For metallic shape memory materials where there is no volume change during the transformation, the term $1+\xi_n^i$ is 1 and Equation 2.44 reduces to $\mathbf{L}^p = \sum_{i=1}^{N} \dot{\xi}^i \mathbf{b}_0^i \otimes \mathbf{m}_0^i$.

In summary, the rate-dependent flow rule of the phase transformation reads,

$$\begin{aligned} \dot{\mathbf{F}}^p &= \mathbf{L}^p\mathbf{F}^p \\ \mathbf{L}^p &= \sum_{i=1}^{N} \frac{\dot{\xi}^i}{1+\xi_n^i}\mathbf{b}_0^i \otimes \mathbf{m}_0^i \\ \dot{\xi}^i &= \bar{\xi}|\frac{\tau^i - b^i}{Y}|^{1/m}\mathrm{sgn}(\tau^i - b^i) \end{aligned} \tag{2.46}$$

[2]The sufficient condition that guarantees that the form for the inelastic deformation gradient is independent of the sequence of activation is thoroughly discussed in [171]

2.2 Summary of Governing and Constitutive Equations

The linear momentum balance:

$$\text{Div}\mathbf{S} + \mathbf{b} = \rho_0 \ddot{\boldsymbol{\varphi}} \tag{2.47}$$

The elastic stress-strain relation:

$$\mathbf{T}^e = \mathcal{C}[\mathbf{E}^e - \mathbf{A}(\theta - \theta_0)] \tag{2.48}$$

The transformation back stress:

$$b = \frac{\partial \psi^p}{\partial \xi} = \frac{\lambda_T}{\theta_T}(\theta - \theta_T) \tag{2.49}$$

The resolved shear stress for each transformation system:

$$\tau^i = \mathbf{b}_0^i \cdot (\mathbf{C}^e \mathbf{T}^e)\mathbf{m}_0^i \tag{2.50}$$

The rate-dependent phase transformation flow rule:

$$\begin{aligned} \dot{\mathbf{F}}^p &= \mathbf{L}^p \mathbf{F}^p \\ \mathbf{L}^p &= \sum_{i=1}^{N} \frac{\dot{\xi}^\alpha}{1 + \xi_n^i} \mathbf{b}^\alpha \otimes \mathbf{m}^i \\ \dot{\xi}^i &= \bar{\xi} |\frac{\tau^i - b}{Y}|^{1/m} \quad \text{sgn}(\tau^i - b), \end{aligned} \tag{2.51}$$

It bears emphasis that the use of the constitutive model in calculations requires the specification of the constitutive model parameters: anisotropic elastic moduli in both phases $\mathcal{C}^a_{ijkl}, \mathcal{C}^m_{ijkl}$, the transformation stress Y, the back stress b, and the orientation of each crystal relative to the frame of the simulations in which the loading directions are specified. In our implementation of the model, we use the rotation matrix to define the crystal orientation with respect to the global reference frame. This rotation matrix is

used to effect the necessary tensorial transformations to the global coordinate system in which the loading is applied. The rotation matrix can also be obtained from the Euler angles determined experimentally.

2.3 Explicit Constitutive Update Algorithm for Martensite Phase Transformation

An explicit algorithm that solves for the volume fraction of martensite in each transformation system in a sequential manner is implemented for updating the constitutive equations [169, 170]. Each transformation system is handled iteratively in such a calculation. The determination of forward or reverse transformation is distinguished by the sign of the overstress, where positive values indicate forward transformation (to monoclinic martensite) and negative ones a reverse transformation (to tetragonal austenite). At each time step, the transformation system with largest absolute overstress $|\tau^i - b|$ is identified and the corresponding volume fraction is updated based on Equation 2.39. The computation proceeds with the other systems in decreasing order of absolute overstress until there is no inactive system with admissible overstress (i.e. for the forward transformation the resolved shear stress exceeds the back stress, and for the reverse transformation the resolved shear stress is smaller than the back stress). The detailed algorithm is as follows,

1. Calculate the volume fraction ξ^i for all systems based on the step t_n;
2. Compute $\mathbf{F}^e = \mathbf{F}_{n+1}\mathbf{F}_n^{p^{-1}}$ and evaluate τ^i for all systems;
3. Calculate the overstress $\tau^i - b$ for all systems and determine its largest absolute value. If this overstress is negative: if $\tau^i - b > 0$ for all systems, go to step 6; If this overstress is positive: if $\tau^i - b < 0$ for all systems, go to step 6. Otherwise:
4. Evaluate $\Delta\mathbf{F}^p = \frac{\dot{\xi}_n^i}{1+\xi_n^i} dt(\mathbf{b}_0^i \otimes \mathbf{m}_0^i)$ based on the system i with the largest absolute value of overstress;
5. Premultiply $\mathbf{F}^p$ by $\Delta\mathbf{F}^p$, return to step 2 using the updated $\mathbf{F}^p$;

6. Compute new volume fraction rates $\dot{\xi}^i$ for each transformation system.

Chapter 3

Simulation Studies of Elastic and Phase Transformation Incompatibilities at oSMA Grain Boundaries

Recent experimental studies have shown that premature intergranular fracture which severely affects the superelastic properties of polycrystalline Cu-based SMAs can be mitigated in fine wires with bamboo-shape oligocrystalline microstructure [2, 52]. In this case, the energy absorption properties and reversible transformation strains can approach the limits of a single crystal. However, the presence of occasional grain boundaries and triple junctions along the length of the wire can still originate incompatibility of deformation due to either elastic or transformation anisotropy, which induces stress concentrations and leads to premature intergranular fracture.

In this chapter, we investigated the competition between transformation and grain boundary constraints as sources of potential premature intergranular fracture in the deformation response of bi-crystal oSMAs using the micromechanical single-crystal constitutive model of phase transformation described in Chapter 2 and finite element simulations. The anisotropic model is able to account for the key mechanisms of

elastic deformation and transformation anisotropy in the single crystal level, and for the constraints to deformation that arise at the grain boundary.

We conducted a series of finite element simulations of the tensile response in bi-crystal CuZnAl oSMA wires of arbitrary grain misorientations. The simulation results facilitates a better understanding of the competing mechanisms of elastic and transformation incompatibility leading to intergranular fracture. Specifically, they suggest that if the grain misorientation is such that the elastic anisotropy is high, sizable stress concentrations at grain boundaries can be observed. This would likely induce fracture in the oligocrystal structure at very a small strain level. By contrast, bi-crystals can achieve full transformation strength comparable to single crystals in the case where elastic incompatibility is low. In addition, the results contain detailed information on nucleation and evolution of martensite variants and stress concentration at SMA grain boundaries. They also provided a clear picture of the deformed shapes of individual grain which helps to understand the type of deformation incompatibility arising at grain boundary. We also showed that this approach could be used to explore the misorientation space for quantifying the level of stress concentration and strain incompatibilities arising at grain boundaries. The simulation results allowed for the identification of general grain misorientations that reduce or minimize elastic and transformation incompatibility, as well as provided insights on the microstructural design of Cu-based SMAs to avoid fracture along grain boundaries. We then investigated the correlation between different types of incompatibilities and two specific metrics charactering the geometrical configuration of grain boundaries, the disorientation angle and CSL.

3.1 Modeling Approach

To model the stress-strain response and martensitic transformation of bi-crystal CuZnAl oSMA wires under tensile loading, we conducted finite element simulations utilizing a computational mesh of 17762 tetrahedral first-order elements representing a section in an oligocrystal oSMA wire. Figure 3-1 illustrates the geometry of a bi-

crystal oSMA wire. Unit cells in each grain demonstrate different orientations of the top and bottom grain, and the interface represents the bi-crystal grain boundary. The length of the wire is 6 mm and the diameter 1 mm. Although the model lacks the description of length scale, we selected the aspect ratio 6:1 to mimic the experimentally observed geometrical configuration of oSMA wires. The mesh consists of two volumes representing two grains oriented perpendicular to the $x - y$ plane in a cylindrical oligocrystalline sample, and grain boundary is perpendicular to z axis. Each grain is assigned a different orientation, which in the model is defined by a rotation matrix and can be calculated from Euler angles. The interface in the middle represents the grain boundary in the bi-crystalline structure. Considering the lack of data specific to grain boundary response to allow a quantitative evaluation, we adopted the well-established grain boundary conformity assumption [172, 173] to analyze incompatibilities due to crystal anisotropy and grain boundary misorientations. This assumption is also supported by scanning electron micrograph (SEM) images showing that grain boundaries remain conformal during experiments. A more detailed model of the grain boundary would require a characterization of deformation mechanism which is not readily available. With one grain's orientation fixed (Euler angles $E1 = 194°$, $E2 = 46°$, $E3 = 235°$), we conducted 26 finite element simulations of oSMA wires with general grain misorientations undergoing tensile loading. The orientations of the samples can be found in Table 3.1. We analyzed the simulation results to explore how grain misorientation affects the development of stress concentration due to elastic and/or transformation incompatibilities. We ran finite element simulations up to 12% strain which exceeds the transformation strain for single-crystals and analyzed the evolution of the von Mises equivalent stress at the grain boundary and martensite volume fraction in each transformation system as the deformation progresses. The von Mises stress is chosen as a metric for quantifying the magnitude of the complex deviatoric stress state, which is responsible for premature fracture. In addition, we explored the correlation between grain boundary characteristics (CSL and disorientation angles) and different types of incompatibilities arising at grain boundaries. Based on the results of the analysis, we proposed an interpre-

tation on the role of elastic and transformation strain incompatibility as a cause for stress concentration and potential premature fracture in oSMA wires.

simulation	rotation matrix
1	$\begin{bmatrix} -0.2528 & -0.8491 & -0.4639 \\ 0.6853 & -0.4956 & 0.5337 \\ -0.6830 & -0.1830 & 0.70711 \end{bmatrix}$
2	$\begin{bmatrix} -0.9492 & 0.0605 & 0.3088 \\ 0.3103 & 0.0170 & 0.9505; \\ 0.0523 & 0.9980 & -0.0349] \end{bmatrix}$
3	$\begin{bmatrix} 0.4189 & 0.6909 & -0.5892 \\ -0.8912 & 0.1884 & -0.4126 \\ -0.1740 & 0.6980 & 0.6947 \end{bmatrix}$
4	$\begin{bmatrix} -0.0341 & 0.9689 & -0.2451 \\ -0.8501 & -0.1571 & -0.5026 \\ -0.5255 & 0.1913 & 0.829 \end{bmatrix}$
5	$\begin{bmatrix} -0.7071 & 0.7071 & 0 \\ 0.2763 & 0.2763 & 0.9205 \\ 0.6509 & 0.6509 & -0.390 \end{bmatrix}$
6	$\begin{bmatrix} 0.5774 & 0.5774 & 0.5774 \\ -0.7887 & 0.2113 & 0.5774 \\ 0.2113 & -0.7887 & 0.5774 \end{bmatrix}$
7	$\begin{bmatrix} 0.9659 & 0.2588 & 0 \\ -0.2315 & 0.8640 & 0.4472 \\ 0.1157 & -0.4320 & 0.8944 \end{bmatrix}$
8	$\begin{bmatrix} 0.7555 & 0.6363 & 0.1562 \\ -0.6489 & 0.6938 & 0.3123 \\ 0.0904 & -0.3373 & 0.9370 \end{bmatrix}$

9	$\begin{bmatrix} 0.5175 & 0.8008 & 0.3015 \\ -0.8486 & 0.4348 & 0.3015 \\ 0.1104 & -0.4119 & 0.9045 \end{bmatrix}$
10	$\begin{bmatrix} 0.5336 & 0.7407 & 0.4082 \\ -0.8324 & 0.3747 & 0.4082 \\ 0.1494 & -0.5577 & 0.8165 \end{bmatrix}$
11	$\begin{bmatrix} 0.9097 & 0.3533 & 0.2182 \\ -0.3439 & 0.3462 & 0.8729 \\ 0.2329 & -0.8691 & 0.4364 \end{bmatrix}$
12	$\begin{bmatrix} 0.8600 & 0.4558 & 0.2294 \\ -0.4744 & 0.5488 & 0.6882 \\ 0.1878 & -0.7008 & 0.6882 \end{bmatrix}$
13	$\begin{bmatrix} 0.7868 & 0.5195 & 0.3333 \\ -0.5863 & 0.4602 & 0.6667 \\ 0.1929 & -0.7200 & 0.6667 \end{bmatrix}$
14	$\begin{bmatrix} 0.5435 & 0.7038 & 0.4575 \\ -0.8226 & 0.3378 & 0.4575 \\ 0.1675 & -0.6250 & 0.7625 \end{bmatrix}$
15	$\begin{bmatrix} 0.5499 & 0.6800 & 0.4851 \\ -0.8162 & 0.3140 & 0.4851 \\ 0.1775 & -0.6626 & 0.7276 \end{bmatrix}$
16	$\begin{bmatrix} 0.7629 & 0.6086 & 0.2182 \\ -0.6340 & 0.6384 & 0.4364 \\ 0.1263 & -0.4713 & 0.8729 \end{bmatrix}$
17	$\begin{bmatrix} 0.9659 & 0.2588 & 0 \\ -0.2511 & 0.9371 & 0.2425 \\ 0.0628 & -0.2343 & 0.9701 \end{bmatrix}$

18	0.7711	0.5778	0.2673
	−0.6176	0.5770	0.5345
	0.1547	−0.5773	0.8018
19	0.8472	0.5037	0.1690
	−0.5130	0.6926	0.5071
	0.1383	−0.5163	0.8452
20	0.9659	0.2588	0
	−0.1436	0.5358	0.8321
	0.2154	−0.8037	0.5547
21	0.6873	0.6499	0.3244
	−0.7105	0.5083	0.4867
	0.1514	−0.5650	0.8111
22	0.9659	0.2588	0
	−0.2021	0.7543	0.6247
	0.1617	−0.6034	0.7809
23	0.7777	0.5535	0.2981
	−0.6045	0.5282	0.5963
	0.1725	−0.6440	0.7454
24	0.9659	0.2588	0
	−0.1948	0.7269	0.6585
	0.1704	−0.6361	0.7526
25	0.9288	0.3586	0.0937
	−0.3286	0.6799	0.6556
	0.1714	−0.6397	0.7493
26	0.8140	0.5135	0.2716
	−0.5528	0.5411	0.6338
	0.1785	−0.6660	0.7243

Table 3.1: Orientations of the samples used in the finite element simulations

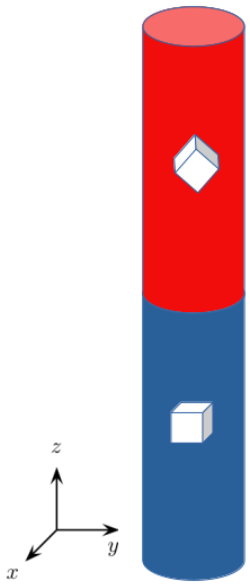

Figure 3-1: An example of the oSMA wire specimen

3.2 Examination of Elastic and Transformation Incompatibility in Bi-crystal oSMAs

In order to understand to the basic types of responses we obtained, we first discuss two particular cases in these simulations with distinct stress-strain responses, where one case shows distinct elastic incompatibility (Case 1: $E1 = 250°$, $E2 = 34°$, $E3 = 206°$ for the top grain) and the other (Case 2: $E1 = 187°$, $E2 = 57°$, $E3 = 234°$ for the top grain) shows low elastic incompatibility yet rather large incompatibility of transformation. The results corresponding to Case 1 are illustrated in Figure 3-2. Figures 3-2a and 3-2b respectively show the spatial distribution of the von Mises stress and the total martensite volume fraction on the surface of the bi-crystal wire at a macroscopic strain level $\epsilon = 0.5\%$. As depicted in Figure 3-2a, the von Mises stress exhibits a peak at the grain boundary of the order of 434 MPa which is a factor of 3 larger than in the bulk of the grain. As shown in Figure 3-2b, both grains remain ostensibly in the austenite phase at this level of applied strain, except at the grain boundary where incipient transformation can be observed. Since there is no significant transformation, it can be concluded that for this bi-crystal configuration,

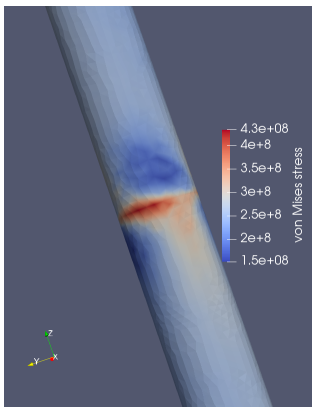

(a) von Mises stress at $\epsilon = 0.5\%$

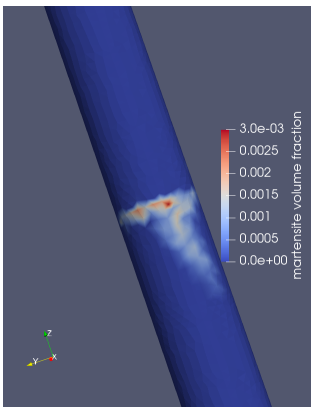

(b) Martensite volume fraction at $\epsilon = 0.5\%$

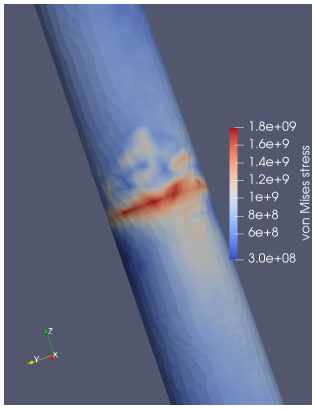

(c) von Mises stress at $\epsilon = 6\%$

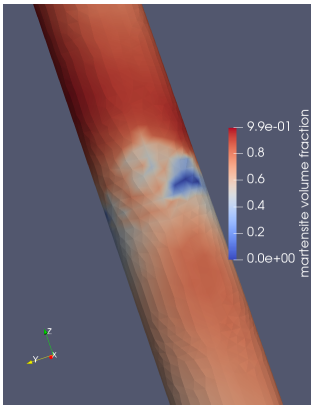

(d) Martensite volume fraction at $\epsilon = 6\%$

Figure 3-2: Case 1: spatial distribution of stresses and martensite volume fraction near grain boundary plane during elastic regime (a)(b), during transformation (c)(d)

deformation incompatibility and stress concentration near the grain boundary arise entirely due to elastic anisotropy.

Figures 3-2c and 3-2d demonstrate the corresponding results at the strain level $\epsilon = 6\%$, which is the final stage of transformation. Figure 3-2d shows that both grains have almost fully transformed except for regions near the grain boundary where transformation is still incomplete. It is worth emphasizing that although we ran the simulations beyond the completion of martensitic transformation, the oSMA wire is expected to break during the elastic range due to large stress concentration at this strain level. As clearly illustrated in Figure 3-2c, the von Mises stress at the grain boundary is about 3 times larger than in regions away from the grain boundary. This indicates that as the wire deforms and the transformation progresses, the increase in stress at the grain boundary is limited, since the stress concentration factor remains the same value as prior to transformation. The stress concentration factor does not increase noticeably during the transformation, which suggests that for this particular grain misorientation, there is no further contribution to stress concentration arising from the anisotropic transformation strains at the grain boundary. In addition, we extracted the evolution of the spatial distribution of martensite variants from the simulations, and qualitatively compared this information with experimental observations of martensite morphology captured in the SEM images in [52]. The experimental results highlight a significant non-uniformity in martensitic transformation in the oligocrystal structure. Specifically, grain boundaries trigger early onset of transformation yet restricts the complete transformation at larger strains. The morphology of martensite is highly localized, multi-variant near grain boundaries and fairly uniform in the unconstrained area. Figures 3-3(a)-(c) show respectively the spatial distribution of martensite volume fraction at strain level $\epsilon = 0.5\%$ in selected systems 5, 10 and 14 obtained from the simulations. It can be noticed that in all three systems, the martensitic transformation initiated at the grain boundary region. However, as shown in Figures 3-3(d)-(f), at strain level $\epsilon = 6\%$, the martensitic transformation near the grain boundary was largely stalled in system 5 and 14, while the region away from the grain boundary experienced a relatively larger amount of transformation.

Meanwhile in the bottom grain, system 10 just started to transform while the top grain remained in the austenite phase. It can be concluded that the simulation results are in consistency with the experiments.

As a way to understand the magnitude of the stress concentration caused by the presence of the grain boundary, we compared with the single crystal response performed on two single crystals with the same orientations as each individual grain in the bi-crystal. Figure 3-4 shows a comparison of the evolution of the von Mises stress in both single crystals and the maximum value in the bi-crystal grain boundary. A few observations can be made. The much larger initial slope in the bi-crystal compared to the single crystals is indicative of significant elastic incompatibility for this grain boundary configuration. These stresses relax very rapidly away from the grain boundary in the unconstrained regions in the bi-crystal toward the values of the stress fields in the individual single crystals. These observations are consistent with the elastic simulation results in [52]. It is expected that for this type of grain boundary configuration, fracture would ensue at the grain boundary due to elastic incompatibility at low levels of strain, thus preventing further transformation and significantly inhibiting the ability of the material to achieve large superelastic deformations.

The results corresponding to Case 2 are shown in Figure 3-5. Figure 3-5b shows that up to an applied strain $\epsilon = 0.5\%$, there is a negligible amount of transformation inside the grains, whereas the grain boundary remains in the austenite phase. At this strain level, the stress concentration at the grain boundary is much lower in this configuration compared to Case 1, see Figure 3-5a. This suggests that in this particular bi-crystal, grains are oriented such that elastic deformations in the austenite phase are more compatible. Figure 3-5c and 3-5d show the corresponding results at $\epsilon = 6\%$. We can observe that both crystals have almost fully transformed but the grain boundary still remains in the austenite phase. This suggests that this specific grain misorientation inhibits phase transformation at the grain boundary, i.e. it corresponds to a case of transformation strain incompatibility. Figure 3-6 shows the spatial distribution of martensite volume fraction in some transformation systems at different strain levels. When $\epsilon = 0.5\%$, as shown in Figures 3-6a-3-6c systems 5 and 14 are the dominant

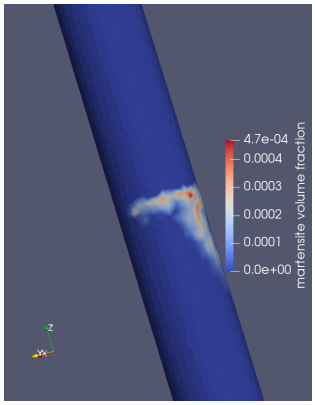

(a) system 5

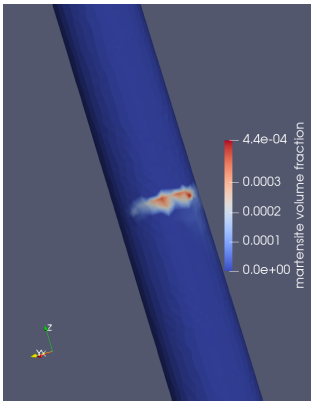

(b) system 10

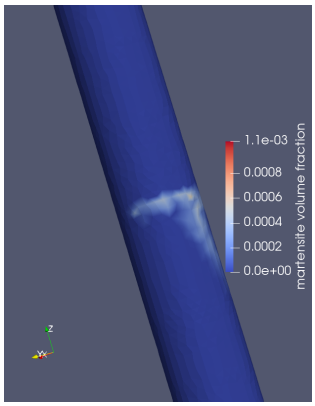

(c) system 14

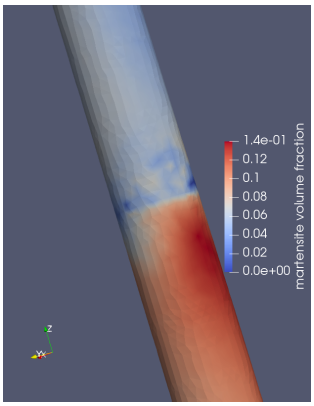

(d) system 5

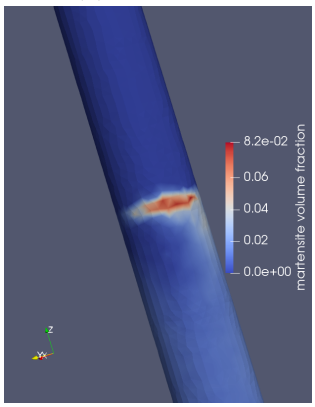

(e) system 10

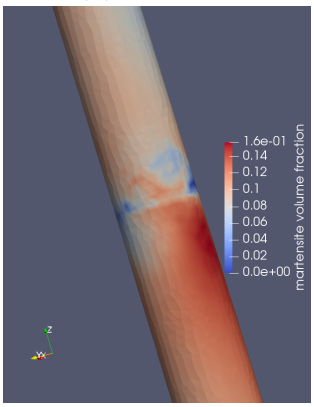

(f) system 14

Figure 3-3: Case 1: spatial distribution of martensite volume fraction near grain boundary plane in selected systems (a)(b)(c) $\epsilon = 0.5\%$, (c)(d)(e) $\epsilon = 6\%$

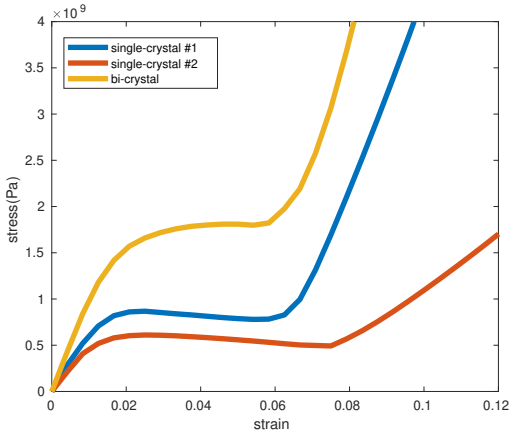

Figure 3-4: Evolution of maximum von Mises stress at the grain boundary plane in bi-crystal and single crystals

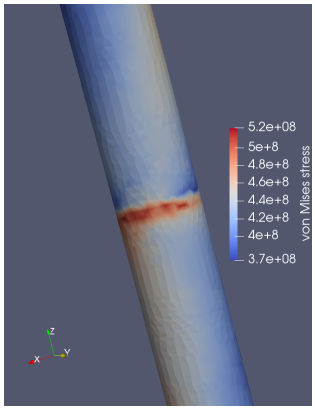

(a) von Mises stress at $\epsilon = 0.5\%$

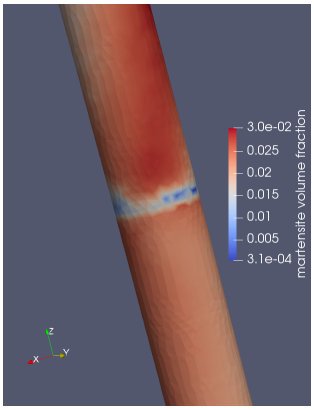

(b) Martensite volume fraction at $\epsilon = 0.5\%$

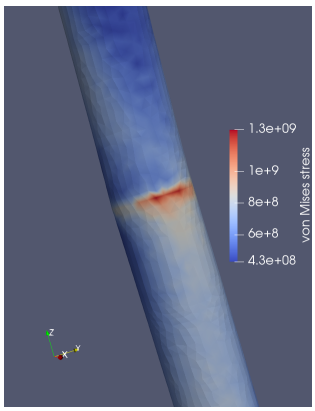

(c) von Mises stress at $\epsilon = 6\%$

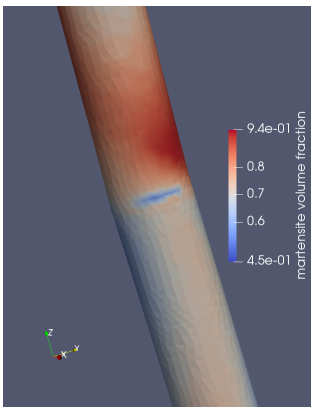

(d) Martensite volume fraction at $\epsilon = 6\%$

Figure 3-5: Case 2: spatial distribution of von Mises stress and martensite volume fraction near grain boundary plane during elastic regime (a)(b), during transformation (c)(d)

transformation systems with a significant larger amount of martensitic transformation than system 9, which remains untransformed except for the small area near its grain boundary where the transformation just initiated (martensitic volume fraction: 0.4%). As the applied strain increases to $\epsilon = 6\%$, we now can see the martensitic transformation in the top grain in systems 5 and 14, while system 9 is still resistant to transformation except for the grain boundary area (martensitic volume fraction: 1.2%), see Figures 3-6d to 3-6f. It is worth emphasizing that these simulation results once again demonstrate the multi-variant nature of martensitic transformation in oligocrystal grain boundaries compared to their single crystal counterparts. The localization of transformation is also accompanied by a concentration of stress at the grain boundary, as the contours of maximum von Mises stress in Figure 3-5c demonstrate, and stress concentration in this case is due to transformation incompatibility instead of elastic incompatibility.

Figure 3-7 shows plots of the evolution of the von Mises stress in the two single crystals and at the bi-crystal grain boundary for this case. It is very clear that there is a high level of elastic compatibility in the austenite phase, as the three initial slopes coincide. As transformation progresses, however, the maximum von Mises stress in the bi-crystal interface grows significantly compared to both single crystals, which confirms that the source of stress concentration is the incompatibility of transformation strains.

Based on these results, it is expected that for this type of grain boundary early fracture due to elastic incompatibility would be avoided. However, transformation strain incompatibility would control the level of strain achievable without fracture.

We can also make some important visual observations of deformation incompatibilities near bi-crystal grain boundaries. It is clear from Figure 3-6 that the deformation of the two adjacent grains in Case 2 is relatively more compatible than in Case 1 (see Figure 3-3), and von Mises stress at the grain boundary in Case 2 is significantly smaller than that in Case 1 towards the end of transformation.

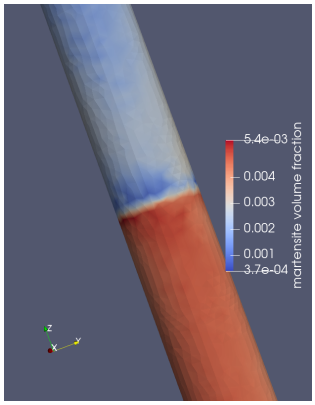

(a) system 5

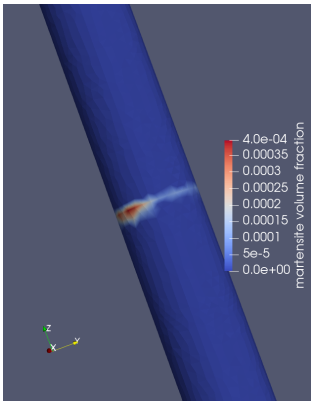

(b) system 9

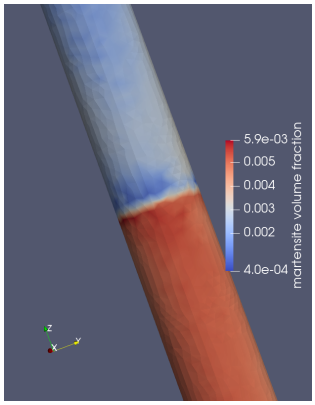

(c) system 14

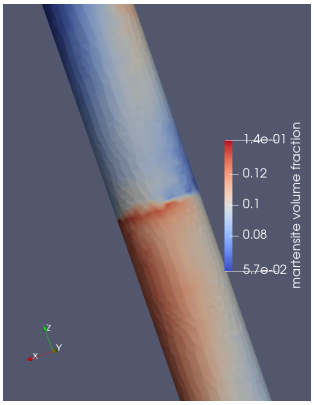

(d) system 5

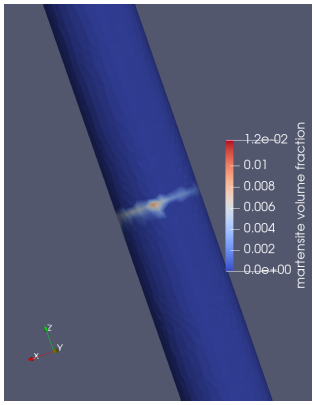

(e) system 9

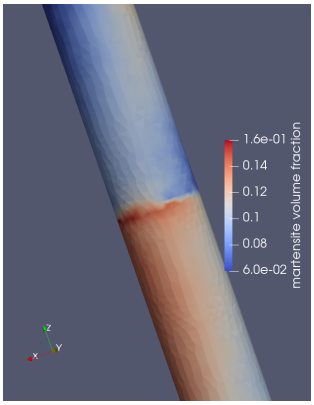

(f) system 14

Figure 3-6: Case 2: spatial distribution of martensite volume fraction near grain boundary plane in selected systems (a)(b)(c) $\epsilon = 0.5\%$, (c)(d)(e) $\epsilon = 6\%$

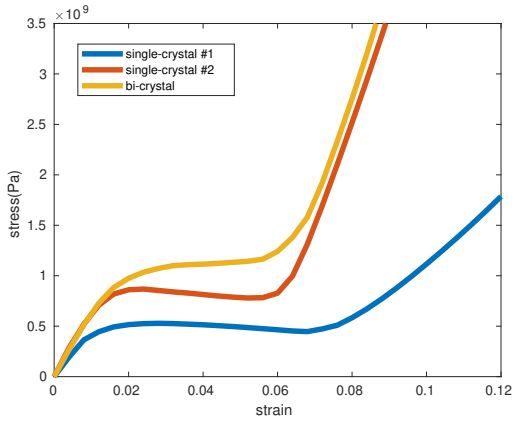

Figure 3-7: Case 2: Evolution of maximum von Mises stress at the grain boundary plane in bi-crystal and single crystals

3.2.1 Application of Coincident Site Lattice Theory of Bi-crystal SMAs

With this preliminary understanding of these two types of incompatibilities, we now discuss and analyze the finite element simulation results corresponding to the remaining 24 cases. We use two metrics to characterize the type of incompatibilities. One is the rate of growth (stiffness ratio) of maximum von Mises stress at grain boundary relative to that in the bottom grain, this is chosen as a measure of elastic incompatibility. The second metric is the ratio of maximum von Mises stress at grain boundary and in the bottom grain at strain level of $\epsilon = 3\%$ (normalized von Mises stress), this is the measure for the incompatibility of transformation strains. We chose to evaluate the normalized von Mises stress at 3% strain because a Cu-based SMA is normally undergoing forward transformation at said strain level. To investigate the dependence of bi-crystal behaviors on grain boundary characteristics, we performed the Coincident Site Lattices (CSL) analysis on all 26 bi-crystal samples following the work detailed in [174, 175]. CSL are special grain boundaries where the atomic lattices line up such that a fraction of the atoms of the two lattices will be in the same location. Grain boundaries that contain a high density of lattice points in a coincident site lattice is expected to have low energy and low diffusion rates and to be resistant to sliding due to good atomic fit. The fraction of the atoms that align is expressed as Σn, where n

is the inverse of the fraction of atoms that align or volume ratio). As the number of atoms that align become smaller, multiple CSLs with the same fraction but different rotation axes $\hat{\mathbf{r}}$ may occur; and these different configurations are distinguished by letters after the Σn value (e.g. $\Sigma 29a$) [63].

To demonstrate the effect of CSL on strain incompatibilities arising at the grain boundary, we identified five finite element simulations with CSL grain boundaries, as shown in Table 3.2. Figure 3-8 (a), (b), (c) and (d) shows the stress-strain responses of bi-crystals with $\Sigma 1$, $\Sigma 11$, $\Sigma 11$, and $\Sigma 29a$, respectively. Note that grain boundaries with extremely small disorientation angles θ_{min} are referred to as small angle CSLs, denoted by $\Sigma 1$. It can be observed that $\Sigma 1$, $\Sigma 11$ grain boundaries have demonstrated very small incompatibility in the elastic range, while large elastic incompatibility is shown in the $\Sigma 29a$ grain boundary configuration. Figure 3-9 (a)-(e) shows the corresponding results for non-CSL type grain boundaries. Evidently, these cases all demonstrated elastic incompatibilities at different levels, with Figure 3-9 (b) and (e) demonstrate the largest elastic incompatibility with stress concentration factor larger than 3. Creuziger et.at [63] conducted experiments and theoretical analysis and concluded that grain boundaries with low order coincident site lattices (CSLs) are less inclined to fail. However, our results showed that the level of transformation incompatibility has no significant relation with the CSL order, see Figure 3-8 (b). In summary, our analysis proved that CSL serves as a good indication of elastic incompatibility; that is, grain boundary configurations of CSL types exhibit low stiffness ratio. But large stress concentration may still occur when transformation incompatibility is high. Grain boundaries of high order CSL, however, are not necessarily compatible elastically.

In addition, Figure 3-10a shows the stiffness ratios in 26 bi-crystal specimens and their disorientation angles. Each point represents a bi-crystal with a disorientation angle defined as the minimum rotation angle with the misorientation axis located in the Standard Stereographic Triangle (SST). It can be observed that among these bi-crystals with various misorientations, the largest stiffness ratio is about 2.3, suggesting that in general elastic incompatibility in this type of Cu-based SMAs is quite high.

Case	θ_{min}	$\hat{\mathbf{r}}$	CSL Type
Low order CSL			
1	13.4	[-0.0662 0.4197 -0.1854]	Σ1-small angle
2	43.87	[1.0638 -0.8886 0.0061]	Σ9
3	45.11	[1.0111 -0.1977 -0.9727]	Σ11
4	55.12	[1.2893 1.0075 -0.1229]	Σ11
Higher order CSL			
5	43.6	[0.7169 0.9233 0.9297]	$\Sigma 29a$

Table 3.2: Among the 26 misorientations considered, only 5 are CSL grain boundaries.

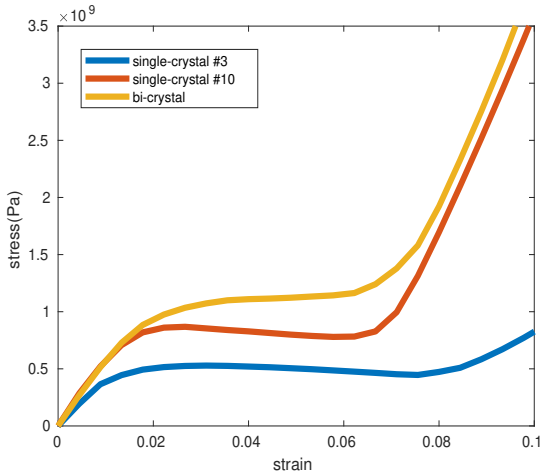

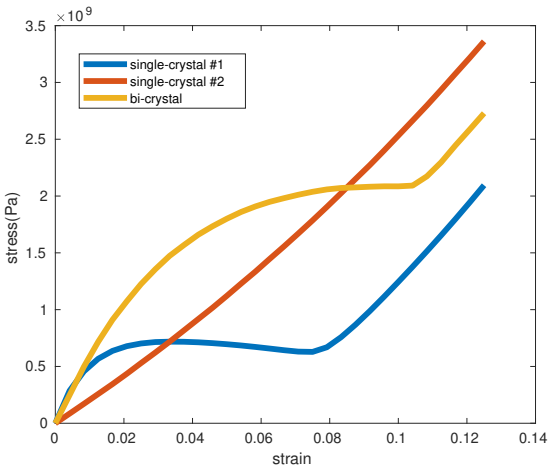

Σ1, Euler angles: [194, 46, 235], [187, 57, 234] Σ11, Euler angles: [135, 113, 0], [177, 92, 18]

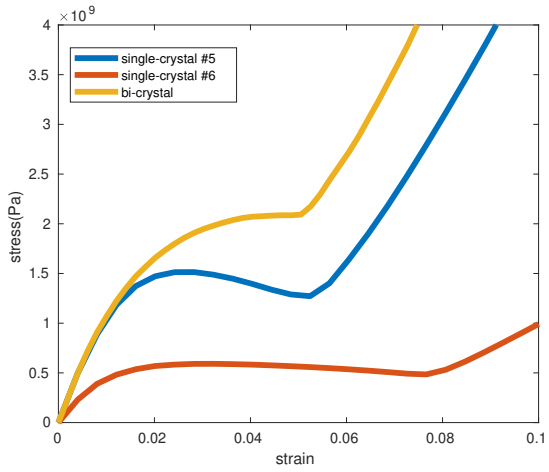

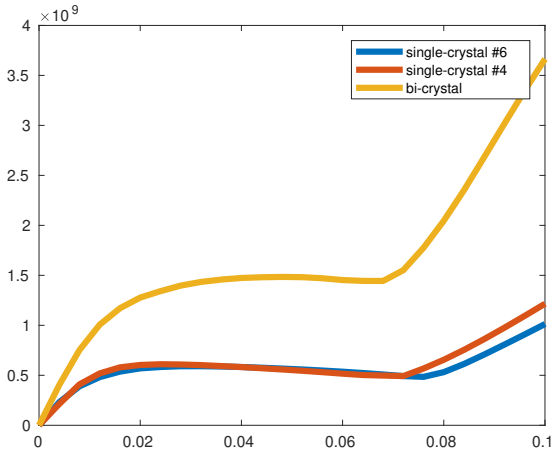

Σ11, Euler angles: [135, 113, 0], [84, 142, 118] $\Sigma 29a$, Euler angles: [250, 34, 206], [84, 142, 118]

Figure 3-8: Maximum von Mises stress at the CSL type grain boundary plane in bi-crystal and single crystals

One can also notice that there is no clear correlation between disorientation angles and elastic incompatibilities. Moreover, the specimens with lowest stiffness ratio are those with larger disorentation angles, which is quite counterintuitive. Most bi-crystal specimens with smaller disorientation angles(smaller than 40°) are shown to have quite large stiffness ratios. The largest stiffness ratios occur in specimens with disorientation angles between 40° and 50°. Figure 3-10b shows the respective results of maximum von Mises stress concentration factor at the grain boundary plane at 2.5% strain. Among all the bi-crystal specimens we analyzed, the largest von Mises stress concentration factor is slighter smaller 4 and it occurs in the bi-crystal with a disorientation angle about 52°. Similarly, we see no clear correlation between the disorientation angles and the von Mises stress concentration factor. However, it can be noticed that specimens with larger disorientation angles (40° to 50°) have the smallest stresses concentration factor from both the elastic and transformation anisotropy.

3.3 Conclusion

Three-dimensional finite element simulations using the micromechanical model enabled the investigation of the evolution of stress concentrations at the grain boundary due to either elastic or transformation strain incompatibility, as well as the analysis of the evolution of the martensite volume fraction. We conducted a series of finite element simulations of oSMA wires with general grain misorientations undergoing tensile loading. Among them two representative cases were identified: one of high elastic incompatibility (Case 1), and one of high elastic compatibility but significant transformation incompatibility (Case 2). The following conclusions were drawn from the simulations results and analysis.

1. The level of stress concentration at the grain boundary as measured by the maximum von Mises stress strongly depends on the crystal boundary misorientation.

2. Elastic incompatibility is quite large in this material. For grain configurations in

which there is significant incompatibility due to elastic anisotropy, large stress concentrations take place at oSMAs grain boundaries at very low strains levels with no significant transformation occuring in either crystal.

3. There exist grain configurations with low elastic incompatibilities, and large stress concentrations during the elastic range can potentially be avoided in these configurations. However, there still can be incompatibilities depending on the extent of transformation strain incompatibility, which will lead to stress concentrations and potential failure at various strain levels during phase transformation.

4. By means of CSL analysis, we also showed that grain boundaries of low order CSL types exhibit very little stress concentration at grain boundaries during elastic range, therefore can potential achieve larger transformation strain. While large stress concentration at low strains due to elastic anisotropy were observed in higher order CSL grain boundaries and random grain boundaries. The approach could be used in an exhaustive simulation study spanning the complete misorientation space. This would allow the identification of misorientations that reduce or minimize elastic and transformation incompatibility and, thus, extend the superelastic range of oSMAs.

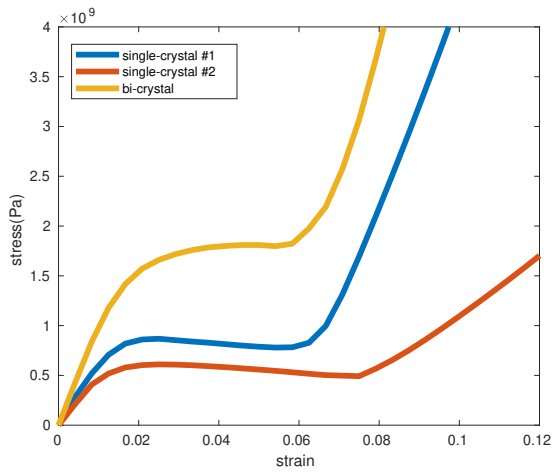

(a) Euler angles: [194, 46, 235], [250, 34, 206]

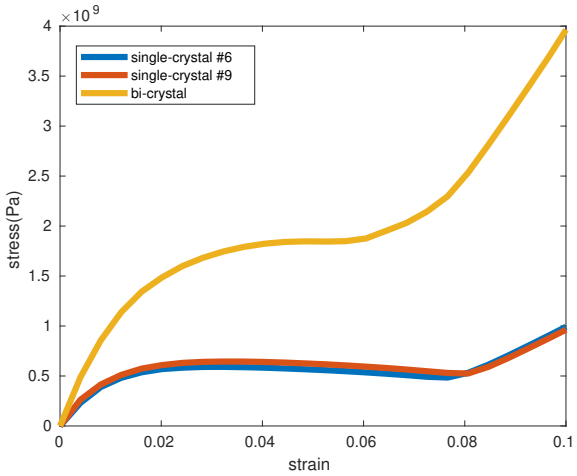

(b) Euler angles: [84, 142, 118], [262, 45, 179]

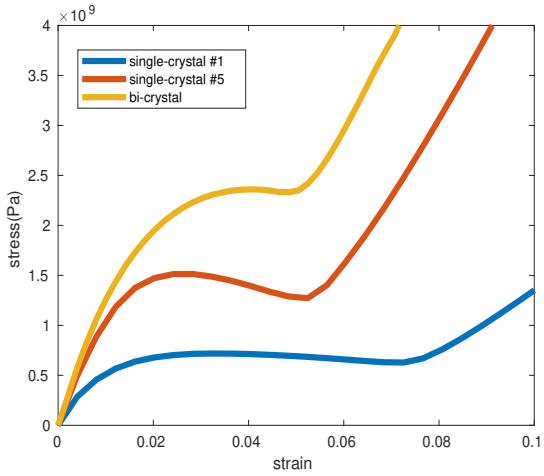

(c) Euler angles: [285, 45, 319], [135, 113, 0]

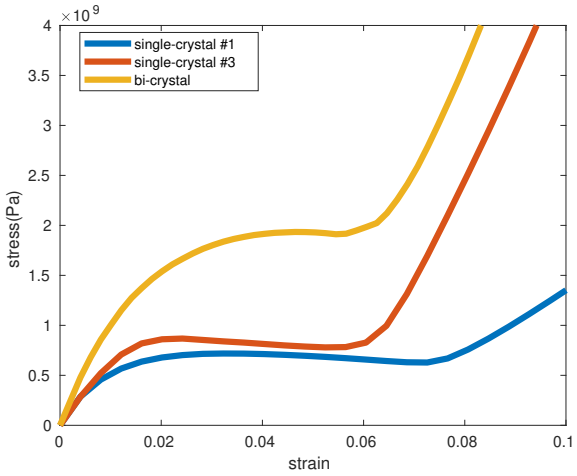

(d) Euler angles: [194, 46, 235],[285, 45, 319]

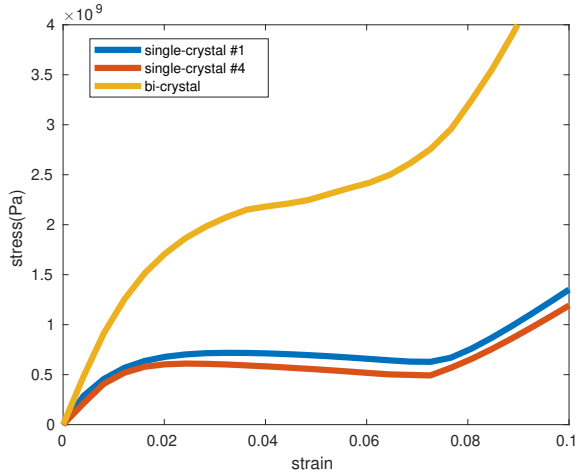

(e) Euler angles: [285, 45, 319], [250, 34, 206]

Figure 3-9: Maximum von Mises stress at the non-CSL type grain boundary plane in bi-crystal and single crystals

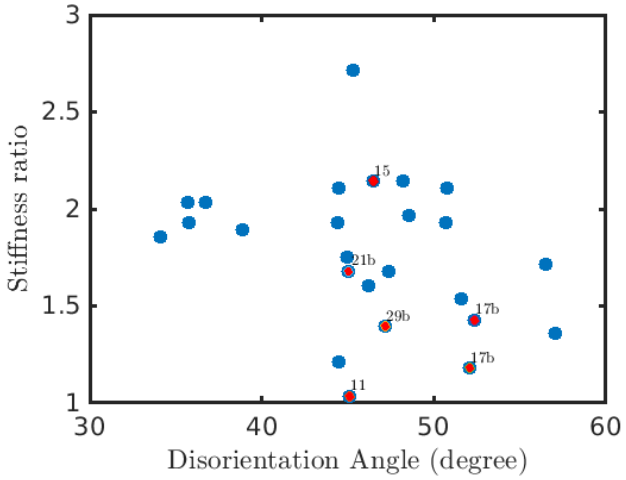

(a) Stiffness ratio (the ratio of initial slope at bi-crystal grain boundary and single crystal)

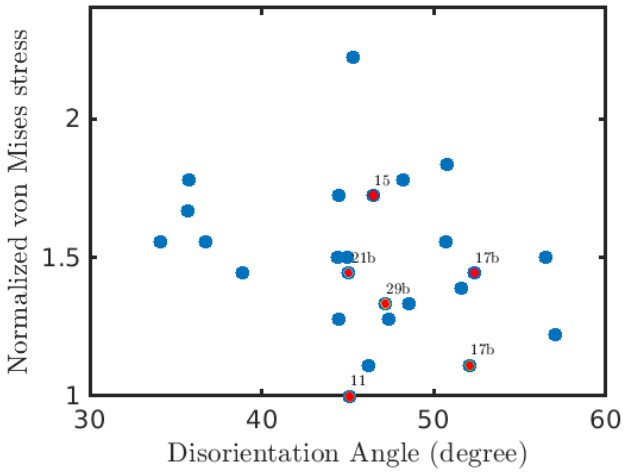

(b) Normalized maximum von Mises stress at 2.5% strain level

Figure 3-10: Plot of quantified elastic and transformation incompatibility at bi-crystal grain boundary vs. disorientation angles

Chapter 4

Phase Transformation and Incompatibility at Grain Boundaries in Zirconia-based SMCs

In this chapter, a single-crystal model is implemented to provide a full mechanistic three-dimensional description of the anisotropic elastic as well as martensitic transformation stress-strain response, including non-Schmid behavior caused by the significant volume change during martensitic transformation. This model was calibrated to and validated against compression tests of single-crystal zirconia micro-pillars conducted in previous literature, prior to being used to model bi-crystals. We conducted a series of simulations of bi-crystal SMCs sampled over the misorientation space, in search of grain boundary configurations that can achieve the full ductility potential of a single crystal. The simulation results provided detailed information on the nucleation and evolution of martensite variants and stress distribution at grain boundaries. To guide the discussion, we first identified bi-crystal configurations which result in very large stress concentrations at very low deformations due to elastic incompatibility, as well as others where the elastic incompatibility is relatively low and stress concentrations only occur at large transformation strains. We also analyzed the relationship between different types of incompatibilities and grain boundary characteristics, specifically disorientation angles. We also showed how this approach can

be used to explore the misorientation space for quantifying the level of elastic and transformation incompatibility at SMCs grain boundaries.

4.1 Model Calibration using Nano-pillar Compression Tests

The constitutive model described in Chapter 2 is calibrated against the micro-pillar compression tests in [6, 76], where grain orientations of single crystal micro-pillar samples were identified using electron backscatter diffraction and correlated with room temperature mechanical response. 24 transformation systems are identified from correspondence B (neither correspondence A or C produces any habit plane for this specific set of lattice parameters). These experiments provide the following data: the critical stress for room temperature transformation, the transformation strain that results, and an approximate value for the loading (tetragonal) elastic modulus. Zeng et al. [76] observed a wide variety of mechanical responses amongst differently-oriented samples, including martensitic transformation without cracking, plastic slip, and fracture. An important limitation of micro-pillar compression experiments is the significant difference between the measured and theoretical loading modulus [6]. In this particular reference, it was observed that for most of the samples with smaller transformation stresses, micro-compression experiments underestimated the elastic moduli significantly. The authors attributed the discrepancy to several aspects of the micro-compression experiments such as substrate and tip compliance, minor misalignments, possible defects in the micro-pillar samples and indentation compliance at the point of contact of the tip and pillar.

We conducted simulations of zirconia micro-pillars with various orientations undergoing compression. In the simulation, we assumed an idealized compression test and artificial compliance was not considered. We therefore expect to obtain a much stiffer elastic response than the experiments. A test of a micro-pillar (Euler angles $E1 = 53°$, $E2 = 122°$, $E3 = 299°$) that underwent full martensitic transformation

without cracking was taken as the basis for calibrating the model parameters. The constitutive model accepts as input the rotation matrix for describing the crystallographic orientation of the crystal. The three Euler angles are converted to the rotation matrices, and later are used to properly rotate all the relevant tensorial quantities. Elastic constants for both austenite and martensite phases were obtained from [176]. Figure 4-1a shows the results of the model using the theoretical values of the elastic constants, where the transformation stress $Y = 6$ MPa and backstress $b = 3$ MPa are calibrated to match the experimental results.

In this particular orientation, the elastic loading modulus in the experiment was about three times smaller than the theoretical value, as a result of the machine compliance issues described above. Accordingly, in Figure 4-1b we perform a post-facto linear machine compliance correction of the strain, to force a match with the theoretical modulus of the tetragonal phase at zero strain. Since the loading and unloading moduli are similar, we used the value obtained from the austenite phase for both loading and unloading cases for simplicity. Figure 4-1b shows that after adjusting the moduli to the theoretical value, the model captures the stress-strain response of the test using the calibrated parameters quite well. Simulations of pillar samples with different grain orientations were conducted and their stress-strain responses are shown in Figure 4-2. It can be observed that the model is also proven to capture the orientation dependence of the material mechanical response quite well.

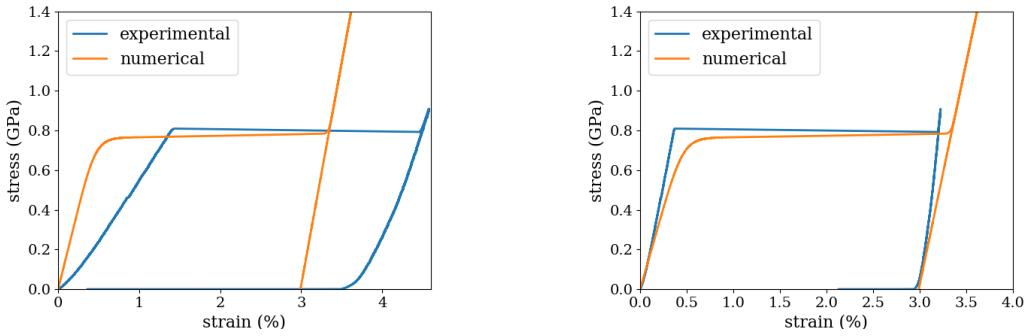

(a) Original experimental data

(b) Experimental data with the elastic modulus is adjusted to theoretical value

Figure 4-1: Simulation results compared with experiments, Euler angles = [53, 122, 299]

To verify the ability of the calibrated model to capture the orientation dependence of transformation stress in zirconia, we conducted simulations using the various orientations of the samples tested in [76] that underwent martensitic transformation without fracture. As a way of summarizing the results, we extracted from the simulation results the calculated transformation stresses for each orientation and compared them with the experimentally measured values in Figure 4-3. It can be observed that, except for a few outliers, the theoretical predictions are a reasonable match to the measured values, despite the unquantified uncertainties, including those in the measurements of grain orientation, possible defects in the micro-pillars, the control of boundary conditions and shape of the micro-pillars.

4.2 Competition Between Phase Transformation and Incompatibility at Grain Boundaries in Bi-crystals

To improve our understanding of incompatibilities arising from elastic anisotropy as well as incompatibility of transformations at grain interfaces, high-resolution three-dimensional finite element simulations of bi-crystal zirconia specimens subjected to compressive loading were conducted. We considered a simple scenario in which two cubic grains were stacked along the z axis. The grain boundary plane was oriented parallel to the $x-y$ plane and the loading direction is along $z-$ axis. Figure 4-4 illustrates the geometry of the bi-crystal specimen. Unit cells in each grain demonstrate different orientations of the top and bottom grain.

We first sampled misorientation space to explore different types of grain boundary incompatibilities. We selected orientations from the experiments in [76] that exhibited martensitic transformation under compression, and avoided orientations that slipped or fractured in the single crystal tests. We started by fixing the orientation of the bottom grain (E1=3°, E2=146°, E3=306°) and considered two different orientations for the top grain which resulted in distinct strain incompatibility types. Each grain is described with its crystallographic orientation by effecting the necessary tensorial

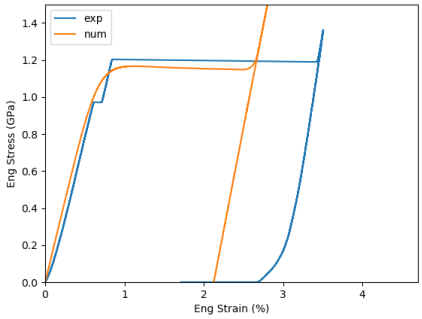

(a) Euler angles = $[3, 146, 306]$

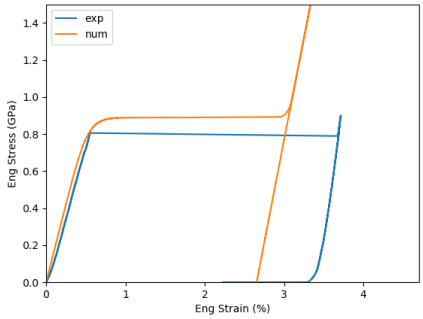

(b) Euler angles = $[194, 46, 235]$

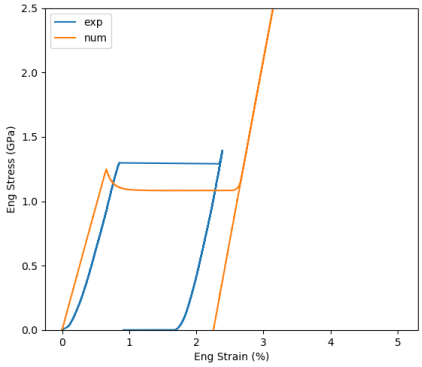

(c) Euler angles = $[75, 117, 301]$

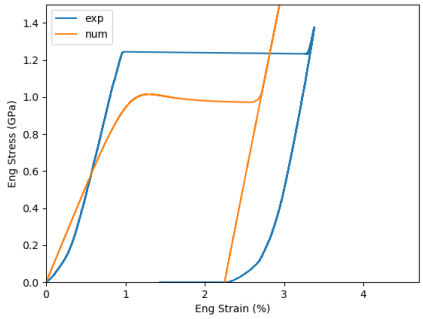

(d) Euler angles = $[250, 34, 206]$

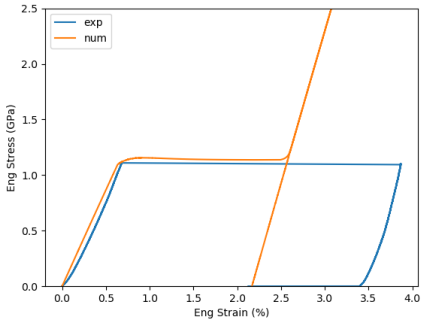

(e) Euler angles = $[258, 60, 147]$

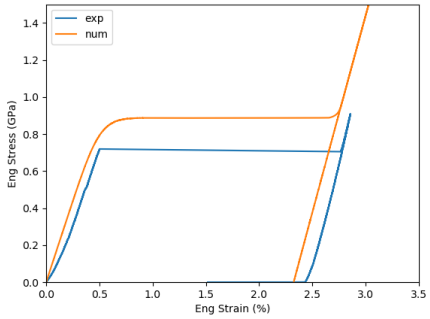

(f) Euler angles = $[245, 33, 197]$

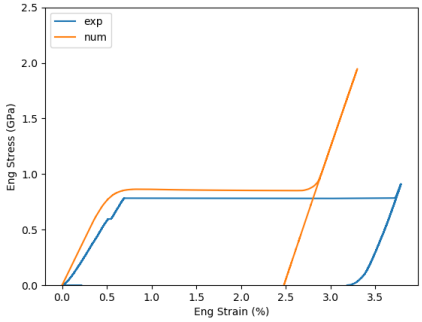

(g) Euler angles = $[187, 57, 234]$

Figure 4-2: Simulation results compared with experimental data after the elastic modulus is adjusted to theoretical value 89

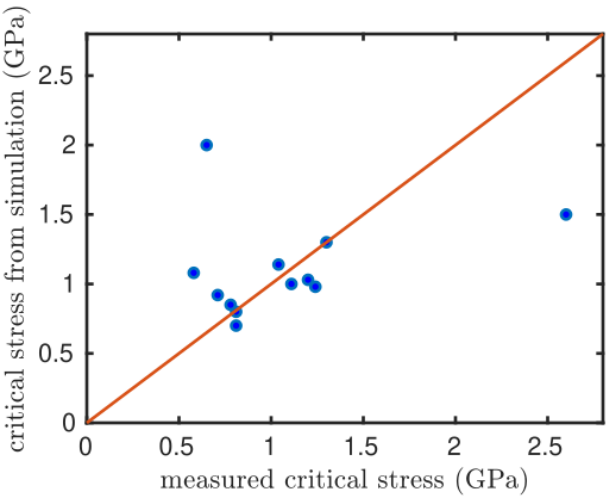

Figure 4-3: Orientation dependence of critical transformation stress: simulation results compared with experiments

transformations to the global coordinate system in which the loading is applied.

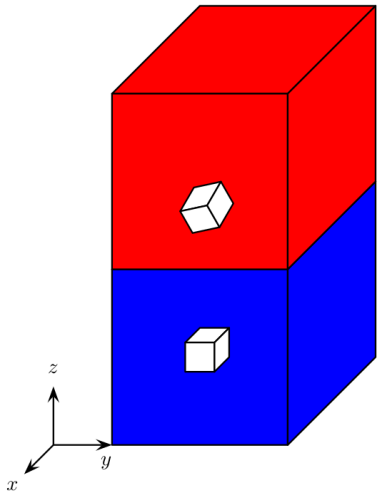

Figure 4-4: An example of the bi-crystal specimen

We ran simulations up to 5% strain which exceeds the transformation strain for the single-crystal orientations tested here, and monitored the evolution of the von Mises equivalent stress at the grain boundary as the deformation progresses. The von Mises stress provides a metric for quantifying the magnitude of the complex deviatoric stress state at the grain boundary. We also monitored the volume fraction of martensite in each transformation system and overall to understand the onset and progression of the transformation at the grain boundary versus the bulk of the grain. To understand

the influence of grain boundaries on the stress field, we conducted corresponding simulations on single crystals with the same orientations as each individual grain in the bi-crystal.

We considered two different cases which, as we shall see, result in two distinct types of incompatibility. In Case 1, the top grain orientation is given by Euler angles E1=53°, E2=122°, E3=299°, whereas in Case 2, the Euler angles for the top grain are E1=84°, E2=142°, E3=118°. The results of the two simulations are shown in Figures 4-5 and 4-7.

Figure 4-5(a), (b) and (c) respectively show snapshots of the von Mises stress at different cross-sections, and the total martensite volume fraction at the bi-crystal grain boundary obtained in Case 1 at a small strain level of 0.6%, at which point the deformation is still ostensibly elastic with martensite volume fraction on the order of 10^{-2}. As can be observed, there is a significant amount of stress concentration at the grain boundary plane in the bi-crystal, despite there being almost no transformation. The maximum von Mises stress can be seen near grain boundary (≈ 0.96 GPa). Figure 4-5(c)-(e) show the total volume fraction as well as the volume fraction in selected transformation systems (3 and 19). Though the overall martensitic volume fraction is extremely small, it is still worth mentioning that the main contribution of martensitic transformation came from system 19, which in this case is the most favorably oriented for transformation, i.e., where the resolved shear stress is the largest. In contrast, system 3 is an example of a system where transformation has not yet been triggered and the volume fraction is 3 orders of magnitude smaller than that in system 19. Figure 4-6(a) shows the comparison of the von Mises stress in the single crystals and the maximum value in the bi-crystal grain boundary as a function of strain for Case 1. As may be noted, the von Mises stress at the grain boundary plane grows significantly larger than that in either single crystal before the occurrence of phase transformation. These results suggest that the source of strain incompatibility is elastic anisotropy.

Figures 4-7 and 4-8 shows the corresponding results for Case 2. Figures 4-7(a), (b) and (c) show the von Mises stress at different bi-crystal cross-sections and corresponding martensitic volume fraction when $\epsilon = 0.3\%$. At this strain level, the

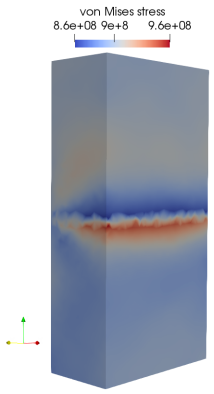

(a) von Mises stress at a bi-crystal cross section plane parallel to $x - z$ plane when $\epsilon = 0.6\%$

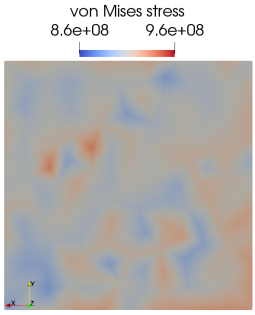

(b) von Mises stress at a bi-crystal cross section plane parallel to $x - y$ plane when $\epsilon = 0.6\%$

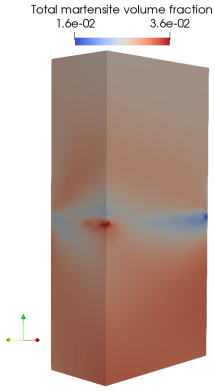

(c) Corresponding total martensite volume fraction

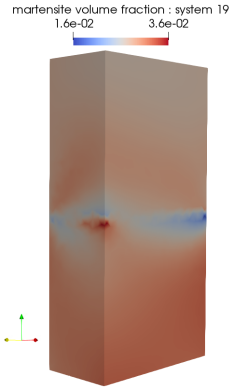

(d) Corresponding martensite volume fraction in system 19

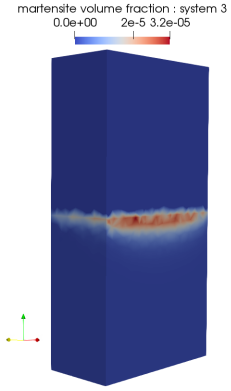

(e) Corresponding martensite volume fraction in system 3

Figure 4-5: Contours of: (a) von Mises; (c)-(e) martensite volume fraction; in the bi-crystal cross-section with normal y; (b) von Mises in the bi-crystal cross-section with normal z. The figures illustrate that there is a strong stress concentration near the bi-crystal interface at a low strain level. Figures (b)-(d) show at that level, there is an incipient but very low transformation. Martensitic transformation is primarily triggered in system 19, but the overall amount of martensite volume fraction is still very small.

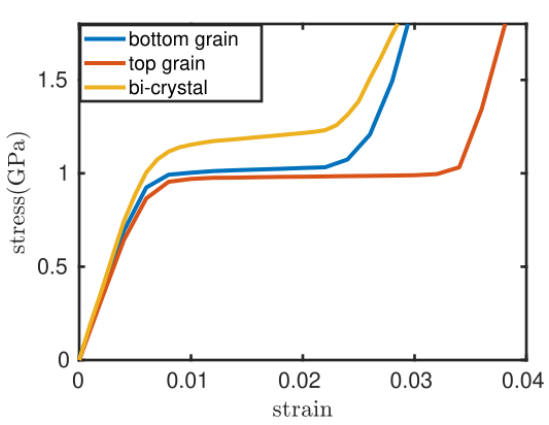

(a) Maximum von Mises stress at the grain boundary plane in bi-crystal and single crystals

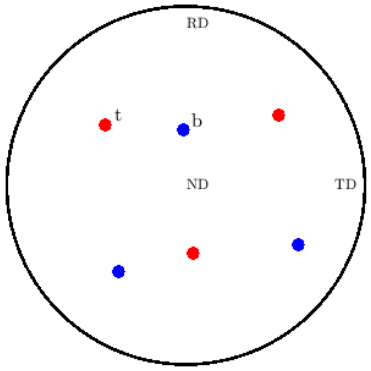

(b) Pole figure showing the [001] [010] [110] poles of the top (red, with the long axis labeled as 't') and bottom grain (blue, with the long axis labeled as 'b')

Figure 4-6: Case 1: Grain boundary configuration with high elastic incompatibility

stress concentration at the grain boundary plane is extremely low and there is no transformation (total volume fraction is on the order of 10^{-4}). This grain boundary configuration therefore has insignificant elastic incompatibility. Figure 4-7(d)-(j) show the corresponding results at $\epsilon = 2\%$, as well as martensite volume fraction in several transformation systems. There is a significant stress concentration at the grain boundary plane at this strain level, as the maximum von Mises stress at the grain boundary is about 1.3 GPa, which is about 1.44 times larger than that in the regions that are farther from grain boundary. As shown in Figure 4-7(e), the corresponding martensitic volume fracture in the bottom grain at this strain level is about 1 except for the region near grain boundary, which indicates that the bottom grain has fully transformed to martensitic phase except for the region near grain boundary. The top grain has also seen a significant amount of transformation with the volume fraction ranging from 0.38 to 0.6, which suggests that stress concentrations are due to the incompatibility of the anisotropic transformation strain at the grain boundary instead of elastic anisotropy at this level of deformation. It is also worth mentioning that martensitic volume fraction in system 19 is $3-4$ orders of magnitude larger than that in other systems, which makes it the dominant transformation system as it

contributes the most to the total volume fraction. As shown in Figure 4-8(a), there is a very low level of elastic incompatibility in the austenite phase, as the three initial slopes coincide. As a result, the maximum von Mises stress at the grain boundary plane remains similar to that in the single crystal. However, as transformation progresses, the maximum von Mises stress at the bi-crystal interface grows much larger than inside either single crystal. At strain level $\epsilon = 2\%$, the stress concentration factor at the grain boundary is about 1.6. The maximum von Mises stress at the grain boundary grows from 1 GPa to 1.3 GPa during transformation, while von Mises stresses in the two single crystal cases plateau at 0.7 GPa and 1 GPa, respectively. This suggests that the source of stress concentration is the incompatibility of the transformation strains. Specifically, at the grain interface, the transformation strain in one grain cannot be accommodated by that in the neighboring grain due to the anisotropic nature of the martensitic transformation, and the deformation constraints lead to stress concentration. These figures suggest that a possible way to quantify the level of elastic incompatibility is to compare the growth of the von Mises stress at the grain boundary relative to the single crystal response during the elastic range. Similarly, one way to quantify the transformation incompatibility is to compare the von Mises stress at the grain boundary relative to the single crystal response at a certain strain level during transformation.

Note that up to this point, we used von Mises stress as a metric as it is representative of complex deviatoric stress states. As mentioned in Chapter 1, the martensitic transformation in zirconia-based SMCs involves a significant volume change, and normal stresses along with shear stresses can trigger the transformation. Therefore, it is important to also examine the sensitivity of both types of incompatibilities to volumetric stresses. To this end, we compared the hydrostatic stress $p = \frac{\sigma_{11}+\sigma_{22}+\sigma_{33}}{3}$ in single crystals and at bi-crystal grain boundaries. Figure 4-9a shows the maximum hydrostatic pressure at the bi-crystal grain boundary plane compared to the single crystals for Case 1 where the grain configuration has high elastic incompatibility. During the elastic range, sizable stress concentrations can be observed at the bi-crystal grain boundary. What's more interesting is that during the transformation, there

(a) von Mises stress at a bi-crystal cross section parallel to $x - z$ plane at $\epsilon = 0.3\%$

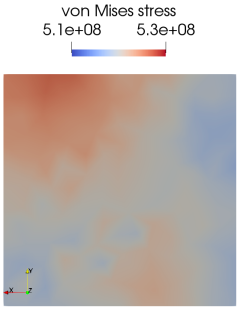

(b) von Mises stress at a bi-crystal cross section parallel to $x - y$ plane at $\epsilon = 0.3\%$

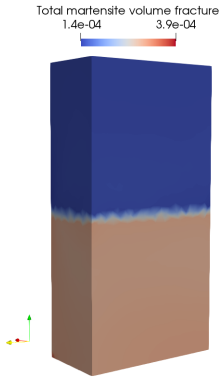

(c) Corresponding total martensite volume fraction at $\epsilon = 0.3\%$

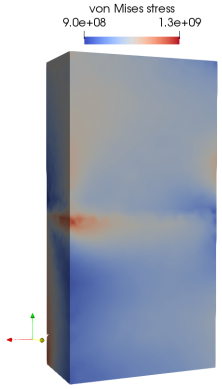

(d) von Mises stress at a bi-crystal cross section parallel to $x - z$ plane at $\epsilon = 2\%$

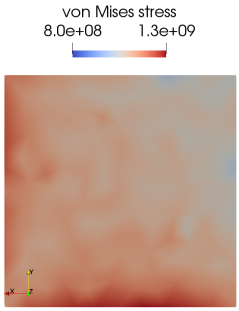

(e) von Mises stress at a bi-crystal cross section parallel to $x - y$ plane at $\epsilon = 2\%$

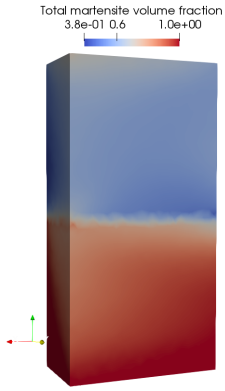

(f) Corresponding total martensite volume fraction at $\epsilon = 2\%$

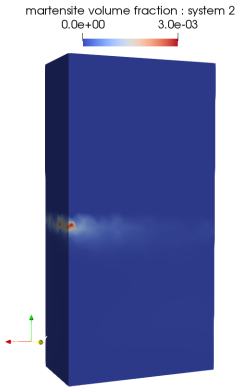

(g) Martensite volume fraction in system 2 at $\epsilon = 2\%$

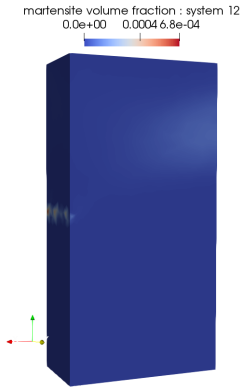

(h) Martensite volume fraction in system 12 at $\epsilon = 2\%$

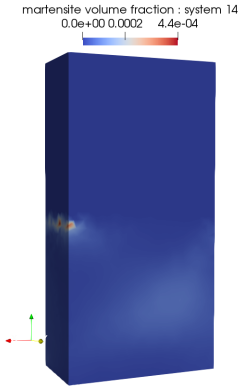

(i) Martensite volume fraction in system 14 at $\epsilon = 2\%$

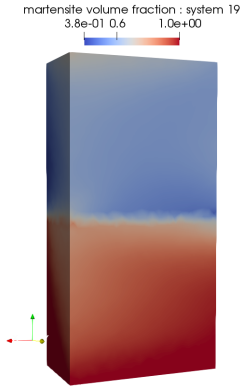

(j) Martensite volume fraction in system 19 at $\epsilon = 2\%$

Figure 4-7: Contours of: (a) von Mises; (c) martensite volume fraction in the bi-crystal cross-section with normal y; (b) von Mises in the bi-crystal cross-section with normal z at $\epsilon = 0.3\%$; (d) von Mises; (f)-(j) martensite volume fraction in the bi-crystal cross-section with normal y; (e) von Mises in the bi-crystal cross-section with normal z at $\epsilon = 2\%$. Figures (a)-(c) illustrate that there is no significant stress concentration near the bi-crystal interface at this low strain level. Figures (d)-(j) show that at a higher strain level, the bottom crystal has almost fully transformed and there is a strong stress concentration near the bi-crystal grain boundary. System 19 is the most favorably oriented system for transformation.

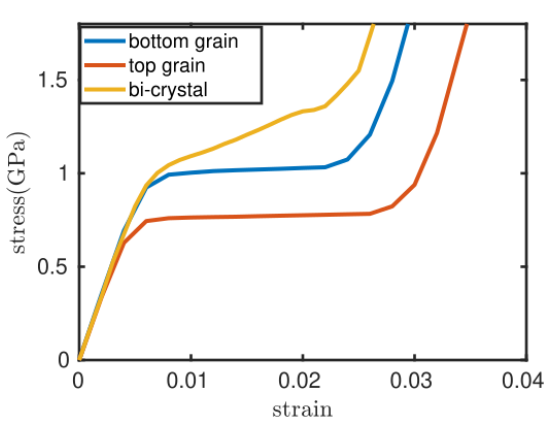

(a) Maximum von Mises stress at the grain boundary plane in bi-crystal and single crystals

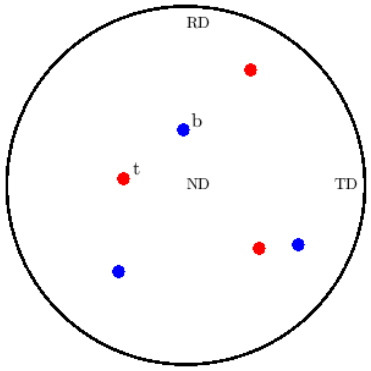

(b) Pole figure showing the [001] [010] [110] poles of the top (red, with the long axis labeled as 't') and bottom grain (blue, with the long axis labeled as 'b')

Figure 4-8: Grain boundary configuration with low elastic incompatibility

is a significant pressure increase at the grain boundary, while the von Mises stress plateaus during transformation, as shown in Figure 4-6c. As a result, the maximum hydrostatic pressure at the grain boundary is about 1.7 times larger than that in the bottom grain at 2% strain. Figure 4-9b shows the respective result for Case 2 where the elastic incompatibility is low, yet the transformation incompatibility is high. We can also observe a buildup of pressure during transformation, which can be attributed to the significant volume expansion.

Having established the two basic types of sources of incompatibilities, we subsequently conducted a series of simulations with 43 different orientations of the top grain with the orientation of the bottom grain fixed. The grain misorientations presented in a pole figure can be found in Figure 4-10. We used the ratio of the initial rate of growth of the von Mises stress at the bi-crystal grain boundary relative to the single crystal response of the bottom grain as a measure of the grain boundary stiffness induced by elastic incompatibility. Similarly, we used the ratio of the von Mises stress at the bi-crystal grain boundary at 2.2% strain (stress concentration factor), relative to the single crystal response of the bottom grain to measure transformation incompatibility. The original data generated from the finite element simulations can

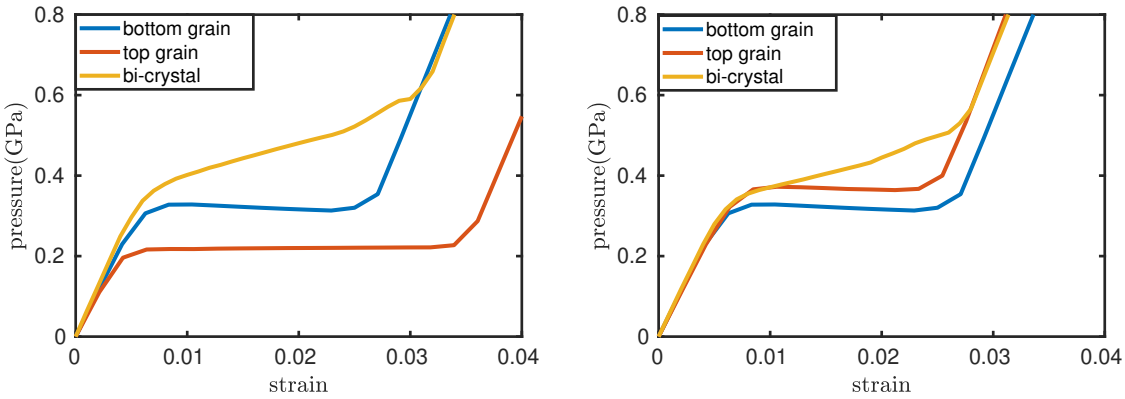

(a) Case 1: elastic incompatibility (b) Case 2: transformation incompatibility

Figure 4-9: Maximum hydrostatic stresses at the grain boundary plane in bi-crystal and single crystals

be found in Figure A-1a and A-1b in Appendix A, respectively.

Figure 4-11a shows the grain boundary stiffness ratios in 43 bi-crystal specimens and their disorientation angles. Each point represents a bi-crystal with a disorientation angle defined as the minimum rotation angle with the misorientation axis located in the Standard Stereographic Triangle (SST). It can be observed that among these bi-crystals with various misorientations, the largest stiffness ratio is slightly below 1.2, suggesting that in general elastic incompatibility in this zirconia-based SMC is rather low. One can also notice that there is a correlation between disorientation angles and elastic incompatibilities particularly for specimen with high disorientation angles. Most bi-crystal specimens with smaller disorientation angles are shown to have small stiffness ratios. By contrast, when the disorientation angle is larger, elastic incompatibility is higher which results in larger stress concentrations in the elastic range. It is worth noting that the two bi-crystals with smallest disorientation angles appear to be outliers with much larger incompatibilities from elasticity than those with disorientation angles between 30° to 50°.

Figure 4-11(b) shows the respective results of maximum von Mises stress concentration factor at the grain boundary plane at 2.2% strain. Among the 43 bi-crystals, the largest von Mises stress concentration factor is 3.1 and it occurs in the bi-crystal with a disorientation angle about 70°. As demonstrated in Figure 4-11(b), bi-crystals

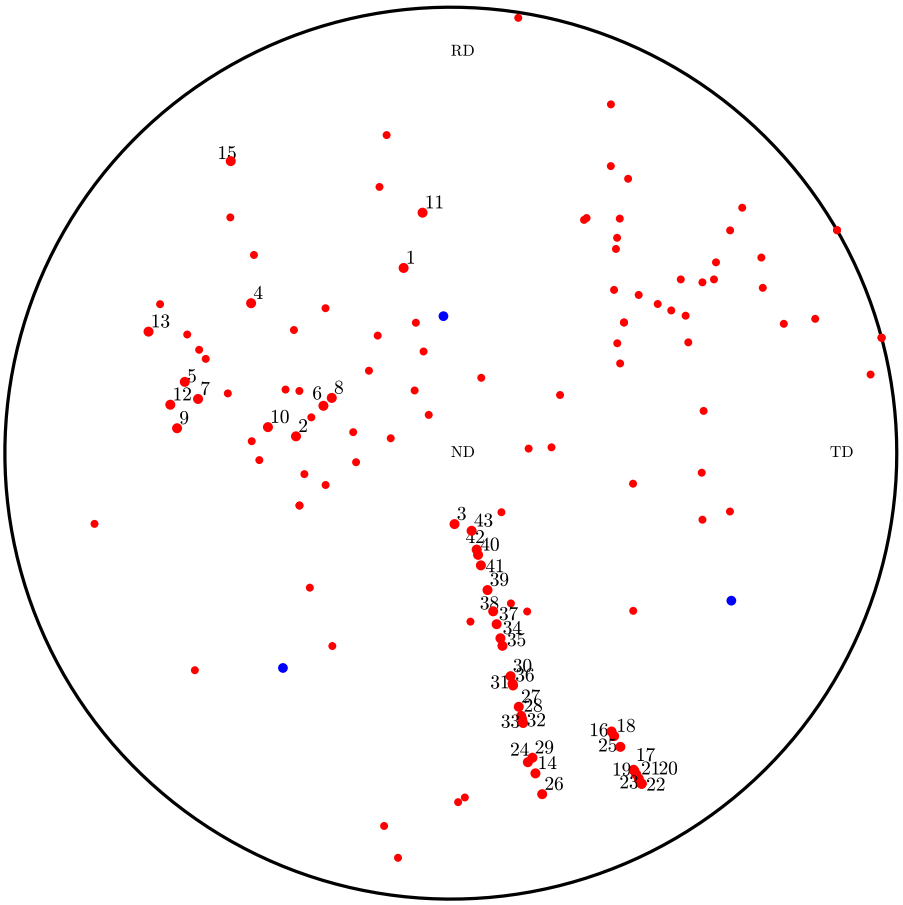

Figure 4-10: A pole figure showing the $[100], [010], [001]$ crystal directions of the bottom (blue) and top grain (red) of 43 bi-crystals studied in the simulations with the long axis [001] pole labeled

with larger von Mises stress and therefore higher transformation incompatibility often correspond to larger disorientation angles, with some outliers in the results especially for samples with small orientation angles.

We repeated the analysis for bi-crystals with a different bottom grain orientation (Euler angles = [194,46,235]) and 17 different orientations for top grain. The corresponding results are shown in Figure 4-12. Similar conclusions can be drawn; bi-crystals with larger disorientation angles tend to exhibit a higher level of elastic

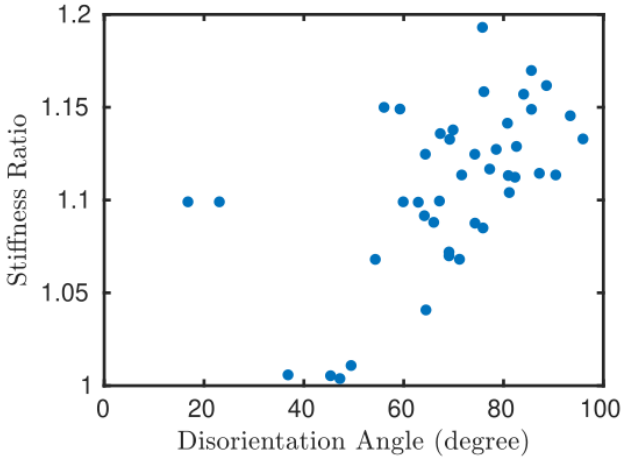

(a) Grain boundary stiffness ratio

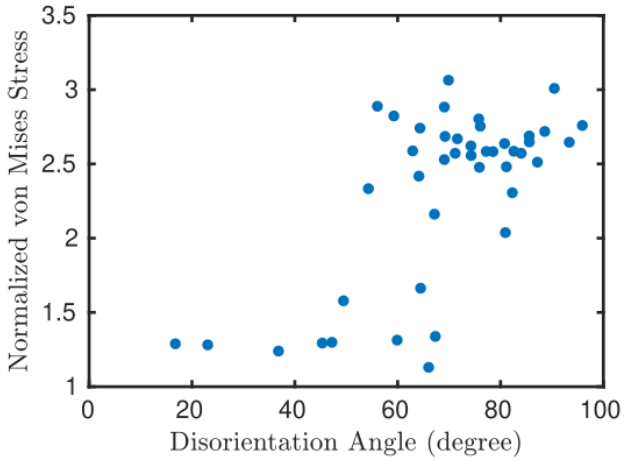

(b) Normalized maximum von Mises stress at 2.2% strain level

Figure 4-11: Quantitative indicators of elastic and transformation incompatibility at bi-crystal grain boundary vs. disorientation angles (bottom grain Euler angle [3, 146, 306])

and transformation incompatibilities. Although there exist a few outliers, bi-crystals with disorientation angles between $10 - 40°$ have relatively lower stiffness ratios and normalized von Mises stresses. The original data generated from the finite element simulations can be found in Figure A-2a and A-2b in Appendix A, respectively.

A few observations can be made from Figures 4-11 and 4-12. Elastic incompatibilities in zirconia are lower in magnitude compared incompatibilities resulting from the martensitic transformation. These results also suggest that the correlation between

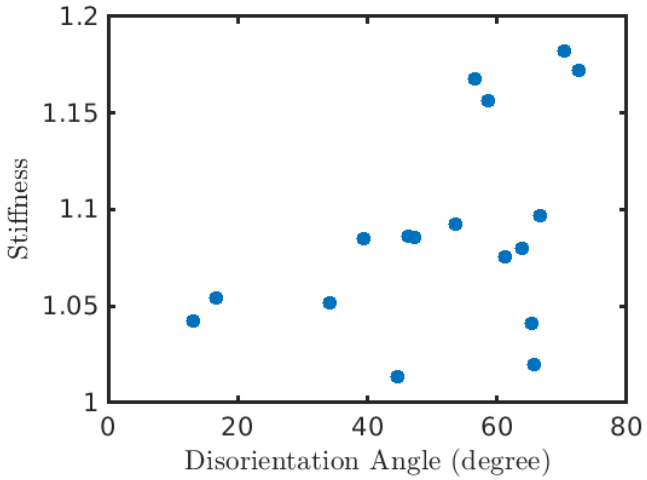

(a) Grain boundary stiffness ratio

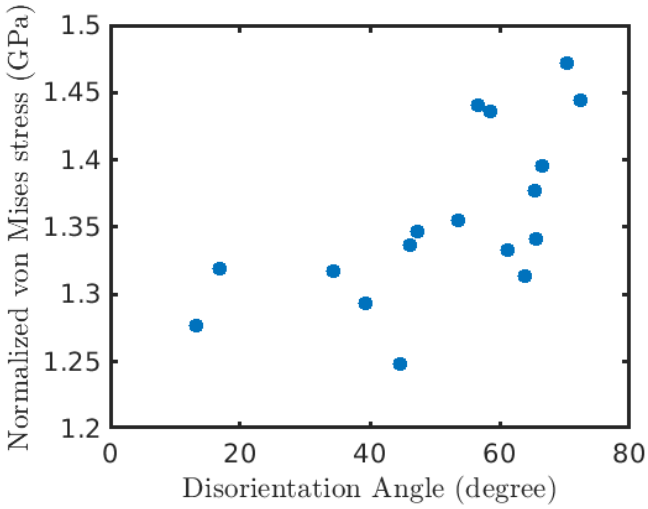

(b) Normalized maximum von Mises stress at 2.2% strain level

Figure 4-12: Quantitative indicators of elastic and transformation incompatibility at bi-crystal grain boundary vs. disorientation angles (bottom grain Euler angle [194,46,235])

disorientation angles and stress concentration factors is more evident in samples with large orientation angles, yet the correlation is not very clear for samples with smaller disorientation angles.

4.3 Conclusion

In this chapter, we conducted a simulation study attempting to characterize the sources and magnitude of strain incompatibility at bi-crystal interfaces in SMCs. To this end, we implemented a micromechanics-based model for SMCs incorporating both elastic and transformation anisotropy at the grain level. We incorporated the non-Schmid effect into the model to account for the volume changes during martensitic transformation which is a unique feature for zirconia-based SMCs. The model was calibrated against micro-compression tests conducted in [6, 76] and shown to capture the orientation-dependence of transformation fairly accurately. Three-dimensional finite element simulations using the micromechanical model enabled the investigation of the evolution of stress concentrations at the grain boundary due to either elastic or transformation strain incompatibility, as well as the analysis of the evolution of the martensite volume fraction, which has not been addressed in SMCs before. The following conclusions can be drawn from the finite element simulation results and analysis,

- Strong dependency of the level of stress concentration at the grain boundary on the crystal boundary misorientations can be observed in SMCs.

- Upon identifying two particular cases with distinct stress-strain responses, we observed that elastic anisotropy leads to severe deformation incompatibility and high von Mises stress concentration at the grain boundary at relatively low strains. When the two grains were elastically compatible, however, high stress concentrations at the grain boundary and transformation strain incompatibilities were still possible due to the anisotropic nature of the martensitic transformation.

- We extracted information about the stress-strain response and the level of strain incompatibilities at grain boundaries from the finite element simulation results and analyzed the relationship between different types of incompatibilities and disorientation angles, a specific metric for characterizing grain boundaries. The

results demonstrated that there was a clear correlation between both elastic and transformation incompatibilities and disorientation angles.

- The approach adopted in this work could be used to identify misorientations that reduce or minimize elastic and transformation incompatibility, thus potentially realizing the superelastic properties and achieving the ductility limits approaching those of single crystals SMCs.

Chapter 5

Conclusions and Future Work Directions

5.1 Conclusions

The objective of this thesis was to improve our understanding of the competition between martensitic transformation, grain boundary constraints, and intergranular fracture in shape memory materials through comprehensive computational modeling. To this end, we accomplished the following goals:

- We implemented a comprehensive computational framework for simulating the deformation of oligocrystalline SMAs and zirconia-based SMCs subjected to general loadings. An anisotropic rate-dependent constitutive model was built upon the framework of previously developed micromechanics-based models and was implemented in the in-house computational framework **ΣMIT**. A robust explicit algorithm was developed to update the constitutive law. We extended the modeling framework to account for the non-Schmid effect observed during phase transformation in SMCs.

- In the case of Cu-based SMAs, previous studies showed that the presence of occasional grain boundaries and triple junctions in the oligocrystal structure can originate incompatibility of deformation due to either elastic or transfor-

mation anisotropy, which induced stress concentrations and leads to premature intergranular fracture. To this end, we utilized the model to analyze elastic and transformation anisotropy at a grain level to gain insights into the sources of deformation incompatibility at bi-crystal grain boundaries which are potentially responsible for premature intergranular fracture in oSMAs.

- From the finite element simulation results of bi-crystal Cu-based SMAs, we observed that the level of stress concentration at the grain boundary as measured by the maximum von Mises stress strongly depended on the crystal boundary misorientation. The large elastic anisotropy Cu-based SMAs often lead to severe deformation incompatibility and high von Mises stress concentration at the grain boundary at relatively low strains. When the crystals were elastically compatible, however, high stress concentrations at the grain boundary, and therefore transformation strain incompatibilities were still possible due to the anisotropic nature of the martensitic transformation.

- We also explored the correlation between grain boundary characteristics (CSL and disorientation angles) and different types of incompatibilities arising at grain boundaries in bi-crystal Cu-based SMAs. We demonstrated that grain boundaries with low CSL order exhibited low elastic incompatibilities in Cu-based SMAs, as previously suggested from experimental observations. However, high CSL order grain boundaries can result in incompatibilities that were commensurate with those exhibited by random grain boundary configurations.

- In the case of SMCs, the model was calibrated against micro-compression tests conducted in [6, 76] and shown to capture the orientation-dependence of transformation fairly accurately. Three-dimensional finite element simulations using the micromechanical model enabled the investigation of the evolution of stress concentrations at the grain boundary due to either elastic or transformation strain incompatibility, as well as the analysis of the evolution of the martensite volume fraction.

- From the finite element simulation results of SMCs, we identified grain boundary configurations which result in very large stress concentrations at very low deformations due to elastic incompatibility, as well as others where the elastic incompatibility is relatively low and stress concentrations only occur at large transformation strains. We also analyzed the relationship between different types of incompatibilities and grain boundary characteristics, and the results indicated a correlation between both types of strain incompatibilities and the disorientation angle, in particular for samples with larger disorientation angles.

- Our study shed light on the competing mechanisms of elastic and transformation incompatibilities leading to severe stress concentration at the grain boundaries. This approach could be used to identify misorientations that reduce or minimize elastic and transformation incompatibility, thus extending the superelastic range of shape memory materials to potentially achieve the ductility limits of single crystals.

5.2 Future work

5.2.1 Size effects in zirconia-based SMCs

An important observation in [75, 6] is that martensitic transformation in zirconia strongly depends on structural length scales of the micro-pillar sample, and that there is potential coupling effect of both size and orientation dependency. Therefore it is of great interest to incorporate the size-dependency into the constitutive model to account for the size effects in zirconia observed in [6, 75].

Both the intrinsic (related to grain size) and extrinsic size effects (related to sample size, e.g. diameter or thickness) have been widely recognized in various SMAs [68, 67, 66, 70, 177, 178, 53, 179, 180]. A considerable amount of previous efforts has been dedicated to incorporating the size-dependency in modeling the martensitic transformation and shape memory properties in SMAs [181, 182, 183, 114, 184, 116, 185, 186, 187, 151, 188, 146]. The modeling approach in [183, 114] combines a supere-

lasticity formulation based on the martensitic volume fraction with gradient plasticity theory [189, 190, 191] to account for size effects that arise at the nano-scale due to grain interactions and free surfaces. Size effects are incorporated through two internal length scales, an energetic length scale and a dissipative length scale, which correspond to the gradient terms in the free energy and the dissipation, respectively. However, the combination of gradient plasticity theory with a multi-system anisotropic constitutive framework is much more challenging and involved and such models have not yet been developed for phase transformation in shape memory materials to our knowledge. The major challenge is to address the coupling of size dependency and orientation effect, which has not been systematically studied experimentally or numerically. The orientation dependent size effect observed in [6] was based on data from only a few samples with different orientations. A more comprehensive study including more fabricated pillars with a wide range of orientations and grain sizes would be extremely valuable to advance further understanding of the coupling of size effects and orientation dependency in zirconia-based SMCs.

5.2.2 Modeling the oligocrystal particle interactions response via an anisotropic contact model

Previous discussions have clearly shown that when made into small volumes, zirconia-based SMCs may exhibit several intriguing mechanical properties, and can potentially survive many superelastic loading cycles without cracking or fracturing. Though these newly-developed SMCs in small-volumes exhibit better energy absorption properties, which brittle ceramics lacked, these micro-scale zirconia pillars are not ideally suited for large-volume applications. Recent work [192, 95, 96] has been focusing on developing granular oligocrystalline packings of SMCs as an aggregate particle system to maximum the energy dissipation. From the modeling perspective, this requires the capacity to model oligocrystal particle interactions using a Hertz-like model for anisotropic superelastic materials. Ideally, the finite element simulation results will serve as a basis to transfer bulk mechanical behaviors into contact relations between

particle pairs of different sizes and shapes and one can extract representative and realistic particle contact laws based on the mechanical behavior of the particles. This will provide the groundwork for upscaled modeling (e.g. Discrete Element Method) to study interaction among a large number of particles. Previous efforts have been made to implement a contact law between two elastically anisotropic bodies using the Discrete Element Method [193]. However, the challenge of developing a Hertz contact model for anisotropic particles undergoing martensitic transformation has not been addressed to our knowledge.

5.2.3 Modeling More Complex Mechanisms during Transformation

- The strain incompatibility in shape memory materials can also derive from the interaction between the different martensite variants. Due to the lack of adequate previous work on the interaction matrix for zirconia-based SMCs that would allow us to calibrate the additional model parameters involved in variants interactions, the interactions among transformation systems were ignored in our model. Previous work has offered a straightforward method in including the variant interactions effects in constitutive models for SMAs [132], and extending this work to zirconia-based SMCs would be an important addition.

- One could consider incorporating possible plastic deformation into the model. The incorporation of both plastic deformation and martensite transformation is a common practice in modeling of SMAs. However due to the lack of experimental results in zirconia-based SMCs, we didn't consider plastic deformation to be part of the model in this work. This should be revisited in subsequent work given more available experimental data.

- In this work, we adopted the common practice of treating grain boundaries in FEM with conforming meshes. Considering the lack of any data specific to grain boundary response that would allow a quantitative evaluation of their

effect in the case of zirconia-based SMCs, we believe the grain boundary conformity assumption can still result in valuable information about deformation incompatibility due to grain boundary misorientation. As more experimental data becomes available, it would be desirable to describe mechanisms of deformation and failure at grain boundaries explicitly as done in models of crystal plasticity of metals [194, 195].

- Defects such as point defects or dislocations, can significantly affect the behavior of ceramics. Defects also play a much larger role in micro-pillar experiments due to the ratio of specimen size to defect size. Our current model does not include the role of defects, as detailed information about the defects and their distribution were challenging to ascertain and are not available as of now. This is likely one of the sources of error in the calibration and analysis [6]. Incorporating a detailed description about the defects and their distribution in the model when more experimental evidence becomes available would be extremely valuable future work.

- Some recent work has studied the role of grain boundary in SMCs subject to thermal cyclic loading[95, 96]. The simulations in this thesis were conducted in isothermal conditions, and it would be very interesting to simulate the material's response in thermal loading and thermo-mechanically coupled situations.

Appendix A

Elastic and transformation incompatibility at SMC grain boundaries

Figures A-1a and A-1a respectively show the stiffness ratio and the normalized von Mises stress of the 43 cases presented in Chapter 4 where the Euler angles of the bottom grain are fixed at [3, 146, 306]. Figures A-2a and A-2b respectively show the stiffness ratio and the normalized von Mises stress of the 17 cases with a different orientation of the bottom grain (Euler angles [194,46,235]).

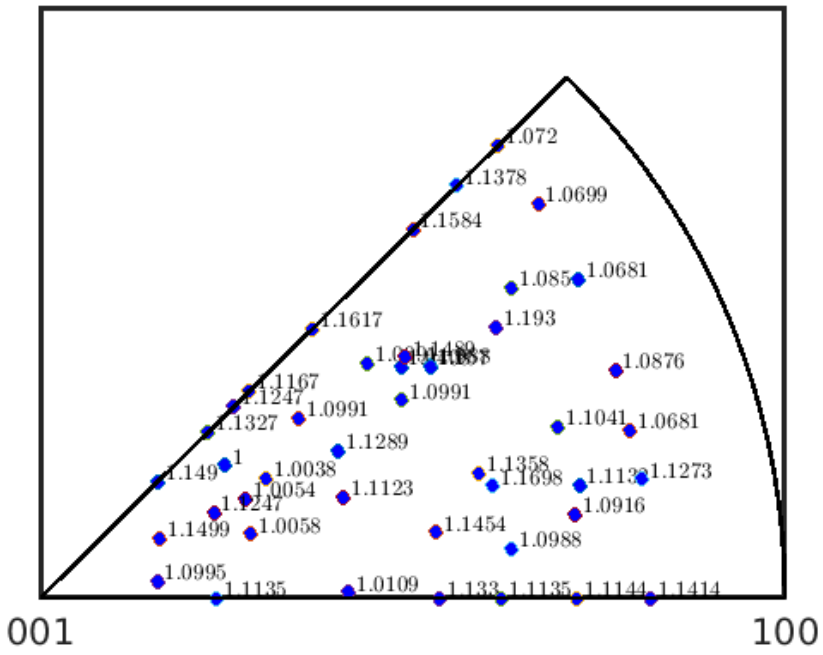

(a) Stiffness ratio/elastic incompatibility

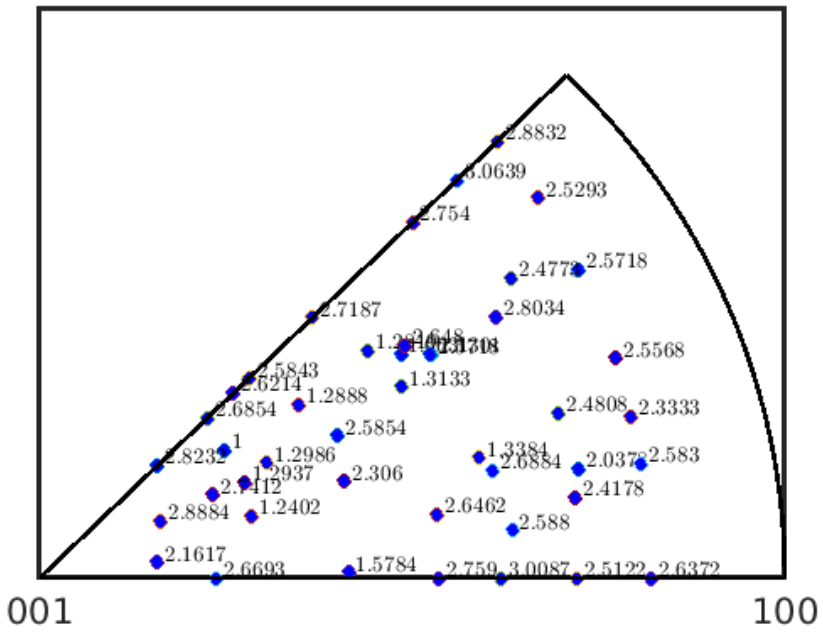

(b) Normalized von Mises stress/transformation incompatibility

Figure A-1: Quantified elastic and transformation incompatibility of all samples on a [001] inverse pole figure. Bottom grain Euler angles = [3, 146, 306]

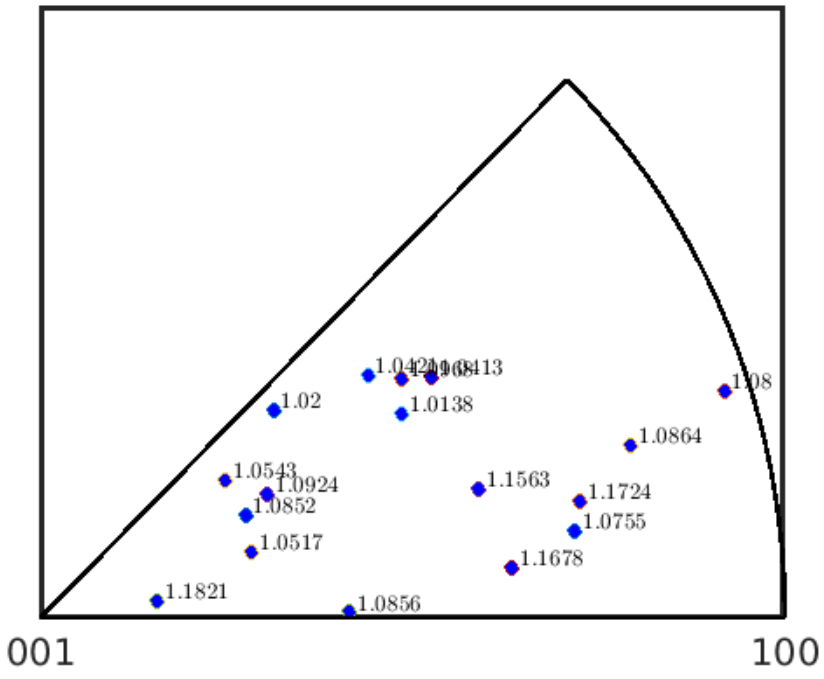

(a) Stiffness ratio/elastic incompatibility

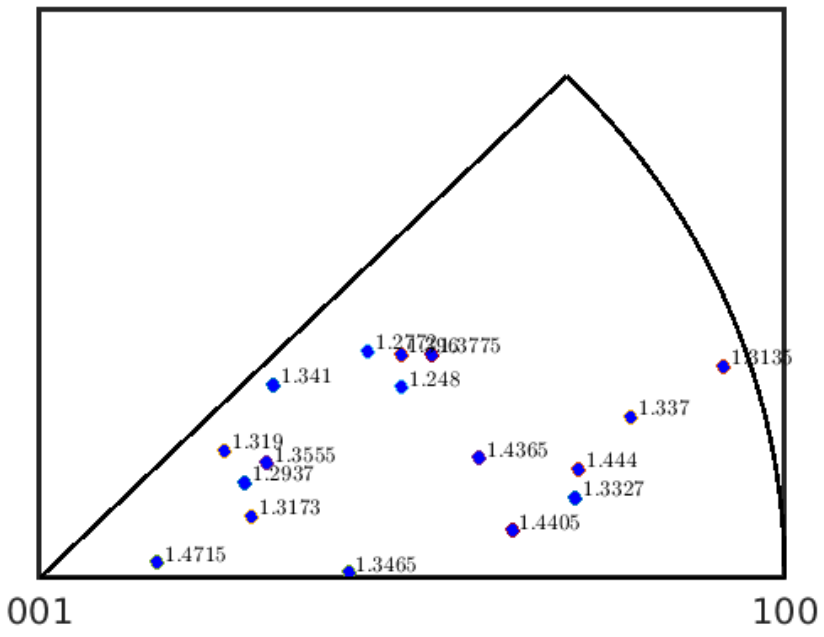

(b) Normalized von Mises stress/transformation incompatibility

Figure A-2: Quantified elastic and transformation incompatibility of all samples on a [001] inverse pole figure. Bottom grain Euler angles = [194,46,235]

Appendix B

Geometrically Nonlinear Theory of Martensite

B.1 Identifying martensite variants

In the section, the application of the geometrically nonlinear theory to different shape memory materials is summarized, following the work in [13, 196, 122]. To calculate all possible transformation systems in a specific single-crystal, only the lattice parameters of the two phases and the lattice distortions, referred to here as the transformation stretch matrices, are needed as inputs to the calculations; no assumption of a lattice invariant shear is required. The theory is built upon the assumption that the microstructure of martensite results from energy minimization and strain compatibility. An energy functional dependent on atomic positions and temperature is postulated, where this functional has multiple energy wells for the different phases. This permits a change of stability between the phases upon either a change in temperature or stress. The theory assumes that there is a single critical temperature θ_{ms} at which the martensitic transformation occurs. At the critical temperature, the austenite and martensite phases are both stable, while the martensite phase is stable when the temperature is below θ_{ms}, and the austenite phase is stable above θ_{ms}. The starting point of the calculation is to identify the tensor that maps a Bravais lattice of the austenite phase to a that of the martensite phase. This deformation depends upon

the change in symmetry during the transformation and the lattice parameters of the two phases. As discussion in Chapter 1, the deformation is not unique, and one is found for each of the symmetry related configurations of the martensite lattice to the variants of martensite. With the knowledge of the transformation tensor, a macroscopic continuum model can be obtained from the microscopic atomic model through the Cauchy-Born rule [197]. The energy functional depends on the macroscopic deformation gradient and temperature. A microstructure is essentially a homogeneous deformation with gradient solely on the energy wells, and the geometrical construction of a microstructure can be reduced to studying certain microscopic compatibility equations at the phase boundaries between the austenite and martensite phases as well as different martensite variants.

The procedure is summarized in the following sections. Take NiTi SMAs for example where the martensitic transformation is from a B2 cubic parent phase to a distorted B19' monoclinic product phase. This mechanism is divided into three steps: (1) uniform expansion or contraction along the direction e_1 (2) shuffling of the atoms in the middle plane with normal e_2 in the direction e_3; the shuffling ensures a close-packed martensitic structure. (3) shear in the plane with normal e_3. The deformation gradient reads,

$$\mathbf{F} = \begin{pmatrix} 1 & cos\theta & 0 \\ 0 & 1 & 0 \\ 0 & 0 & 1 \end{pmatrix} \begin{pmatrix} \alpha & 0 & 0 \\ 0 & \gamma sin\theta & 0 \\ 0 & 0 & \beta \end{pmatrix} = \begin{pmatrix} \alpha & \gamma cos\theta & 0 \\ 0 & \gamma sin\theta & 0 \\ 0 & 0 & \beta \end{pmatrix} \tag{B.1}$$

where $\alpha = a/a_0$, $\beta = b/\sqrt{(}2a_0)$,$\gamma = c/\sqrt{(}2a_0)$ are the transformation stretches and θ is the angle between the edges with lengths a and c.

We then calculate the transformation stretch matrix $\mathbf{U} = \sqrt{(\mathbf{F^T F})}$. Once the components of a transformation stretch matrix $\mathbf{U}$ (denoted as $\mathbf{U}_1$) are obtained, all other transformation stretch matrices can be found as the unique matrices in the set $\left\{\mathbf{R}\mathbf{U}_1\mathbf{R}^T, R \in \mathcal{P}_a\right\}$, where $\mathcal{P}_a$ is the point group of the austenite. The number of unique matrices in this set is 12, and these transformation stretch matrices

$\mathbf{U}_2, \cdots, \mathbf{U}_{12}$ are referred to as the variants of $\mathbf{U}_1$. The components of all the monoclinic martensite variants in the cubic basis are

$$\mathbf{U}_1 = \begin{pmatrix} \theta & \rho & \rho \\ \rho & \sigma & \tau \\ \rho & \tau & \sigma \end{pmatrix} \mathbf{U}_2 = \begin{pmatrix} \theta & -\rho & -\rho \\ -\rho & \sigma & \tau \\ -\rho & \tau & \sigma \end{pmatrix} \mathbf{U}_3 = \begin{pmatrix} \theta & -\rho & \rho \\ -\rho & \sigma & -\tau \\ \rho & -\tau & \sigma \end{pmatrix} \mathbf{U}_4 = \begin{pmatrix} \theta & \rho & -\rho \\ \rho & \sigma & -\tau \\ -\rho & -\tau & \sigma \end{pmatrix}$$

$$\mathbf{U}_5 = \begin{pmatrix} \sigma & \rho & \tau \\ \rho & \theta & \rho \\ \tau & \rho & \sigma \end{pmatrix} \mathbf{U}_6 = \begin{pmatrix} \sigma & -\rho & \tau \\ -\rho & \theta & -\rho \\ \tau & -\rho & \sigma \end{pmatrix} \mathbf{U}_7 = \begin{pmatrix} \sigma & -\rho & -\tau \\ -\rho & \theta & \rho \\ -\tau & \rho & \sigma \end{pmatrix} \mathbf{U}_8 = \begin{pmatrix} \sigma & \rho & -\tau \\ \rho & \theta & -\rho \\ -\tau & -\rho & \sigma \end{pmatrix}$$

$$\mathbf{U}_9 = \begin{pmatrix} \sigma & \tau & \rho \\ \tau & \sigma & \rho \\ \rho & \rho & \theta \end{pmatrix} \mathbf{U}_{10} = \begin{pmatrix} \sigma & \tau & -\rho \\ \tau & \sigma & -\rho \\ -\rho & -\rho & \theta \end{pmatrix} \mathbf{U}_{11} = \begin{pmatrix} \sigma & -\tau & \rho \\ -\tau & \sigma & -\rho \\ \rho & -\rho & \theta \end{pmatrix} \mathbf{U}_{12} = \begin{pmatrix} \sigma & -\tau & -\rho \\ -\tau & \sigma & \rho \\ -\rho & \rho & \theta \end{pmatrix}$$

where the specific components are

$$\theta = \frac{\alpha(\alpha + \gamma sin\theta)}{\sqrt{\alpha 2 + \gamma^2 + 2\alpha\gamma sin\theta}}$$
$$\rho = \frac{\alpha\gamma cos\theta}{\sqrt{2}\sqrt{\alpha 2 + \gamma^2 + 2\alpha\gamma sin\theta}}$$
$$\sigma = \frac{1}{2}\frac{\gamma(\gamma + \alpha sin\theta)}{\sqrt{\alpha 2 + \gamma^2 + 2\alpha\gamma sin\theta}} + \beta$$
$$\tau = \frac{1}{2}\frac{\gamma(\gamma + \alpha sin\theta)}{\sqrt{\alpha 2 + \gamma^2 + 2\alpha\gamma sin\theta}} - \beta$$

The eigenvalues $\lambda^{(1)}, \lambda^{(2)}, \lambda^{(3)}$ of these symmetric matrices are $\lambda^{(1)} = \beta$,

$$\lambda^{(2)} = \frac{\sqrt{\alpha 2 + \gamma^2 + 2\alpha\gamma sin\theta} - \sqrt{\alpha 2 + \gamma^2 - 2\alpha\gamma sin\theta}}{2},$$

$$\lambda^{(3)} = \frac{\sqrt{\alpha 2 + \gamma^2 + 2\alpha\gamma sin\theta} - \sqrt{\alpha 2 + \gamma^2 - 2\alpha\gamma sin\theta}}{2}$$

B.2 Energy minimization

B.2.1 Energy wells

Since a rigid rotation does not change the state of the crystal or induce the martensitic transformation, the austenite phase corresponds not only to the identity matrix but to all rotation matrices $\mathbf{Q}$. The austenite and the variants of martensite can be described as follows:

$$\begin{aligned}
\mathcal{A} &= \{\mathbf{F} : \mathbf{F} = \mathbf{Q} \text{ for some rotation } \mathbf{Q}\} \\
\mathcal{M}_1 &= \{\mathbf{F} : \mathbf{F} = \mathbf{Q}\mathbf{U}_1 \text{ for some rotation } \mathbf{Q}\} \\
&\cdots \\
\mathcal{M}_N &= \{\mathbf{F} : \mathbf{F} = \mathbf{Q}\mathbf{U}_N \text{ for some rotation } \mathbf{Q}\}
\end{aligned}$$

where N is the number of variants, which can be obtained based on the knowledge of point groups of the martensite ($\mathcal{P}_m$) and austenite ($\mathcal{P}_a$):

$$N = \frac{\text{the number of rotations in } \mathcal{P}_a}{\text{the number of rotations in } \mathcal{P}_m}$$

It is worth emphasizing that all the variants have the same energy according to material symmetry, and the energy density is minimized on the austenite well $\mathcal{A}$ at high temperatures and on the martensite wells $\mathcal{M}$ at low temperatures and on both the austenite and martensite wells at the transformation temperature θ_{ms}.

$$\begin{aligned}
\psi(\mathbf{G},\theta) \leq \psi(\mathbf{F},\theta), \text{for all } \mathbf{G} \in \mathcal{A} \text{ and for all } \mathbf{F} \quad \theta > \theta_{ms} \\
\psi(\mathbf{G},\theta) \leq \psi(\mathbf{F},\theta), \text{for all } \mathbf{G} \in \mathcal{A} \cup \mathcal{M} \text{ and for all } \mathbf{F} \quad \theta = \theta_{ms} \\
\psi(\mathbf{G},\theta) \leq \psi(\mathbf{F},\theta), \text{for all } \mathbf{G} \in \mathcal{M} \text{ and for all } \mathbf{F} \quad \theta < \theta_{ms}
\end{aligned} \tag{B.2}$$

Therefore the task of identifying the energy minimizing configurations for martensitic transformation is reduced to looking for deformations $\mathbf{y}$ with the deformation gradient $\nabla\mathbf{y}$ in the relevant energy wells. The essential steps to identify these configurations

are summarized in the following sections.

B.2.2 Twinning in martensite

The deformation $\mathbf{y}$ corresponding to two variants I and J of the martensite can be denoted as,

$$\nabla \mathbf{y} = \begin{cases} \mathbf{Q}_1 \mathbf{U}_I \text{ in } \Omega_1 \\ \mathbf{Q}_2 \mathbf{U}_J \text{ in } \Omega_2 \end{cases} \tag{B.3}$$

for some rotations $\mathbf{Q}_1$, $\mathbf{Q}_2$. For the deformation to be continuous, the kinematic compatibility condition must be satisfied,

$$\mathbf{Q}_1 \mathbf{U}_I - \mathbf{Q}_2 \mathbf{U}_J = \mathbf{b} \otimes \hat{\mathbf{n}} \tag{B.4}$$

for some vectors $\mathbf{b}$ and $\hat{\mathbf{n}}$. Premultiply by $\mathbf{Q}_2^T$ and we have the twinning equation,

$$\mathbf{Q}\mathbf{U}_I - \mathbf{U}_J = \mathbf{a} \otimes \hat{\mathbf{n}} \tag{B.5}$$

Given $\mathbf{U}_I$ and $\mathbf{U}_J$, one can find $\mathbf{Q}, \mathbf{a}, \hat{\mathbf{n}}$ by solving the twinning equation following the steps,

1. Calculate $\mathbf{C} = \mathbf{G}^{-T}\mathbf{F}^{-T}\mathbf{F}\mathbf{G}^{-1}$.

2. If $\mathbf{C} = \mathbf{I}$, there is no solution.

3. If $\mathbf{C} \neq \mathbf{I}$, calculate the eigenvalues of $\mathbf{C}$ and number them so that $\lambda_1 \leq \lambda_2 \leq \lambda_3$.

4. The twinning equation has a solution if and only if the eigenvalues satisfy $\lambda_1 \leq 1, \lambda_2 = 1, \lambda_3 \geq 1$.

5. If the inequality in step 4 holds, then there are two solutions given by:

$$\begin{aligned}\mathbf{a} &= \rho\left(\sqrt{\frac{\lambda_3(1-\lambda_1)}{\lambda_3-\lambda_1}}\hat{\mathbf{e}}_1 + \mathcal{K}\sqrt{\frac{\lambda_1(\lambda_3-1)}{\lambda_3-\lambda_1}}\hat{\mathbf{e}}_3\right), \\ \hat{\mathbf{n}} &= \frac{\sqrt{\lambda_3}-\sqrt{\lambda_1}}{\rho\sqrt{\lambda_3-\lambda_1}}\left(-\sqrt{1-\lambda_1}\mathbf{G}^{\mathbf{T}}\hat{\mathbf{e}}_{\mathbf{1}} + \mathcal{K}\sqrt{\lambda_3-1}\mathbf{G}^{\mathbf{T}}\hat{\mathbf{e}}_{\mathbf{3}}\right),\end{aligned} \tag{B.6}$$

where $\mathcal{K} = \pm 1, \rho \neq 0$ is chosen to make $|\hat{\mathbf{n}}| = 1$, and $\hat{\mathbf{e}}_i$ are the eigenvectors of $\mathbf{C}$ corresponding to the eigenvalues λ_i. Choosing $\mathcal{K} = \pm 1$ gives us two solutions and we can subsequently obtain $\mathbf{Q}$ by substituting $\mathbf{a}, \hat{\mathbf{n}}$ back into the twinning equation. The matrix $\mathbf{C}$ describes the deformation of one side relative to the other and its eigenvalues describe the stretches of one side relative to the other. If the two sides are coherent, we need to find a plane which is relatively unstretched. This is possible if and only if (a), one of the three stretches is equal to one and (2) the other two stretches straddle one.

To obtain all admissible twinning configurations $\mathbf{Q}, \mathbf{a}, \hat{\mathbf{n}}$, this procedure should be applied to all possible pairs of martensite variants.

B.2.3 Solving the habit plane equation

After obtaining the twinning solutions, we can then identify the interface between the austenite and twinned martensite. A schematic description of phase twinning as parallel bands alternately containing different variants of martensite can be found in Figure B-1. To ensure the deformation is continuous and its gradient exists, the following compatibility equation has to be satisfied,

$$(\lambda\mathbf{A} + (1-\lambda)\mathbf{B}) - \mathbf{C} = \mathbf{b} \otimes \hat{\mathbf{m}} \tag{B.7}$$

This indicates that the "averaged" deformation $(\lambda\mathbf{A}+(1-\lambda)\mathbf{B})$ can form an interface with C.

The sequence of deformations is an energy minimizing one if and only if $\mathbf{A}, \mathbf{B}, \mathbf{C}$ belong to the energy wells. For example, $\mathbf{C} = \mathbf{I}, \mathbf{B} = \mathbf{Q}_2\mathbf{U}_I, \mathbf{A} = \mathbf{Q}_1\mathbf{U}_J$ is one such

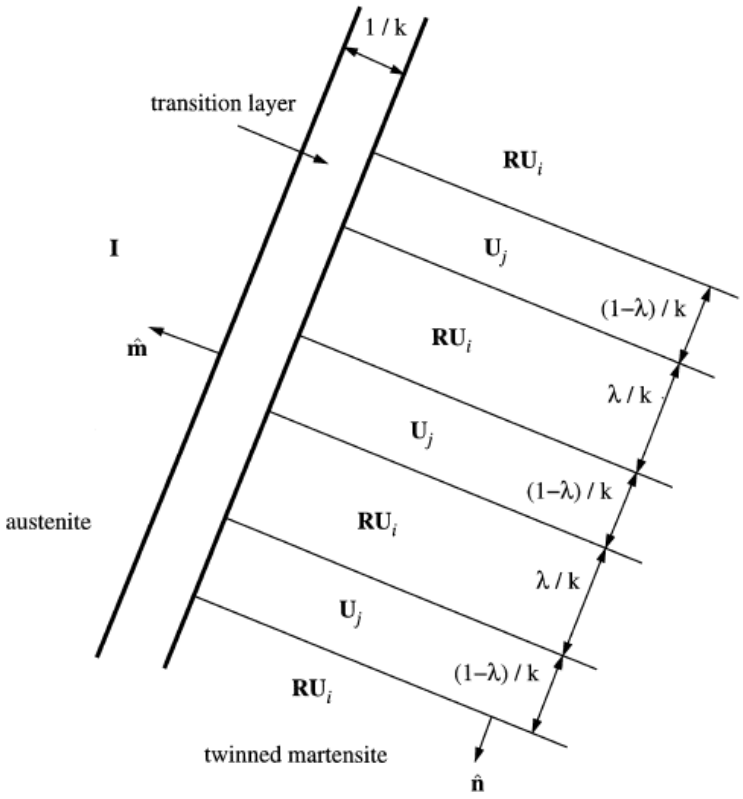

Figure B-1: Austenite-twinned martensite microstructure: $\mathbf{R}_{ij}\mathbf{U}_i$ and $\mathbf{U}_j$ represent variant pairs that satisfy the kinematics compatibility equation, produced in [13]

.

energy minimizing set, and the resulting habit plane equation is,

$$\mathbf{Q}\mathbf{U}_J - \mathbf{U}_I = \mathbf{a}' \otimes \hat{\mathbf{n}} \tag{B.8}$$

$$\mathbf{Q}'(\lambda \mathbf{Q}\mathbf{U}_J + (1-\lambda)\mathbf{U}_I) = \mathbf{I} + \mathbf{b} \otimes \hat{\mathbf{m}} \tag{B.9}$$

where $\mathbf{Q} = \mathbf{Q}_2^T \mathbf{Q}_1$ and $\mathbf{Q}' = \mathbf{Q}_2$. It can be concluded that a compatible interface between the austenite and fine twins of the Ith and Jth variants of martensite can be formed if and only if Equation B.9 is solvable. By solving the twinning equation, we can determine $\mathbf{Q}, \mathbf{a}, \hat{\mathbf{n}}$, and the habit plane can be solved following the procedure in [13, 122],

1. Calculate

$$\delta = \mathbf{a} \cdot \mathbf{U_I}(\mathbf{U_I^2} - \mathbf{I})^{-\mathbf{1}}\hat{\mathbf{n}}$$
$$\eta = \mathrm{tr}(\mathbf{U}_I^2) - \det(\mathbf{U}_I^2) - 2 + \frac{|a|^2}{2\delta}$$

The austenite-martensite interface equation has a solution if and only if $\delta \leq -2$ and $\eta \geq 0$

2. Calculate

$$\lambda = \frac{1}{2}(1 - \sqrt{1 + \frac{2}{\delta}})$$

3. Calculate

$$\mathbf{C} = (\mathbf{U}_I + \lambda\hat{\mathbf{n}} \otimes \mathbf{a})(\mathbf{U_I} + \lambda\mathbf{a} \otimes \hat{\mathbf{n}})$$

Find the eigenvalues and eigenvectors (automatically $\lambda_2 = 1$). The following is the solution to the habit plane equation:

$$\mathbf{b} = \rho\left(\sqrt{\frac{\lambda_3(1-\lambda_1)}{\lambda_3 - \lambda_1}}\hat{\mathbf{e}}_1 + \mathcal{K}\sqrt{\frac{\lambda_1(\lambda_3 - 1)}{\lambda_3 - \lambda_1}}\hat{\mathbf{e}}_3\right)$$
$$\hat{\mathbf{m}} = \frac{\sqrt{\lambda}_3 - \sqrt{\lambda}_1)}{\rho\sqrt{\lambda_3 - \lambda_1}}\left(-\sqrt{1-\lambda_1}\hat{\mathbf{e}}_1 + \mathcal{K}\sqrt{\lambda_3 - 1}\right)$$

where ρ is chose n to make $|\hat{\mathbf{m}}| = 1$ and $\mathcal{K} = \pm 1$. Then go back to the habit plane equation to obtain $\mathbf{Q}'$

4. If $\delta < -2$, replace λ with (1-λ) and repeat step 3.

In order to obtain all the possible habit plane solutions, the above procedure should be repeated for each set of twinning variants $\mathbf{U}_I, \mathbf{a}, \hat{\mathbf{n}}$.

Bibliography

[1] Ying Chen, Xuexi Zhang, David C Dunand, and Christopher A Schuh. Shape memory and superelasticity in polycrystalline cu–al–ni microwires. *Applied Physics Letters*, 95(17):171906, 2009.

[2] S. M. Ueland, Y. Chen, and C. A. Schuh. Oligocrystalline shape memory alloys. *Adv. Funct. Mater.*, 22(10):2094–2099, 2012.

[3] Patricio E Reyes-Morel and I-Wei Chen. Transformation plasticity of ceo2-stabilized tetragonal zirconia polycrystals: I, stress assistance and autocatalysis. *Journal of the American Ceramic Society*, 71(5):343–353, 1988.

[4] Richard HJ Hannink, Patrick M Kelly, and Barry C Muddle. Transformation toughening in zirconia-containing ceramics. *Journal of the American Ceramic Society*, 83(3):461–487, 2000.

[5] NK Simha. Twin and habit plane microstructures due to the tetragonal to monoclinic transformation of zirconia. *Journal of the Mechanics and Physics of Solids*, 45(2):261–292, 1997.

[6] Alan Lai. *Shape memory ceramics in small volumes*. PhD thesis, Massachusetts Institute of Technology, 2016.

[7] Patrick M Kelly and LR Francis Rose. The martensitic transformation in ceramics: its role in transformation toughening. *Progress in Materials Science*, 47(5):463–557, 2002.

[8] Makoto Hayakawa, N Kuntani, and M Oka. Structural study on the tetragonal to monoclinic transformation in arc-melted zro2-2mol.% y2o3—i. experimental observations. *Acta metallurgica*, 37(8):2223–2228, 1989.

[9] Makoto Hayakawa and M Oka. Structural study on the tetragonal to monoclinic transformation in arc-melted zro2-2mol.% y2o3—ii. quantitative analysis. *Acta metallurgica*, 37(8):2229–2235, 1989.

[10] M Hayakawa, K Adachi, and M Oka. Crystallographic analysis of the monoclinic herringbone structure in an arc-melted zro2-2 mol% y2o3 alloy. *Acta Metallurgica et Materialia*, 38(9):1753–1759, 1990.

[11] Alan Lai, Zehui Du, Chee Lip Gan, and Christopher A Schuh. Shape memory and superelastic ceramics at small scales. *Science*, 341(6153):1505–1508, 2013.

[12] G Rengarajan and JN Reddy. On the inelastic behavior of crystalline silicon at elevated temperatures. *Journal of the Mechanics and Physics of Solids*, 49(8):1665–1700, 2001.

[13] R.D. James and K.F. Hane. Martensitic transformations and shape memory alloys materials. *Acta Materialia*, 48:197–222, 2000.

[14] RN Patil and EC Subbarao. Axial thermal expansion of zro2 and hfo2 in the range room temperature to 1400° c. *Journal of Applied Crystallography*, 2(6):281–288, 1969.

[15] EC Subbarao, HS Maiti, and KK Srivastava. Martensitic transformation in zirconia. *Physica status solidi (a)*, 21(1):9–40, 1974.

[16] C Niclaeys, T Ben Zineb, S Arbab-Chirani, and E Patoor. Determination of the interaction energy in the martensitic state. *International Journal of plasticity*, 18(11):1619–1647, 2002.

[17] E Patoor, Mohammed El Amrani, André Eberhardt, and Marcel Berveiller. Determination of the origin for the dissymmetry observed between tensile and compression tests on shape memory alloys. *Le Journal de Physique IV*, 5(C2):C2–495, 1995.

[18] LC Chang and TA Read. Plastic deformation and diffusionless phase changes in metals–the gold-cadmium beta phase. *JOM*, 3(1):47–52, 1951.

[19] MV Swain. Shape memory behaviour in partially stabilized zirconia ceramics. *Nature*, 322(6076):234, 1986.

[20] Patrick T Mather, Xiaofan Luo, and Ingrid A Rousseau. Shape memory polymer research. *Annual Review of Materials Research*, 39:445–471, 2009.

[21] Kazuhiro Otsuka and Clarence Marvin Wayman. *Shape memory materials*. Cambridge university press, 1999.

[22] Andreas Lendlein and Steffen Kelch. Shape-memory polymers. *Angewandte Chemie International Edition*, 41(12):2034–2057, 2002.

[23] J Ortin and A Planes. Thermodynamic analysis of thermal measurements in thermoelastic martensitic transformations. *Acta metallurgica*, 36(8):1873–1889, 1988.

[24] Svetlana A Shabalovskaya. On the nature of the biocompatibility and on medical applications of niti shape memory and superelastic alloys. *Bio-medical materials and engineering*, 6(4):267–289, 1996.

[25] NB Morgan. Medical shape memory alloy applications–the market and its products. *Materials Science and Engineering: A*, 378(1):16–23, 2004.

[26] S Miyazaki. Medical and dental applications of shape memory. *Shape memory materials*, page 267, 1999.

[27] Diego Mantovani. Shape memory alloys: Properties and biomedical applications. *Jom*, 52(10):36–44, 2000.

[28] D Batalu, H Guoqiu, A Aloman, G Coşmeleaţă, L Xiaoshan, and Z Zhihua. A review on tini shape memory alloys (sma) used for medical applications. recycling aspects. *Research Gate*, 2020.

[29] Lorenza Petrini and Francesco Migliavacca. Biomedical applications of shape memory alloys. *Journal of Metallurgy*, 2011, 2011.

[30] Raana Sarvari, Peyman Keyhanvar, Samira Agbolaghi, Mohammad Sadegh Gholami Farashah, Amirhouman Sadrhaghighi, Mohammad Nouri, and Laila Roshangar. Shape-memory materials and their clinical applications. *International Journal of Polymeric Materials and Polymeric Biomaterials*, 71(5):315–335, 2022.

[31] Chunsheng Wen, Xiaojiao Yu, Wei Zeng, Shan Zhao, Lin Wang, Guangchao Wan, Shicheng Huang, Hannah Grover, and Zi Chen. Mechanical behaviors and biomedical applications of shape memory materials: A review. *AIMS Materials Science*, 5(4):559–590, 2018.

[32] Isabelle Denry and J Robert Kelly. State of the art of zirconia for dental applications. *Dental materials*, 24(3):299–307, 2008.

[33] Yen-Wei Chen, Joelle Moussi, Jeanie L Drury, and John C Wataha. Zirconia in biomedical applications. *Expert review of medical devices*, 13(10):945–963, 2016.

[34] Corina Marilena Cristache, Mihai Burlibasa, Gheorghe Cristache, Sergiu Drafta, Ion Alexandru Popovici, Alexandru Andrei Iliescu, Sonila Zisi, and Liliana Burlibasa. Zirconia and its biomedical applications. *Metalurgia International*, 16(7):18, 2011.

[35] Y Motemani, PJS Buenconsejo, and A Ludwig. Recent developments in high-temperature shape memory thin films. *Shape Memory and Superelasticity*, 1(4):450–459, 2015.

[36] Mohammad Mahdi Kheirikhah, Samaneh Rabiee, and Mohammad Ehsan Edalat. A review of shape memory alloy actuators in robotics. *Robot soccer world cup*, pages 206–217, 2010.

[37] L Janke, C Czaderski, M Motavalli, and J Ruth. Applications of shape memory alloys in civil engineering structures—overview, limits and new ideas. *Materials and Structures*, 38(5):578–592, 2005.

[38] HS Tzou, H-J Lee, and SM Arnold. Smart materials, precision sensors/actuators, smart structures, and structronic systems. *Mechanics of Advanced Materials and Structures*, 11(4-5):367–393, 2004.

[39] ZG Wei, R Sandstroröm, and S Miyazaki. Shape-memory materials and hybrid composites for smart systems: Part i shape-memory materials. *Journal of materials science*, 33(15):3743–3762, 1998.

[40] Satoru Aizawa, Tadahiro Kakizawa, and Masahiko Higasino. Case studies of smart materials for civil structures. *Smart materials and structures*, 7(5):617, 1998.

[41] Chung Yan Liu and Wei-Hsin Liao. A snake robot using shape memory alloys. In *2004 IEEE International Conference on Robotics and Biomimetics*, pages 601–605. IEEE, 2004.

[42] Young Pyo Lee, Byungkyu Kim, Moon Gu Lee, and Jong-Oh Park. Locomotive mechanism design and fabrication of biomimetic micro robot using shape memory alloy. In *IEEE International Conference on Robotics and Automation, 2004. Proceedings. ICRA'04. 2004*, volume 5, pages 5007–5012. IEEE, 2004.

[43] Arianna Menciassi, Samuele Gorini, G Pernorio, and Paolo Dario. A sma actuated artificial earthworm. In *IEEE International Conference on Robotics and Automation, 2004. Proceedings. ICRA'04. 2004*, volume 4, pages 3282–3287. IEEE, 2004.

[44] I Birkby and Ron Stevens. Applications of zirconia ceramics. In *Key Engineering Materials*, volume 122, pages 527–552. Trans Tech Publ, 1996.

[45] Jianliang Lin and Thomas C Stinnett. Development of thermal barrier coatings using reactive pulsed dc magnetron sputtering for thermal protection of titanium alloys. *Surface and Coatings Technology*, 403:126377, 2020.

[46] Xiao Wang and Alfred Ludwig. Recent developments in small-scale shape memory oxides. *Shape Memory and Superelasticity*, 6(3):287–300, 2020.

[47] Anne Leriche, Francis Cambier, and Helen Reveron. Zirconia ceramics, structure and properties. In Michael Pomeroy, editor, *Encyclopedia of Materials: Technical Ceramics and Glasses*, pages 93–104. Elsevier, Oxford, 2021.

[48] Cheng Fang, Wei Wang, Yuezhen Ji, and Michael CH Yam. Superior low-cycle fatigue performance of iron-based sma for seismic damping application. *Journal of Constructional Steel Research*, 184:106817, 2021.

[49] Vicen Torra, Antonio Isalgue, Ferran Martorelli, Francisco C Lovey, and Patrick Terriault. Damping in civil engineering using sma. part i: Particular properties of cuaibe for damping of family houses. *Canadian Metallurgical Quarterly*, 49(2):179–190, 2010.

[50] Iman Abavisani, Omid Rezaifar, and Ali Kheyroddin. Multifunctional properties of shape memory materials in civil engineering applications: A state-of-the-art review. *Journal of Building Engineering*, 44:102657, 2021.

[51] J San Juan, ML Nó, and CA Schuh. Superelastic cycling of cu–al–ni shape memory alloy micropillars. *Acta Materialia*, 60(10):4093–4106, 2012.

[52] Stian M Ueland and Christopher A Schuh. Grain boundary and triple junction constraints during martensitic transformation in shape memory alloys. *Journal of Applied Physics*, 114(5):053503, 2013.

[53] Ying Chen and Christopher A Schuh. Size effects in shape memory alloy microwires. *Acta Materialia*, 59(2):537–553, 2011.

[54] S. M. Ueland and C. A. Schuh. Superelasticity and fatigue in oligocrystalline shape memory alloy microwires. *Acta Mater*, 60(1):282–292, 2012.

[55] Stian M Ueland and Christopher A Schuh. Transition from many domain to single domain martensite morphology in small-scale shape memory alloys. *Acta materialia*, 61(15):5618–5625, 2013.

[56] H Das and F Spit. The measurement of the diffusion of phosphorus in oligocrystalline silicon with 32 p as radiotracer. a comparison of solid and liquid scintillation counting. *Journal of radioanalytical and nuclear chemistry*, 117(3):171–182, 1987.

[57] Z. Zhao, M. Ramesh, D. Raabe, A. Cuitiño, and R. Radovitzky. Investigation of three-dimensional aspects of grain-scale plastic surface deformation of an aluminum oligocrystal. *International Journal of Plasticity*, 24:2278:2297, 2008.

[58] Hidekazu Sakamoto, Yoshio Kijima, and Ken'ichi Shimizu. Fatigue and fracture characteristics of polycrystalline cu–al–ni shape memory alloys. *Transactions of the Japan Institute of Metals*, 23(10):585–594, 1982.

[59] K Otsuka. Cm wayman, k. nakai, h. sakamoto, and shimizu k. superelasticity effects and stress-induced martensitic transformations in cu-al-ni alloys. *Acta Metal-lurgica*, 24(3):207–26, 1976.

[60] S Miyazaki, Tadashi Kawai, and K Otsuka. Study of fracture in cu-al-ni shape memory bicrystals. *Le Journal de Physique Colloques*, 43(C4):C4–813, 1982.

[61] S Miyazaki, T Kawai, and K Otsuka. On the origin of intergranular fracture in β phase shape memory alloys. *Scripta Metallurgica*, 16(4):431–436, 1982.

[62] SW Husain and PC Clapp. The intergranular embrittlement of cu-ai-ni β-phase alloys. *Journal of materials science*, 22(7):2351–2356, 1987.

[63] A Creuziger and WC Crone. Grain boundary fracture in cualni shape memory alloys. *Materials Science and Engineering: A*, 498(1):404–411, 2008.

[64] Rebecca D Dar, Haoxue Yan, and Ying Chen. Grain boundary engineering of co–ni–al, cu–zn–al, and cu–al–ni shape memory alloys by intergranular precipitation of a ductile solid solution phase. *Scripta Materialia*, 115:113–117, 2016.

[65] Ilja Dvorak and EB Hawbolt. Transformational elasticity in a polycrystalline cu-zn-sn alloy. *Metallurgical Transactions A*, 6(1):95–99, 1975.

[66] GN Sure and LC Brown. The mechanical properties of grain refined β-cuaini strain-memory alloys. *Metallurgical and Materials Transactions A*, 15(8):1613–1621, 1984.

[67] M Somerday, JA Wert, and RJ Comstock. Effect of grain size on the observed pseudoelastic behavior of a cu-zn-al shape memory alloy. *Metallurgical and Materials Transactions A*, 28(11):2335–2341, 1997.

[68] A Ishida and M Sato. Thickness effect on shape memory behavior of ti-50.0 at.% ni thin film. *Acta Materialia*, 51(18):5571–5578, 2003.

[69] Dennis W Norwich and Audrey Fasching. A study of the effect of diameter on the fatigue properties of niti wire. *Journal of Materials Engineering and Performance*, 18(5):558–562, 2009.

[70] Y Sutou, T Omori, K Yamauchi, N Ono, R Kainuma, and K Ishida. Effect of grain size and texture on pseudoelasticity in cu–al–mn-based shape memory wire. *Acta Materialia*, 53(15):4121–4133, 2005.

[71] S Montecinos, A Cuniberti, and A Sepúlveda. Grain size and pseudoelastic behaviour of a cu–al–be alloy. *Materials Characterization*, 59(2):117–123, 2008.

[72] J. San Juan, M.L. Nó, and C.A. Schuh. Superelasticity and shape memory in micro- and nanometer-scale pillars. *Advanced Materials*, 20:272–278, 2008.

[73] J. San Juan, M.L. Nó, and C.A. Schuh. Nanoscale shape-memory alloys for ultrahigh mechanical damping. *Nature Nanotechnology*, 4:415–419, 2009.

[74] Nihan Tuncer, Lei Qiao, Raul Radovitzky, and Christopher A Schuh. Thermally induced martensitic transformations in cu-based shape memory alloy microwires. *Journal of materials science*, 50(22):7473–7487, 2015.

[75] Zehui Du, Xiao Mei Zeng, Qing Liu, Alan Lai, Shahrouz Amini, Ali Miserez, Christopher A Schuh, and Chee Lip Gan. Size effects and shape memory properties in zro2 ceramic micro-and nano-pillars. *Scripta Materialia*, 101:40–43, 2015.

[76] Xiao Mei Zeng, Alan Lai, Chee Lip Gan, and Christopher A Schuh. Crystal orientation dependence of the stress-induced martensitic transformation in zirconia-based shape memory ceramics. *Acta Materialia*, 116:124–135, 2016.

[77] Zehui Du, Xiao Mei Zeng, Qing Liu, Christopher A Schuh, and Chee Lip Gan. Superelasticity in micro-scale shape memory ceramic particles. *Acta Materialia*, 123:255–263, 2017.

[78] Xiaomei Zeng, Zehui Du, Christopher A Schuh, and Chee Lip Gan. Enhanced shape memory and superelasticity in small-volume ceramics: a perspective on the controlling factors. *MRS Communications*, 7(4):747–754, 2017.

[79] Xiao Mei Zeng, Zehui Du, Christopher A Schuh, Nobumichi Tamura, and Chee Lip Gan. Microstructure, crystallization and shape memory behavior of titania and yttria co-doped zirconia. *Journal of the European Ceramic Society*, 36(5):1277–1283, 2016.

[80] Xiao Mei Zeng, Zehui Du, Nobumichi Tamura, Qing Liu, Christopher A Schuh, and Chee Lip Gan. In-situ studies on martensitic transformation and high-temperature shape memory in small volume zirconia. *Acta Materialia*, 134:257–266, 2017.

[81] Girraj Kishore Bansal and AH Heuer. On a martensitic phase transformation in zirconia (zro2)-i. metallographic evidence. *Acta Metallurgica*, 20(11):1281–1289, 1972.

[82] GK Bansal and AH Heuer. On a martensitic phase transformation in zirconia (zro2)-ii. crystallographic aspects. *Acta Metallurgica*, 22(4):409–417, 1974.

[83] Ronald C Garvie and Michael V Swain. Thermodynamics of the tetragonal to monoclinic phase transformation in constrained zirconia microcrystals. *Journal of materials science*, 20(4):1193–1200, 1985.

[84] Sylvain Deville, Gérard Guénin, and Jérôme Chevalier. Martensitic transformation in zirconia: Part i. nanometer scale prediction and measurement of transformation induced relief. *Acta Materialia*, 52(19):5697 – 5707, 2004.

[85] Sylvain Deville, Gérard Guénin, and Jérôme Chevalier. Martensitic transformation in zirconia: part ii. martensite growth. *Acta materialia*, 52(19):5709–5721, 2004.

[86] Jerome Chevalier, Laurent Gremillard, Anil V Virkar, and David R Clarke. The tetragonal-monoclinic transformation in zirconia: lessons learned and future trends. *Journal of the American Ceramic Society*, 92(9):1901–1920, 2009.

[87] Jenq-Gong Duh, Hsing-Tao Dai, and Wei-Yuung Hsu. Synthesis and sintering behaviour in ceo2-zro2 ceramics. *Journal of materials Science*, 23(8):2786–2791, 1988.

[88] Patricio E Reyes-Morel, Jyh-Shiarn Cherng, and I-Wei Chen. Transformation plasticity of ceo2-stabilized tetragonal zirconia polycrystals: Ii, pseudoelasticity and shape memory effect. *Journal of the American Ceramic Society*, 71(8):648–657, 1988.

[89] RH Dauskardt, W Yu, and RO Ritchie. Fatigue crack propagation in transformation-toughened zirconia ceramic. *Journal of the American Ceramic Society*, 70(10):C–248, 1987.

[90] EP Butler. Transformation-toughened zirconia ceramics. *Materials Science and Technology*, 1(6):417–432, 1985.

[91] Michael V Swain and LRF Rose. Strength limitations of transformation-toughened zirconia alloys. *Journal of the American Ceramic Society*, 69(7):511–518, 1986.

[92] Arthur H Heuer. Transformation toughening in zro2-containing ceramics. *Journal of the American Ceramic Society*, 70(10):689–698, 1987.

[93] Edward L Pang, Caitlin A McCandler, and Christopher A Schuh. Reduced cracking in polycrystalline zro2-ceo2 shape-memory ceramics by meeting the cofactor conditions. *Acta Materialia*, 177:230–239, 2019.

[94] Edward L Pang, Gregory B Olson, and Christopher A Schuh. Role of grain constraint on the martensitic transformation in ceria-doped zirconia. *Journal of the American Ceramic Society*, 2020.

[95] Isabel R Crystal, Alan Lai, and Christopher A Schuh. Cyclic martensitic transformations and damage evolution in shape memory zirconia: Single crystals vs polycrystals. *Journal of the American Ceramic Society*, 103(8):4678–4690, 2020.

[96] Isabel R Crystal and Christopher A Schuh. Grain size-effect on intergranular cracking in shape memory zirconia during cyclic martensitic transformations. *Available at SSRN 3681175*, 2020.

[97] Tzer-Shin Sheu, Tseng-Ying Tien, and I-Wei Chen. Cubic-to-tetragonal (t') transformation in zirconia-containing systems. *Journal of the American Ceramic Society*, 75(5):1108–1116, 1992.

[98] Waltraud M Kriven, WL Fraser, and SW Kennedy. Martensite crystallography of tetragonal zirconia. In *Advances in ceramics*, pages 82–97. Am Ceram Soc, 1981.

[99] Cheikh Cisse, Wael Zaki, and Tarak Ben Zineb. A review of constitutive models and modeling techniques for shape memory alloys. *International Journal of Plasticity*, 76:244–284, 2016.

[100] Ralph C Smith. *Smart material systems: model development*. SIAM, 2005.

[101] Dimitris C. Lagoudas. *Shape memory alloys: modeling and engineering applications*. Springer, 2008.

[102] Ashish Khandelwal and Vidyashankar Buravalla. Models for shape memory alloy behavior: an overview of modeling approaches. *The International Journal of Structural Changes in Solids*, 1(1):111–148, 2009.

[103] Rohan Abeyaratne and James K Knowles. Nucleation, kinetics and admissibility criteria for propagating phase boundaries. *Shock induced transitions and phase structures in general media*, pages 1–33, 1993.

[104] R. Abeyaratne and J.K. Knowles. A continuum model of a thermoelastic solid capable of undergoing phase transitions. *Journal of the Mechanics and Physics of Solids*, 41:541–571, 1993.

[105] CA Rogers, CR Fuller, and C Liang. Active control of sound radiation from panels using embedded shape memory alloy fibers. *Journal of Sound Vibration*, 136(1):164–170, 1990.

[106] J.G. Boyd and D.C. Lagoudas. A thermodynamical constitutive model for shape memory materials. part i. the monolithic shape memory alloy. *International Journal of Plasticity*, 12:805–842, 1996.

[107] Ken Gall, T Jesse Lim, David L McDowell, Huseyin Sehitoglu, and Yuriy I Chumlyakov. The role of intergranular constraint on the stress-induced martensitic transformation in textured polycrystalline niti. *International Journal of Plasticity*, 16(10):1189–1214, 2000.

[108] MA Qidwai and DC Lagoudas. On thermomechanics and transformation surfaces of polycrystalline niti shape memory alloy material. *International journal of plasticity*, 16(10-11):1309–1343, 2000.

[109] P Thamburaja and L Anand. Polycrystalline shape-memory materials: effect of crystallographic texture. *Journal of the Mechanics and Physics of Solids*, 49(4):709–737, 2001.

[110] P Thamburaja and L Anand. Superelastic behavior in tension–torsion of an initially-textured ti–ni shape-memory alloy. *International Journal of Plasticity*, 18(11):1607–1617, 2002.

[111] L. Anand and M.E. Gurtin. Thermal effects in the superelasticity crystalline shape-memory materials. *Journal of the Mechanics and Physics of Solids*, 51:1015–1058, 2003.

[112] DJ Hartl and DC Lagoudas. Constitutive modeling and structural analysis considering simultaneous phase transformation and plastic yield in shape memory alloys. *Smart Materials and Structures*, 18(10):104017, 2009.

[113] Darren J Hartl, George Chatzigeorgiou, and Dimitris C Lagoudas. Three-dimensional modeling and numerical analysis of rate-dependent irrecoverable deformation in shape memory alloys. *International Journal of Plasticity*, 26(10):1485–1507, 2010.

[114] L. Qiao. *Computational modeling of size-dependent superelasticity in shape memory alloys*. PhD thesis, MIT, 2013.

[115] Satyabrata Dhala, Sushil Mishra, Asim Tewari, and Alankar Alankar. Modeling of finite deformation of pseudoelastic niti shape memory alloy considering various inelasticity mechanisms. *International Journal of Plasticity*, 115:216–237, 2019.

[116] Chao Yu, Guozheng Kang, and Qianhua Kan. A micromechanical constitutive model for grain size dependent thermo-mechanically coupled inelastic deformation of super-elastic niti shape memory alloy. *International Journal of Plasticity*, 105:99–127, 2018.

[117] JS Bowles and JK Mackenzie. The crystallography of martensite transformations i. *Acta metallurgica*, 2(1):129–137, 1954.

[118] JS Bowles and J K Mackenzie. The crystallography of martensite transformations iii. face-centred cubic to body-centred tetragonal transformations. *Acta Metallurgica*, 2(2):224–234, 1954.

[119] JK Mackenzie and JS Bowles. The crystallography of martensite transformations ii. *Acta Metallurgica*, 2(1):138–147, 1954.

[120] J.M. Ball and R.D. James. Fine phase mixtures as minimizers of energy. *Archive for Rational Mechanics Analysis*, 100(1):13–52, 1987.

[121] K.F. Hane and T.W. Shield. Microstructure in the cubic to monoclinic transition in titanium-nickel shape memory alloys. *Acta Materialia*, 47(9):2602–2617, 1999.

[122] Kaushik Bhattacharya. *Microstructure of martensite: why it forms and how it gives rise to the shape-memory effect*, volume 2. Oxford University Press, 2003.

[123] Surya R. Kalidindi. *Polycrystal plasticity : constitutive modeling and deformation processing*. PhD thesis, MIT, 1992.

[124] P Thamburaja. Constitutive equations for martensitic reorientation and detwinning in shape-memory alloys. *Journal of the Mechanics and Physics of Solids*, 53(4):825–856, 2005.

[125] P Thamburaja, H Pan, and FS Chau. Martensitic reorientation and shape-memory effect in initially textured polycrystalline ti–ni sheet. *Acta Materialia*, 53(14):3821–3831, 2005.

[126] N. Siredey, E. Patoor, M. Berveiller, and A. Eberhardt. Constitutive equations for polycrystalline thermoelastic shape memory alloys. part i. intragranular interactions and behavior of the grain. *International Journal of Solids and Structures*, 36:4289–4315, 1999.

[127] E Patoor, A Eberhardt, and M Berveiller. Micromechanical modelling of superelasticity in shape memory alloys. *Le Journal de Physique IV*, 6(C1):C1–277, 1996.

[128] Ken Gall and Huseyin Sehitoglu. The role of texture in tension–compression asymmetry in polycrystalline niti. *International Journal of Plasticity*, 15(1):69–92, 1999.

[129] H. Gao, Y. Huang, W.D. Nix, and J.W. Hutchinson. Mechanism-based strain gradient plasticity i. theory. *Journal of the Mechanics and Physics of Solids*, 47:1239–1263, 1999.

[130] Petr Šittner and Václav Novák. Anisotropy of martensitic transformations in modeling of shape memory alloy polycrystals. *International Journal of Plasticity*, 16(10):1243–1268, 2000.

[131] Xiujie Gao and L Catherine Brinson. A simplified multivariant sma model based on invariant plane nature of martensitic transformation. *Journal of Intelligent Material Systems and Structures*, 13(12):795–810, 2002.

[132] XM Wang, BX Xu, and ZF Yue. Micromechanical modelling of the effect of plastic deformation on the mechanical behaviour in pseudoelastic shape memory alloys. *International Journal of Plasticity*, 24(8):1307–1332, 2008.

[133] Amir Hosein Sakhaei and Kian-Meng Lim. Transformation-induced plasticity in high-temperature shape memory alloys: a one-dimensional continuum model. *Continuum Mechanics and Thermodynamics*, 28(4):1039–1047, 2016.

[134] Amir Hosein Sakhaei, Kian-Meng Lim, and Sergio Turteltaub. Thermomechanical discrete dislocation–transformation model of single-crystal shape memory alloy. *Mechanics of Materials*, 97:1–18, 2016.

[135] YM Jin and GJ Weng. Micromechanics study of thermomechanical characteristics of polycrystal shape-memory alloy films. *Thin Solid Films*, 376(1-2):198–207, 2000.

[136] Chao Yu, Guozheng Kang, and Qianhua Kan. Crystal plasticity based constitutive model of niti shape memory alloy considering different mechanisms of inelastic deformation. *International Journal of Plasticity*, 54:132–162, 2014.

[137] Y Gillet, E Patoor, and M Berveiller. Calculation of pseudoelastic elements using a non-symmetrical thermomechanical transformation criterion and associated rule. *Journal of intelligent material systems and structures*, 9(5):366–378, 1998.

[138] Christophe Bouvet, Sylvain Calloch, and Christian Lexcellent. A phenomenological model for pseudoelasticity of shape memory alloys under multiaxial proportional and nonproportional loadings. *European Journal of Mechanics-A/Solids*, 23(1):37–61, 2004.

[139] Dimitris Lagoudas, Darren Hartl, Yves Chemisky, Luciano Machado, and Peter Popov. Constitutive model for the numerical analysis of phase transformation in polycrystalline shape memory alloys. *International Journal of Plasticity*, 32:155–183, 2012.

[140] Yuan Zhong, Ken Gall, and Ting Zhu. Atomistic study of nanotwins in NiTi shape memory alloys. *Journal of Applied Physics*, 110:033532, 2011.

[141] Yuan Zhong, Ken Gall, and Ting Zhu. Atomistic characterization of pseudoelasticity and shape memory in NiTi nanopillars. *Acta Materialia*, 60(18):6301–6311, 2012.

[142] T Uehara, C Asai, and N Ohno. Molecular dynamics simulation of shape memory behaviour using a multi-grain model. *Modelling and Simulation in Materials Science and Engineering*, 17(3):035011, 2009.

[143] Chia-Wei Yang and Nien-Ti Tsou. Microstructural analysis and molecular dynamics modeling of shape memory alloys. *Computational Materials Science*, 131:293–300, 2017.

[144] Daniel Mutter and Peter Nielaba. Simulation of structural phase transitions in niti. *Physical Review B*, 82(22):224201, 2010.

[145] D. Mutter and P. Nielaba. Simulation of the thermally induced austenitic phase transition in niti nanoparticles. *The European Physical Journal B*, 84(1):109–113, 2011.

[146] Kai Nie, Ming-Peng Li, Wen-Ping Wu, and Qing-Ping Sun. Grain size-dependent energy partition in phase transition of niti shape memory alloys studied by molecular dynamics simulation. *International Journal of Solids and Structures*, 221:31–41, 2021.

[147] Andrei Artemev, Y Jin, and AG Khachaturyan. Three-dimensional phase field model of proper martensitic transformation. *Acta materialia*, 49(7):1165–1177, 2001.

[148] Mahmood Mamivand, Mohsen Asle Zaeem, and Haitham El Kadiri. A review on phase field modeling of martensitic phase transformation. *Computational Materials Science*, 77:304–311, 2013.

[149] Yuan Zhong and Ting Zhu. Phase-field modeling of martensitic microstructure in niti shape memory alloys. *Acta materialia*, 75:337–347, 2014.

[150] Cheikh Cissé and Mohsen Asle Zaeem. An asymmetric elasto-plastic phase-field model for shape memory effect, pseudoelasticity and thermomechanical training in polycrystalline shape memory alloys. *Acta Materialia*, 201:580–595, 2020.

[151] Bo Xu, Guozheng Kang, Chao Yu, and Qianhua Kan. Phase field simulation on the grain size dependent super-elasticity and shape memory effect of nanocrystalline niti shape memory alloys. *International Journal of Engineering Science*, 156:103373, 2020.

[152] Mohsen Asle Zaeem, Ning Zhang, and Mahmood Mamivand. A review of computational modeling techniques in study and design of shape memory ceramics. *Computational Materials Science*, 160:120–136, 2019.

[153] Ning Zhang and Mohsen Asle Zaeem. Competing mechanisms between dislocation and phase transformation in plastic deformation of single crystalline yttria-stabilized tetragonal zirconia nanopillars. *Acta Materialia*, 120:337–347, 2016.

[154] Ning Zhang and Mohsen Asle Zaeem. Role of grain boundaries in determining strength and plastic deformation of yttria-stabilized tetragonal zirconia bicrystals. *Journal of materials science*, 53(8):5706–5718, 2018.

[155] Ning Zhang and Mohsen Asle Zaeem. Understanding specimen-and grain-size effects on nanoscale plastic deformation mechanisms and mechanical properties of polycrystalline yttria-stabilized tetragonal zirconia nanopillars. *European Journal of Mechanics-A/Solids*, 76:80–90, 2019.

[156] Ning Zhang and Mohsen Asle Zaeem. Effects of grain orientations and pre-existing defects on mechanical properties and deformation mechanisms of polycrystalline yttria-stabilized tetragonal zirconia. *Materialia*, 9:100553, 2020.

[157] Ning Zhang and Mohsen Asle Zaeem. Effects of twin boundaries and pre-existing defects on mechanical properties and deformation mechanisms of yttria-stabilized tetragonal zirconia. *Journal of the European Ceramic Society*, 40(1):108–114, 2020.

[158] Mahmood Mamivand, Mohsen Asle Zaeem, Haitham El Kadiri, and Long-Qing Chen. Phase field modeling of the tetragonal-to-monoclinic phase transformation in zirconia. *Acta Materialia*, 61(14):5223–5235, 2013.

[159] Mahmood Mamivand, Mohsen Asle Zaeem, and Haitham El Kadiri. Shape memory effect and pseudoelasticity behavior in tetragonal zirconia polycrystals: A phase field study. *International Journal of Plasticity*, 60:71–86, 2014.

[160] Mahmood Mamivand, Mohsen Asle Zaeem, and Haitham El Kadiri. Effect of variant strain accommodation on the three-dimensional microstructure formation during martensitic transformation: application to zirconia. *Acta Materialia*, 87:45–55, 2015.

[161] Ehsan Moshkelgosha and Mahmood Mamivand. Anisotropic phase-field modeling of crack growth in shape memory ceramics: Application to zirconia. In *ASME International Mechanical Engineering Congress and Exposition*, volume 59490, page V012T10A064. American Society of Mechanical Engineers, 2019.

[162] Mark F Horstemeyer. *Integrated Computational Materials Engineering (ICME) for metals: using multiscale modeling to invigorate engineering design with science*. John Wiley & Sons, 2012.

[163] L. Noels and R. Radovitzky. A general discontinuous Galerkin method for finite hyperelasticity. Formulation and numerical applications. *International Journal for Numerical Methods in Engineering*, 68(1):64–97, 2006.

[164] L. Noels and R. Radovitzky. An explicit discontinuous Galerkin method for non-linear solid dynamics. Formulation, parallel implementation and scalability properties. *International Journal for Numerical Methods in Engineering*, 74(9):1393–1420, 2007.

[165] R. Radovitzky, A. Seagraves, M. Tupek, and L. Noels. A scalable 3D fracture and fragmentation algorithm based on a hybrid, discontinuous Galerkin, Cohesive Element Method. *Computer Methods in Applied Mechanics and Engineering*, 200:326–344, 2011.

[166] P Thamburaja and L Anand. Thermo-mechanically coupled superelastic response of initially-textured ti-ni sheet. *Acta Materialia*, 51(2):325–338, 2003.

[167] Jan De Vos, Etienne Aernoudt, and Luc Delaey. The crystallography of the martensitic transformation of bcc into 9r: A generalized mathematical model. *International Journal of Materials Research*, 69(7):438–444, 1978.

[168] H Horikawa, S Ichinose, K Morii, S Miyazaki, and K Otsuka. Orientation dependence of β 1 -> β 1 stress-induced martensitic transformation in a cu-ai-ni alloy. *Metallurgical and Materials Transactions A*, 19(4):915–923, 1988.

[169] S.N. Kuchnicki, A.M. Cuitiño, and R.A. Radovitzky. Efficient and robust constitutive integrators for single-crystal plasticity modeling. *International Journal of Plasticity*, 22:1988–2011, 2006.

[170] SN Kuchnicki, RA Radovitzky, and AM Cuitiño. An explicit formulation for multiscale modeling of bcc metals. *International Journal of Plasticity*, 24(12):2173–2191, 2008.

[171] G Rengarajan and KR Rajagopal. On the form for the plastic velocity gradient lp in crystal plasticity. *Mathematics and Mechanics of Solids*, 6(5):471–480, 2001.

[172] Barbe, F. and Decker, L. and Jeulin, D. and Cailletaud, G. Intergranular and intragranular behavior of polycrystalline aggregates. part 1: F.e. model. *International Journal of Plasticity*, 17:513–536, 2001.

[173] Raul Radovitzky and Alberto Cuitino. Direct numerical simulation of polycrystals. In *44th AIAA/ASME/ASCE/AHS/ASC Structures, Structural Dynamics, and Materials Conference*, page 1615, 2003.

[174] V Randle. The measurement of grain boundary geometry. institute of physics publishing, 1993.

[175] Valerie Randle. The coincidence site lattice and the 'sigma enigma'. *Materials Characterization*, 47(5):411–416, 2001.

[176] Erich H Kisi and Christopher J Howard. Elastic constants of tetragonal zirconia measured by a new powder diffraction technique. *Journal of the American Ceramic Society*, 81(6):1682–1684, 1998.

[177] T Waitz, D Spišák, J Hafner, and HP Karnthaler. Size-dependent martensitic transformation path causing atomic-scale twinning of nanocrystalline niti shape memory alloys. *EPL (Europhysics Letters)*, 71(1):98, 2005.

[178] Kenta Seki, Hiroaki Kura, Tetsuya Sato, and Tomoyasu Taniyama. Size dependence of martensite transformation temperature in ferromagnetic shape memory alloy fepd. *Journal of Applied Physics*, 103(6):063910, 2008.

[179] QingPing Sun, Ahadi Aslan, MingPeng Li, and MingXiang Chen. Effects of grain size on phase transition behavior of nanocrystalline shape memory alloys. *Science China Technological Sciences*, 57(4):671–679, 2014.

[180] Minglu Xia, Pan Liu, and Qingping Sun. Grain size dependence of young's modulus and hardness for nanocrystalline niti shape memory alloy. *Materials Letters*, 211:352–355, 2018.

[181] QP Sun and YJ He. A multiscale continuum model of the grain-size dependence of the stress hysteresis in shape memory alloy polycrystals. *International Journal of Solids and Structures*, 45(13):3868–3896, 2008.

[182] Stanislaw Stupkiewicz and Henryk Petryk. Grain-size effect in micromechanical modelling of hysteresis in shape memory alloys. *ZAMM-Journal of Applied Mathematics and Mechanics/Zeitschrift für Angewandte Mathematik und Mechanik*, 90(10-11):783–795, 2010.

[183] L. Qiao, J.J. Rimoli, Y. Chen, C. A. Schuh, and R. Radovitzky. Nonlocal superelastic model of size-dependent hardening and dissipation in single crystal Cu-Al-Ni shape memory alloys. *Phys. Rev. Lett.*, 106:085504, 2011.

[184] Lei Qiao and Raul Radovitzky. Computational modeling of size-dependent superelasticity of shape memory alloys. *Journal of the Mechanics and Physics of Solids*, 93:93–117, 2016.

[185] Majid Tabesh, James G Boyd, and Dimitris C Lagoudas. Modeling size effect in the sma response: a gradient theory. In *Behavior and Mechanics of Multifunctional Materials and Composites 2014*, volume 9058, pages 10–20. SPIE, 2014.

[186] Ahmad Fallah and Mohsen Botshekanan Dehkordi. A new nonlinear finite element model for transient dynamic response of a micro composite plate embedded with micro sma wires considering the size effects. *Mechanics of Advanced Materials and Structures*, pages 1–22, 2021.

[187] Arnaud Duval, Mohamed Haboussi, and T Ben Zineb. Modelling of localization and propagation of phase transformation in superelastic sma by a gradient nonlocal approach. *International Journal of Solids and Structures*, 48(13):1879–1893, 2011.

[188] Dongjie Jiang and Yao Xiao. Modelling on grain size dependent thermomechanical response of superelastic niti shape memory alloy. *International Journal of Solids and Structures*, 210:170–182, 2021.

[189] N.A. Fleck and J.W. Hutchinson. A phenomenological theory for strain gradient effects in plasticity. *Journal of the Mechanics and Physics of Solids*, 41:1825–1857, 1993.

[190] N.A. Fleck, G.M. Muller, M.F. Ashby, and J.W. Hutchinson. Strain gradient plasticity: Theory and Experiment. *Acta Materialia*, 42:475–487, 1994.

[191] N.A. Fleck and J.W. Hutchinson. A reformulation of strain gradient plasticity. *Journal of the Mechanics and Physics of Solids*, 49:2245–2271, 2001.

[192] Z Yu Hang, Mostafa Hassani-Gangaraj, Zehui Du, Chee Lip Gan, and Christopher A Schuh. Granular shape memory ceramic packings. *Acta Materialia*, 132:455–466, 2017.

[193] Saviz Mowlavi and Ken Kamrin. Contact model for elastically anisotropic bodies and efficient implementation into the discrete element method. *Granular Matter*, 23(2):1–29, 2021.

[194] A. Jérusalem, L. Stainier, and R. Radovitzky. A continuum model describing the reverse grain-size dependence of the strength of nanocrystalline metals. *Philosophical Magazine*, 87(17):2541–2559, 2007.

[195] A. Jerusalem, M. Dao, S. Suresh, and R. Radovitzky. Three-dimensional model of strength and ductility of polycrystalline copper containing nanoscale twins. *Acta Materialia*, 56:4647–4657, 2008.

[196] Kaushik Bhattacharya. Theory of martensitic microstructure and the shape-memory effect. *Available from author: bhatta@ co. caltech. edu*, 1998.

[197] Pingbing Ming et al. Cauchy–born rule and the stability of crystalline solids: static problems. *Archive for rational mechanics and analysis*, 183(2):241–297, 2007.